

**Springer Theses**

Recognizing Outstanding Ph.D. Research

Sen Zhang

# Electric-Field Control of Magnetization and Electronic Transport in Ferromagnetic/ Ferroelectric Heterostructures



Springer

# **Springer Theses**

Recognizing Outstanding Ph.D. Research

For further volumes:  
<http://www.springer.com/series/8790>

## **Aims and Scope**

The series “Springer Theses” brings together a selection of the very best Ph.D. theses from around the world and across the physical sciences. Nominated and endorsed by two recognized specialists, each published volume has been selected for its scientific excellence and the high impact of its contents for the pertinent field of research. For greater accessibility to non-specialists, the published versions include an extended introduction, as well as a foreword by the student’s supervisor explaining the special relevance of the work for the field. As a whole, the series will provide a valuable resource both for newcomers to the research fields described, and for other scientists seeking detailed background information on special questions. Finally, it provides an accredited documentation of the valuable contributions made by today’s younger generation of scientists.

### **Theses are accepted into the series by invited nomination only and must fulfill all of the following criteria**

- They must be written in good English.
- The topic should fall within the confines of Chemistry, Physics, Earth Sciences, Engineering and related interdisciplinary fields such as Materials, Nanoscience, Chemical Engineering, Complex Systems and Biophysics.
- The work reported in the thesis must represent a significant scientific advance.
- If the thesis includes previously published material, permission to reproduce this must be gained from the respective copyright holder.
- They must have been examined and passed during the 12 months prior to nomination.
- Each thesis should include a foreword by the supervisor outlining the significance of its content.
- The theses should have a clearly defined structure including an introduction accessible to scientists not expert in that particular field.

Sen Zhang

# Electric-Field Control of Magnetization and Electronic Transport in Ferromagnetic/ Ferroelectric Heterostructures

Doctoral Thesis accepted by  
Tsinghua University, Beijing, China

 Springer

*Author*

Dr. Sen Zhang  
College of Science  
National University of Defense Technology  
Changsha  
Hunan  
People's Republic of China

*Supervisor*

Prof. Yonggang Zhao  
Department of Physics and State Key  
Laboratory of Low-Dimensional  
Quantum Physics  
Tsinghua University  
Beijing  
People's Republic of China

ISSN 2190-5053

ISSN 2190-5061 (electronic)

ISBN 978-3-642-54838-3

ISBN 978-3-642-54839-0 (eBook)

DOI 10.1007/978-3-642-54839-0

Springer Heidelberg New York Dordrecht London

Library of Congress Control Number: 2014935972

© Springer-Verlag Berlin Heidelberg 2014

This work is subject to copyright. All rights are reserved by the Publisher, whether the whole or part of the material is concerned, specifically the rights of translation, reprinting, reuse of illustrations, recitation, broadcasting, reproduction on microfilms or in any other physical way, and transmission or information storage and retrieval, electronic adaptation, computer software, or by similar or dissimilar methodology now known or hereafter developed. Exempted from this legal reservation are brief excerpts in connection with reviews or scholarly analysis or material supplied specifically for the purpose of being entered and executed on a computer system, for exclusive use by the purchaser of the work. Duplication of this publication or parts thereof is permitted only under the provisions of the Copyright Law of the Publisher's location, in its current version, and permission for use must always be obtained from Springer. Permissions for use may be obtained through RightsLink at the Copyright Clearance Center. Violations are liable to prosecution under the respective Copyright Law. The use of general descriptive names, registered names, trademarks, service marks, etc. in this publication does not imply, even in the absence of a specific statement, that such names are exempt from the relevant protective laws and regulations and therefore free for general use.

While the advice and information in this book are believed to be true and accurate at the date of publication, neither the authors nor the editors nor the publisher can accept any legal responsibility for any errors or omissions that may be made. The publisher makes no warranty, express or implied, with respect to the material contained herein.

Printed on acid-free paper

Springer is part of Springer Science+Business Media ([www.springer.com](http://www.springer.com))

**Parts of this thesis have been published in the following journal articles:**

Zhang S., Zhao Y. G., Li P. S., Yang J. J., Rizwan S., Zhang J. X., Seidel J., Qu T. L., Yang Y. J., Luo Z. L., He Q., Zou T., Chen Q. P., Wang J. W., Yang L. F., Sun Y., Wu Y. Z., Xiao X., Jin X. F., Huang J., Gao C., Han X. F., Ramesh R. “Electric-Field Control of Nonvolatile Magnetization in  $\text{Co}_{40}\text{Fe}_{40}\text{B}_{20}/\text{Pb}(\text{Mg}_{1/3}\text{Nb}_{2/3})_{0.7}\text{Ti}_{0.3}\text{O}_3$  Structure at Room Temperature” *Physical Review Letters* 2012, 108, 137203 (Reproduced with Permission).

Zhang S., Zhao Y. G., Xiao X., Wu Y. Z., Rizwan S., Yang L. F., Li P. S., Wang J. W., Zhu M. H., Zhang H. Y., Jin X. F., Han X. F. “Giant electrical modulation of magnetization in  $\text{Co}_{40}\text{Fe}_{40}\text{B}_{20}/\text{Pb}(\text{Mg}_{1/3}\text{Nb}_{2/3})_{0.7}\text{Ti}_{0.3}\text{O}_3(011)$  heterostructure” *Scientific Reports* 2014, 4, 3727 (Reproduced with Permission).

# Supervisor's Foreword

Electric-field control of magnetism is important for new generation information storage technology with high integration density and low power consumption. In this regard, multiferroic materials have attracted much attention due to their interesting behavior—coexistence of ferroelectric and magnetic orders and coupling between them, which is essential for electric-field control of magnetism via the converse magnetoelectric effect. Unfortunately, room-temperature single-phase multiferroic materials are rare and the converse magnetoelectric effects are weak. So, as an alternative approach, artificial ferromagnetic–ferroelectric (FM–FE) multiferroic heterostructures have been widely studied recently and are believed to be promising for applications since various room-temperature FM and FE materials can be chosen. So far, electric-field control of magnetism has been realized in FM/FE heterostructures via strain coupling, charge modulation, and exchange bias, with a lot of work focusing on the strain-coupling systems. Previous reports on strain-coupling systems, based on the converse piezoelectric effect and converse magnetostriction, revealed a reversible butterfly-like behavior for the bipolar-electric-field-controlled magnetization and the change of magnetization that cannot retain (volatile) after removal of the applied electric fields, which is not useful for information storage. The aim of this book is to explore switchable, nonvolatile, and reversible electric-field controlled magnetism in FM/FE strain-coupling systems.

The book reports the first example of a large, switchable, and nonvolatile bipolar-electric-field-controlled magnetization at room-temperature in a compound multiferroic heterostructure consisting of amorphous  $\text{Co}_{40}\text{Fe}_{40}\text{B}_{20}$  (CoFeB) FM thin film and (001)-oriented  $\text{Pb}(\text{Mg}_{1/3}\text{Nb}_{2/3})_{0.7}\text{Ti}_{0.3}\text{O}_3$  (PMN-PT) FE substrate. Through investigations of the ferroelectric domains and crystal structures with in situ electric fields, a novel mechanism was demonstrated for electric-field control of magnetization involving the combined action of  $109^\circ$  ferroelastic domain switching in FE substrate and absence of magnetocrystalline anisotropy in amorphous CoFeB. The book also explores electric-field control of magnetism in a multiferroic heterostructure consisting of CoFeB thin film and (011)-oriented PMN-PT substrate, as well as electric-field-tunable magnetoresistance in a spin valve structure with involvement of CoFeB/PMN-PT heterostructure at room-temperature.

The book should be helpful for further exploring electric-field control of magnetism in FM/FE strain-coupling systems and prompting applications of the interesting effects.

Beijing, February 2014

Prof. Yonggang Zhao

# Acknowledgments

This book and the relevant work have been completed under the direction of Prof. Yonggang Zhao in Department of Physics, Tsinghua University and supported by the 973 project of the Ministry of Science and Technology of China, National Nature Science Foundation of China, Special Fund of Tsinghua for Basic Research, Tsinghua National Laboratory for Information Science and Technology Cross-discipline Foundation, Research Project of National University of Defense Technology.

I take this opportunity to express my gratitude to my supervisor Prof. Yonggang Zhao for all his efforts and instructions devoted to the project choice, experimental work, theoretical analysis, question discussion, and manuscript preparation related to my doctoral thesis. His help and instruction have benefited me all my life.

I owe a great deal to all the collaborators in the research related to my thesis; they are from Prof. Xiufeng Han and Yang Sun's group from Institute of Physics, Chinese Academy of Sciences, Prof. Ramamoorthy Ramesh's group in UC Berkeley of USA, Prof. Chen Gao's group in University of Science and Technology of China, Prof. Xiaofeng Jin and Yizheng Wu's group in Fudan University, Prof. Xiaozhong Zhang's group in Tsinghua University, and Mr. Zhenwen Huang in Bruker Company. The cooperation with them was a pleasant experience!

I owe many thanks to Prof. Ying-Hao Chu in National Chiao Tung University in Taiwan and Prof. Wenbin Wu in University of Science and Technology of China for their help and guidance. I also owe my thanks to Dr. Jing Wang and Dr. Jing Ma from Prof. Ce-Wen Nan's group in Tsinghua University for their kind help and discussion.

My thanks also go to teachers Meihong Zhu, Huiyun Zhang, and Xiaoping Zhang and students such as Peisen Li in Prof. Yonggang Zhao's group for their guidance, help, cooperation, and accompanying in my 5-year-long doctoral career in Tsinghua University.

I also extend sincere thanks to Profs. Hans Schmid, James Scott, Beatriz Noheda, Fert Albert, Kathrin Dörr, Manfred Fiebig, and Victor Mironov, for their kind help and permissions for reusing the published figures in my doctoral thesis.

Last but not the least, I thank my family and friends, especially my dear wife Wenjun Zhang, for their unfailing concern, encouragement, and support in my doctoral work and thesis writing.

Thanks, to all of you!

# Contents

<b>1</b>	<b>Introduction</b>	1
1.1	Information Storage Technology	2
1.1.1	Overview of Information Storage Technology	2
1.1.2	Magnetism and Magnetic Storage Technology	2
1.1.3	Ferroelectricity and Ferroelectric Storage Technology	7
1.1.4	Comparison and Summary of Information Storage Technologies	10
1.2	Multiferroic Materials and Magnetoelectric Effect	11
1.2.1	Definition and Properties of Multiferroic Materials	11
1.2.2	Historical Perspective of Multiferroics and ME Effect	13
1.2.3	Origin and Classification of Multiferroicity	14
1.3	Compounded Multiferroic Structures and Electric-Field Control of Magnetization	20
1.3.1	Classification of Compounded Multiferroic Structures	20
1.3.2	Compounded Multiferroic Heterostructures and Electric-Field Control of Magnetization	23
1.4	Application of Multiferroic Materials in Information Storage	30
1.4.1	Magnetoresistance and its Classification	31
1.4.2	Multiferroics and Magnetoelectric Multistate Memory	35
1.4.3	Multiferroic Structures and Electric-Writing and Magnetic-Reading Memory	38
1.5	General Topics and Brief Content of the Thesis	42
	References	43
<b>2</b>	<b>Experimental Methods</b>	49
2.1	Sample Preparation Techniques	49
2.1.1	Pulsed Laser Deposition Method	49
2.1.2	Magnetron Sputtering Method	52
2.2	Measurement, Characterization, and Analysis Techniques for Multiferroic Properties	55
2.2.1	Measurement and Characterization of Macroscopic Magnetic Properties	55
2.2.2	Characterization of Macroscopic Ferroelectric and Piezoelectric Properties	59

- 2.2.3 Characterization of Microscopic Ferromagnetic and Ferroelectric Properties . . . . . 62
- 2.2.4 X-ray Diffraction Techniques and Crystal Structure Analysis . . . . . 67
- 2.2.5 Electrical Transport Measurement Technique and Photolithography . . . . . 72
- References . . . . . 73
- 3 Electric-Field Control of Magnetism in CoFeB/PMN-PT(001) Structure . . . . . 75**
  - 3.1 Introduction . . . . . 75
  - 3.2 Sample Preparation and Characterization . . . . . 77
    - 3.2.1 Sample Preparation . . . . . 77
    - 3.2.2 Texture Characterization of the Sample . . . . . 78
    - 3.2.3 Characterization of Ferroelectric and Piezoelectric Properties . . . . . 79
  - 3.3 Electric-Field Control of Magnetism . . . . . 81
    - 3.3.1 Electric-Field Control of Magnetic Anisotropy . . . . . 81
    - 3.3.2 Electric-Field Control of Magnetization . . . . . 83
    - 3.3.3 Electric-Field Control of Magnetic Domain . . . . . 86
  - 3.4 Mechanism Investigation . . . . . 88
    - 3.4.1 Eliminating Interfacial Charge Modulation and Current Effect . . . . . 88
    - 3.4.2 Characterization and Analysis of Ferroelectric Domain of PMN-PT . . . . . 89
    - 3.4.3 Magnetic Response of CoFeB to 109° Ferroelectric Domain Switching . . . . . 94
    - 3.4.4 Quantitative Analysis Based on XRD-RSM . . . . . 95
    - 3.4.5 Further Inference and Validation Based on the Mechanism . . . . . 100
  - 3.5 Characterization of Properties Related to Application Requirements . . . . . 103
    - 3.5.1 Characterization of Fatigue and Retention Properties of the Sample . . . . . 103
    - 3.5.2 Magnetic Field-Assisted Electric-Field Control of Magnetization Reversal . . . . . 104
  - 3.6 Chapter Summary . . . . . 106
  - References . . . . . 106
- 4 Electric-Field Control of Magnetism and Magnetoresistance in CoFeB/PMN-PT(011) Structure . . . . . 109**
  - 4.1 Introduction . . . . . 109
  - 4.2 Sample Preparation and Characterization . . . . . 111
    - 4.2.1 Sample Preparation . . . . . 111

- 4.2.2 Characterization of Crystal Structure, Ferroelectricity,  
and Piezoelectricity . . . . . 112
- 4.3 Electric-Field Control of Magnetism . . . . . 114
  - 4.3.1 Electric-Field Control of Magnetization . . . . . 114
  - 4.3.2 Mechanism and Quantitative Investigation . . . . . 118
  - 4.3.3 Characterization and Design for Application . . . . . 121
- 4.4 Electric-Field Control of Magnetoresistance . . . . . 123
  - 4.4.1 Electric-Field Control of Magnetization in CoFeB  
Film with Pinning Layer . . . . . 123
  - 4.4.2 Preparation of Spin Valve and Electric-Field  
Control of Magnetoresistance . . . . . 124
- 4.5 Chapter Summary . . . . . 127
- References . . . . . 127
  
- 5 Summary and Outlook . . . . . 129**
  - 5.1 Research Summary . . . . . 129
  - 5.2 Outlook and Prospect . . . . . 130

# Abbreviations

AFM	Atomic Force Microscopy
AMR	Anisotropic Magneto-resistance
BFO	$\text{BiFeO}_3$
CMR	Colossal Magneto-resistance
CoFeB	$\text{Co}_{40}\text{Fe}_{40}\text{B}_{20}$
DMS	Diluted Magnetic Semiconductor
DRAM	Dynamic Random Access Memory
DRO	Destructive Readout
ESR	Electron Spin Resonance
FeRAM	Ferroelectric Random Access Memory
FET	Field Effect Transistor
FMR	Ferromagnetic Resonance
GMR	Giant Magneto-resistance
LSMO	$\text{La}_{0.67}\text{Sr}_{0.33}\text{MnO}_3$
ME	Magnetoelectric
MERAM	Magnetoelectric Random Access Memory
MFM	Magnetic Force Microscopy
MOKE	Magneto-Optical Kerr Effect
MR	Magneto-resistance
MRAM	Magnetic Random Access Memory
MTJ	Magnetic Tunneling Junction
NDRO	Non-destructive Readout
OMR	Ordinary Magneto-resistance
PFM	Piezoresponse Force Microscopy
PLD	Pulsed Laser Deposition
PMN-PT	$\text{Pb}(\text{Mg}_{1/3}\text{Nb}_{2/3})_{0.7}\text{Ti}_{0.3}\text{O}_3$
PZN-PT	$\text{Pb}(\text{Zn}_{1/3}\text{Nb}_{2/3})_{0.7}\text{Ti}_{0.3}\text{O}_3$
RAM	Random Access Memory
ROM	Read Only Memory
SPM	Scanning Probe Microscopy
SQUID	Superconducting QUantum Interference Device

SRAM	Static Random Access Memory
STM	Scanning Tunneling Microscopy
STT	Spin Transfer Torque
SV	Spin Valve
TMR	Tunneling Magneto-resistance
XRD	X-ray Diffraction

# Chapter 1

## Introduction

The twenty-first century is an era of information technology, in which the ever-increasing volume of information has put forward more and more challenging demands for the information storage technology. At present, exploiting new concepts for dense, fast, and nonvolatile random access memory with reduced energy consumption is a significant issue in the scientific research and information technology. Magnetic recording, one of the conventional information recording methods, has been widely used in data storage industries, in which the discovery of the giant/tunneling magneto-resistance has significantly promoted magnetic memory technology due to the advantages of high sensitivity and non-destructive readout (NDRO). However, the information writing method by magnetic field or electric current has the handicaps of difficulty in high density integration and relatively high writing energy. In contrast, the ferroelectric recording has the advantage of high density storage capability and relatively low energy consumption by electric field writing, but the complex reading process and destructive readout (DRO) have greatly hindered its application as memories. Is it possible to combine the advantages of the two recording methods and overcome their disadvantages? The discovery of multiferroic materials and the magnetoelectric (ME) coupling effect has brought a promising solution to the issue. What is more multiferroic materials bringing about novel physical phenomena and potential applications in multifunctional devices have drawn much interest in the scientific research and been extensively studied. This chapter begins with some basic technologies in information storage, reviews the research progresses related to multiferroic materials and ME coupling, and finally addresses the brief thought of the thesis.

## 1.1 Information Storage Technology

### 1.1.1 Overview of Information Storage Technology

Since the origin of human civilization, people have to face the issue of information storage all the time. From recording information by knotting the rope to writing texts on the paper, information has recorded the human history and civilization. In another aspect, human civilization (especially science, e.g., the invention of paper) has also promoted the information storage technology. Nowadays, the scopes of information storage technologies are already far beyond the text recording on the papers. The modern storage technologies include magnetic recording, electrical recording, optical recording, and numerous new types of recording methods [1].

The main recording devices and memories at present can be classified as following by the different storage techniques as discussed above. (i) Information recording related to magnetic technology, such as tape, floppy disk, hard disk, magnetic cards, and so on; (ii) Information recording related to electrical technology, such as random access memory (RAM, including static RAM, i.e., SRAM and dynamic RAM, i.e., DRAM), read only memory (ROM), flash memory (FLASH), and so on; (iii) Information recording related to optical technology, such as CD-ROM/RAM, DVD-ROM/RAM, magneto-optical disk, and so on. Different recording methods adapt to different applications and demands in information storage due to their characteristics and performances [2], as shown in Table 1.1. Among the information recording technologies, magnetic recording is dominated and has played an important role in the information storage, due to its comprehensive performances, such as relatively large capacity, high reading speed, NDRO, and so on. Besides, new types of high-performance memories, such as magnetic random access memory (MRAM) and ferroelectric memory (FeRAM) are under extensive research and design for applications.

### 1.1.2 Magnetism and Magnetic Storage Technology

In general, the magnetism of materials originated from the spin of electrons and their orbital motion, and the properties of magnetism are determined by the electronic arrangement within atoms and the crystal structure of the material. Due to the arrangement of electrons and exchange interaction between them, different magnetic orders are presented, which exhibit different magnetic properties [3, 4]. As a result, the magnetism of materials can be divided into paramagnetism, diamagnetism, ferromagnetism, ferrimagnetism, antiferromagnetism, helimagnetism, and so on, as shown in Fig. 1.1.

*Ferromagnetism* is a kind of phenomenon that the magnetic moments of atoms have been aligned in the same direction to achieve a kind of ordering (spontaneous magnetization) without external magnetic field. This kind of magnetic order is

**Table 1.1** Performances comparison of different recording technologies (© [2002] IEEE. Reprinted, with permission, from Ref. [2])

Memories	DRAM	SRAM	Flash	PRAM	FeRAM	MRAM
Nonvolatile	No	No	Yes	Yes	Yes	Yes
Program power	Low	Low	High	Low	Low	High
Program voltage	Low	Low	High	–	Low	Middle
Reading voltage	100–200 mV	100–200 mV	Delta Current	–	–	20–40 %
Writing time	50 ns	8 ns	1 μs	10 ns	30 ns	30 ns
Erasure time	50 ns	8 ns	1–100 ms	50 ns	30 ns	30 ns
Reading time	50 ns	8 ns	50 ns	20 ns	30 ns	30 ns
Program energy	Middle	High	High	Low	Low	Middle

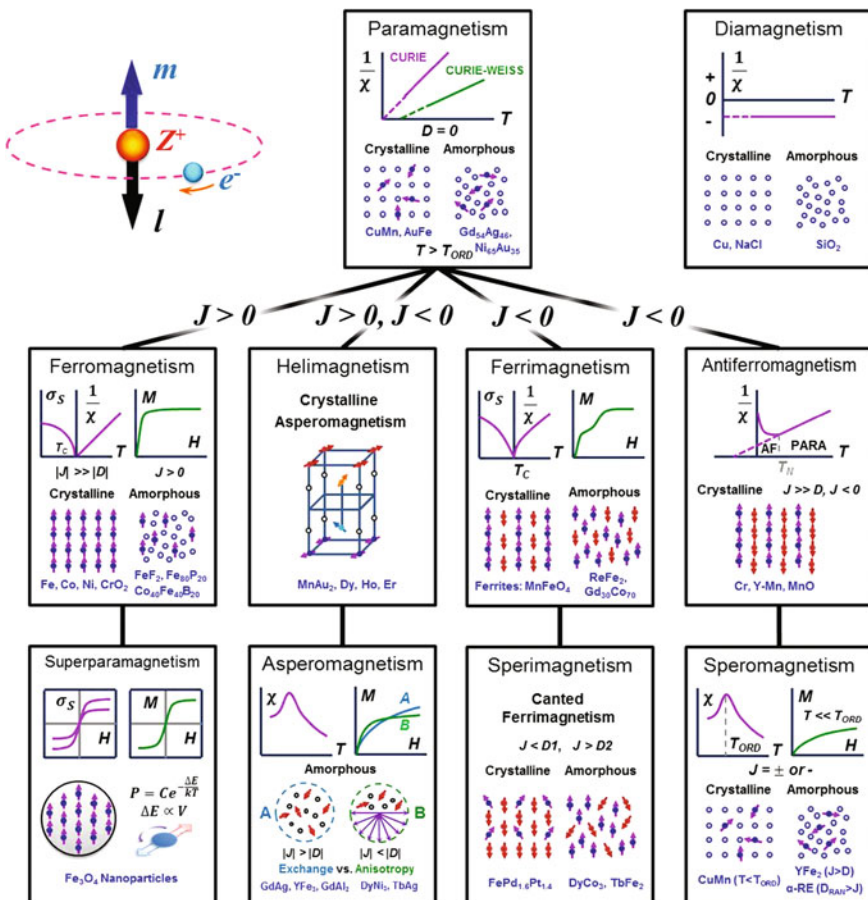
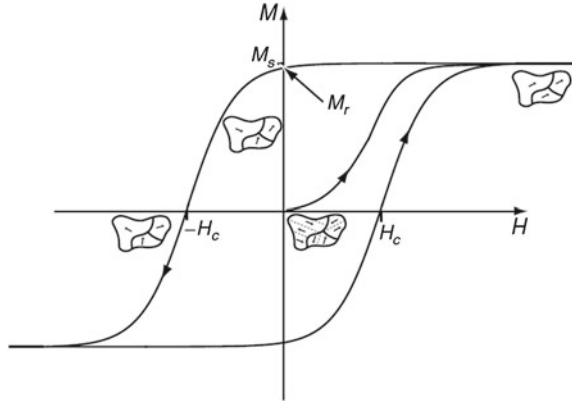


**Fig. 1.1** Origin of magnetism in materials and their classification (Reprinted from Ref. [4] and C.M. Hurd, Contemp. Phys. 23, L69 (1982) by permission of Taylor & Francis Ltd.)

**Fig. 1.2** Magnetic domains and magnetic hysteresis loop in ferromagnetic materials (Reprinted from Ref. [4] by permission of Taylor & Francis Ltd.)

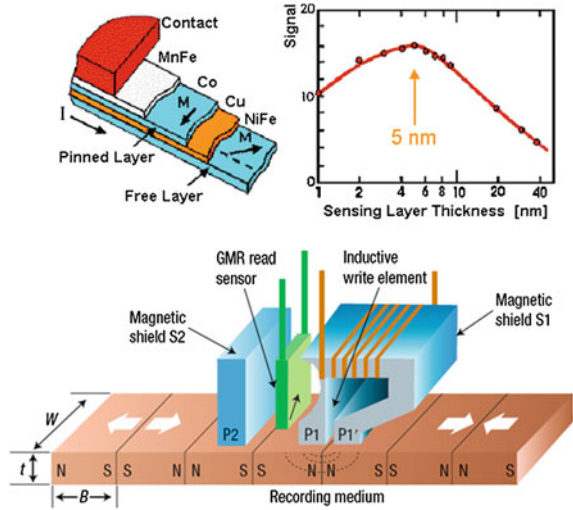


formed due to the exchange interaction between electrons in different atoms under certain temperature (Curie temperature). The spontaneous magnetization in ferromagnetic materials is divided into a number of small regions, and the atomic magnetic moments are arranged parallel in the same direction inside each region, which is called magnetic domain. The orientations of the spontaneous magnetization of different magnetic domains in the material are random and different from each other, and the whole sample show zero net magnetization without magnetic field due to the canceling effect between different magnetic domains. When applied with an external magnetic field, the magnetization of each magnetic domain tends to align along the direction of the external magnetic field, and the net magnetization can achieve a high value. After the magnetic field is removed, the states of magnetization and magnetic domains are maintained, resulting in a hysteresis behavior in the magnetization–magnetic field ( $M$ – $H$ ) curve, which is known as the magnetic hysteresis loop, as shown in Fig. 1.2.

*Antiferromagnetism* is a kind of phenomenon that the magnetic moments of atoms align in a regular pattern with neighboring spins aligning in opposite directions. As a result, antiferromagnetic materials do not exhibit any macro magnetic properties due to the neighbor atomic magnetic moments canceling with each other, and their magnetization curves are similar to those of paramagnetism with linear behaviors. The equivalent internal magnetic field in antiferromagnetic materials is generally much larger than the external magnetic field, and an external magnetic field is hard to change the orientation of the magnetic moment of antiferromagnetism. Thus, antiferromagnetic materials are often used as magnetic pinned layers in the exchange bias system.

*Helimagnetism* is a kind of phenomenon that the magnetic moments of atoms are arranged in a helical structure with neighboring spins shifting a certain angle to each other. As a result, the magnetic moments are canceled with each other in some of the arrangements, and the materials do not exhibit any macro magnetic properties; while in other arrangements the magnetic moments cannot be completely canceled with each other, and obvious macro magnetic properties are

**Fig. 1.3** Spin valve and magnetic recording devices  
 (© [1994] IEEE. Reprinted, with permission, from Ref. [7] and Macmillan Publishers Ltd.: Ref. [9], © 2007)

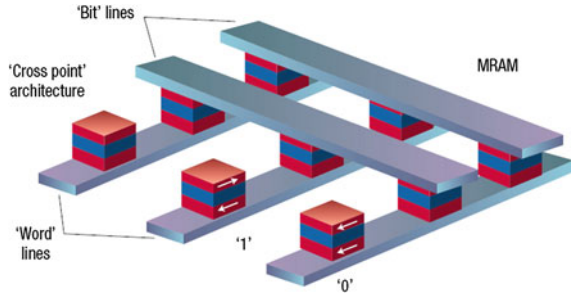


presented. Helimagnetism always appears in materials containing rare earth elements with  $4f$  electrons.

Due to the ability that the spontaneous magnetization of the ferromagnetic materials can be switched by an external magnetic field, and it can be maintained after removing the magnetic field, ferromagnetic materials can be used as the logic unit in memories with magnetization up representing “1” and magnetization down representing “0”. As a result, ferromagnetism has an extremely important position and wide application in modern science and technology [5–7]. What is more, the discovery of the giant magnetoresistance (GMR) effect and its application in the spin valves (SVs, as shown in Fig. 1.3) as the magnetic reading head, has largely improved the sensitivity of magnetic detection and the density of magnetic recording in the information storage and brings the revival of spintronic devices.

Although magnetic recording technology has many advantages and is dominated in the information storage devices, it is facing more challenges with the continuously increased requirements of the recording density of information in recent years [8]. First, the higher density of the information recording requires the smaller of the magnetic unit cell. According to the theory of magnetism, the smaller the magnetic unit cell is, the harder it is to maintain the state of the magnetization, resulting in the instability of the recorded information. When the size of the magnetic recording medium approaches to a certain small limit, the thermal disturbance at room temperature will cause the self-demagnetization effect (i.e., the superparamagnetic limit of magnetization) and result in failure of the recorded information. Therefore, there is a density limit for magnetic recording. Second, in order to improve the stability of the information recorded or extend the superparamagnetic limit of magnetic recording medium, the most commonly used method is to increase the coercive field of the magnetic recording layer. The higher the coercive field of the magnetic materials is, the harder the

**Fig. 1.4** Configuration of the MRAM (Reprinted by permission from Macmillan Publishers Ltd.: Ref. [9], © 2007)



magnetization is to be disturbed by the demagnetization effect, and the more stable the recording bit of information will be. However, in another aspect, the higher the coercive field is, the larger the external magnetic field is required to change the magnetization in the recording process, which demands a higher writing energy.

Since the tunneling magnetoresistance (TMR) effect has a higher magnetoresistance ratio ( $\Delta R/R$ ) and larger background resistance than the GMR effect, the MRAM is possible to be achieved based on the magnetic tunneling junctions (MTJs). Compared with the ordinary magnetic recording device, MRAM can be employed as a random access memory with higher storage density; and compared with the DRAM, MRAM has a nonvolatile property which does not need additional energy to refresh the memory units to keep the information after recording. As a result, MRAM is considered as a kind of very important memory with broad prospects in applications and has been extensively investigated and developed [9–11].

The reading out process of MRAM can be easily realized by measuring the TMR of the MTJ units, and the writing process is realized by crossover controlling of the electrical currents in the regularly arranged metal wires, which are perpendicular to each other and clip the MTJ unit in the top and bottom directions. The top wire is called “Bit” line and the bottom wire is called “Word” line, as shown in Fig. 1.4. When the bit line is loaded with a current, a magnetic field is generated around it and all of the memory cells in this bit line are loaded with an external magnetic field. However, the current is exactly controlled to make sure the magnetic field is not large enough to switching the magnetization of the free layer in each MTJ unit. Afterwards, another current is applied in the word line, which also generates a magnetic field around it and loads all of the memory cells in this word line with the induced magnetic field. At this time, the memory cell located in the cross-point of the bit line and word line has been loaded with a superimposing magnetic field with large value, and the magnetization of the free layer in this MTJ unit can be completely switched. Thus, the directions of magnetization of the two ferromagnetic layers in each MTJ unit can be switched parallel (low resistance, denoted as “0”) or antiparallel (high resistance, denoted as “1”) and the information writing operation can be achieved.

Seeing from the writing process of the MRAM, one may find the disadvantages of difficulty in accurately controlling the current, high power consumption, and possible mistakes in this cross-point writing [11], which may hinder its applications.

For example, the selected memory cell to be written is loaded by a strong superimposing magnetic field induced by two perpendicular currents flowing along the word line and bit line, but all the other memory cells in the word line and bit line are also exposed to a magnetic field with a half writing power. Although these half-chosen memory cells may not be written for the magnetic field is not strong enough to change the direction of the magnetization in the MTJ unit, but the disturbances of the half-power will inevitably affect the stability of recorded information. What is more, the situation will be worse with the increment of integrating density, and the possibility of miswriting will also be largely increased. Although a variety of other methods have been proposed to improve the writing process in MRAM, such as “spin transfer torque (STT),” “writing current with a vertical direction,” and so on [10], the writing process of MRAM and its high power consumption are still difficult problems to be solved [11].

### ***1.1.3 Ferroelectricity and Ferroelectric Storage Technology***

Ferroelectricity is a kind of phenomenon that some materials have a spontaneous electric polarization and the spontaneous polarization can be reversed by an external electric field. Materials with ferroelectricity are called ferroelectrics, such as  $\text{BaTiO}_3$  and  $\text{LiNbO}_3$ . The properties of ferroelectricity and ferromagnetism have many similar behaviors corresponding to each other, and the prefix ferro is used to describe the common properties of them instead of meaning ferroelectric materials contain any iron. Ferroelectricity was discovered by a French scientist named Valasek in Rochelle salt ( $\text{NaKC}_4\text{H}_4\text{O}_6 \cdot 4\text{H}_2\text{O}$ ) in 1920; as a result, it was also named as Valasek electricity or Rochelle electricity [12].

Seen from the microscopic scale, the ferroelectricity originates from the distortion of the lattice. Below a certain temperature, a structural distortion happens to the crystal lattice of the materials in which the center of negative charge does not coincide with the center of positive charge, and the electric dipole moment is induced. Due to the emergence of the electric dipole moments and the interaction between each other, the electric dipole moments are aligned orderly in some special directions, resulting in the spontaneous polarization of ferroelectricity. When loaded by an external electric field, the polarization state of the ferroelectric materials will change with the electric field, resulting in a ferroelectric hysteresis loop involving the spontaneous polarization ( $P$ ) and the external electric field ( $E$ ), as shown in Fig. 1.5. From the ferroelectric hysteresis loops (i.e.,  $P$ - $E$  loops), one can see the saturated polarization, remanent polarization, coercive field, and electric susceptibility of the ferroelectric materials, which are the main parameters to characterize the property of ferroelectricity.

When the spontaneous polarization emerges in ferroelectric materials, the depolarization field and strain will be induced, which increases the total energy of the system. In order to reduce the energy, the spontaneous polarization of the sample will be divided into a number of small areas, which are called ferroelectric domains.

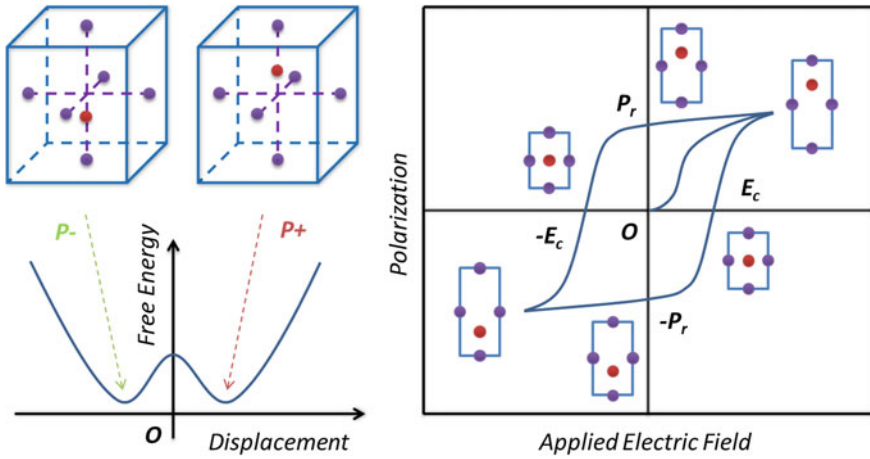
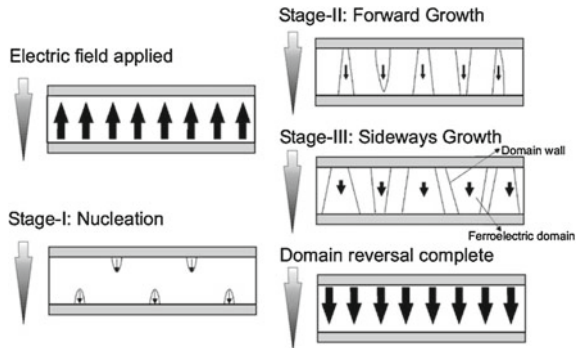


**Fig. 1.5** The origin of ferroelectricity (*left*) and the ferroelectric hysteresis loop (*right*)

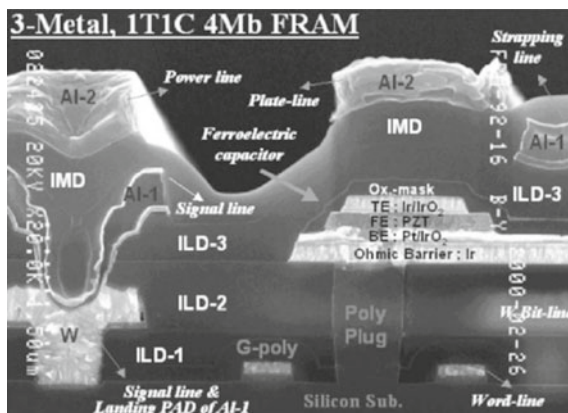
**Fig. 1.6** Ferroelectric domain and ferroelectric polarization reversal process (Reprinted with permission from Ref. [13]. © 2005 by American Physical Society)



In each ferroelectric domain, the internal electric dipoles are arranged in the same direction, resulting in the direction of net polarization pointing along a certain direction. However, the directions of polarization in different ferroelectric domains are different, and the net polarization of the whole sample is neutralized, reducing the electrostatic energy and elastic energy. The process of ferroelectric polarization switched by an external electric field is accompanied with the process of ferroelectric domain nucleation or reorientation (Fig. 1.6), which reveals the inherent association between the ferroelectric domains and ferroelectric hysteresis loops [13].

Similar to the classification of magnetic materials, the dielectric properties of materials can also be divided into paraelectricity, ferroelectricity, and antiferroelectricity. Similar to the ferromagnetism, the ferroelectric order of materials only exists below a certain temperature, namely the Curie Temperature ( $T_C$ ). When the temperature is higher than  $T_C$ , the material changes from the ferroelectric phase to the paraelectric phase, and the spontaneous polarization of ferroelectricity disappears. Since the ferroelectricity is a subfamily of the dielectricity, piezoelectricity,

**Fig. 1.7** The structure of FeRAM observed by scanning electron microscope (SEM) (Reprinted with permission from Ref. [13]. © 2005 by American Physical Society)



and pyroelectricity, the ferroelectric materials will inevitably exhibit the dielectric, piezoelectric, and pyroelectric properties. What is more, the ferroelectric materials also have interactions with light and exhibit some optical properties. As a result, the ferroelectricity has drawn much attention not only in scientific research but also in applications. For example, one important application of ferroelectricity is in the information storage technology. Utilizing the properties that the polarization of ferroelectric materials can be reversed by an external electric field and the states of polarization are maintained after removing the electric field, ferroelectric materials can be used as the recording media with the remanent polarizations ( $\pm P_r$ ) corresponding to the binary elements “1” and “0”, respectively. As a result, the concept and model of ferroelectric random access memory (FeRAM) have been proposed and designed as shown in Fig. 1.7, which is a kind of nonvolatile random access memory with low power consumption, has been investigated intensively and widely [14–17].

Different from the semiconductor-based DRAM in which the information is recorded by the charges on the capacitor, the information saved in the FeRAM is recorded by the position of the center atom in the ferroelectric crystal unit cell. In fact, directly detecting the position of the center atom by electrical method is impossible, the actual readout operation is realized by a complicated indirect process as follows. First, a given electric pulse named “reading voltage” is applied on the capacitor of the FeRAM cell, i.e., the capacitor is charging. Second, the leakage current namely “reading current” is detected by an ampere meter at the same time. If the center atom of the ferroelectric unit cell is already located in the position where the reading voltage is trying to drive, the center atom does not move and results in zero reading current. Otherwise, the center atom will be driven from the initial position to the other location, and a current peak is induced in the reading current due to polarization switching. Therefore, the information “1” or “0” recorded by the atomic position “up” or “down” in the memory cell can be readout and further processed by the electronic circuit, as shown in Fig. 1.8.

Seeing from the reading process of FeRAM as discussed above, the reading operation may cause a state change in the storage unit, which is essentially a

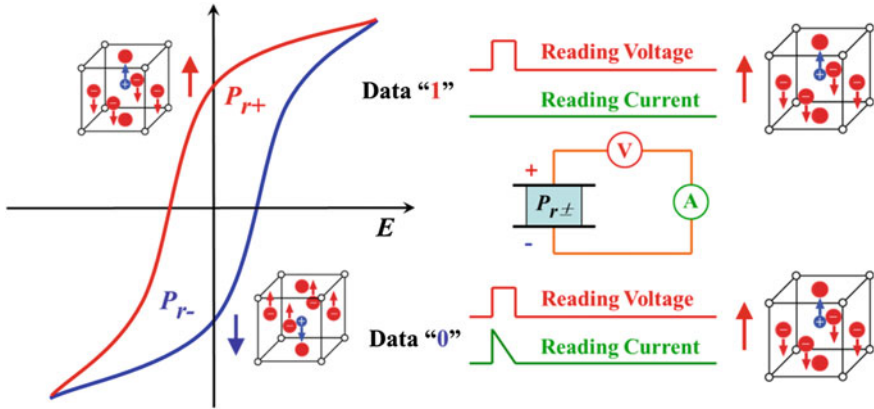


**Fig. 1.8** The readout process of FeRAM

destructive readout (DRO). In order to preserve the original information, each reading operation is followed by a reduction process to restore the data bits automatically. As we know, the fatigue effect is widely observed in ferroelectric materials, i.e., the value of remanent polarization ( $P_r$ ) will be gradually reduced after repeated inversion of the polarization, resulting in loss of the capability in the data recording. Since the readout process of the FeRAM is destructive, in which the “reading” of data must be followed by a “writing” operation, this effect will undoubtedly exacerbate the fatigue problem of ferroelectric materials and restrict the application of ferroelectricity as nonvolatile memories. However, due to the advantages such as nonvolatile storage (compared with DRAM), low power consumption (compared with the MRAM, FeRAM can be easily written by electric fields instead of large currents), high access speed and recording density, wide operating temperature, easy compatibility with the semiconductor planar technology and so on, the FeRAM is also a kind of important and ideal memory, and has continuously been concerned about and improved for applications.

### ***1.1.4 Comparison and Summary of Information Storage Technologies***

In summary, due to the advantage of expedient NDRO, magnetic recording is dominated and has played an important role in the information storage, while the limitations of its storage density and high writing power have prevented itself to be a perfect information storage technology. Although the MRAM has been developed and continuously improved based on the techniques of TMR and MTJ, it is still hard to overcome the disadvantages of lower recording density and higher energy consumption. In contrast, the FeRAM based on ferroelectric recording has the advantages of high recording density and low writing energy, while the

complex and DRO process greatly restrict its application as memory. Although the NDRO process of FeRAM based on the field effect transistor (FET) has been proposed and designed, the engineering model of FeRAM cell has not been fully understood yet, and the NDRO FeRAM is still on the way to be realized.

Therefore, the relevant researchers in this area have tried to combine the advantages of ferromagnetic recording and ferroelectric recording and overcome their disadvantages. As a result, new materials, new structures, and new concept of memories related to electric and magnetic recording have been continuously explored and designed, and a promising way is using the magnetoelectric (ME) coupling in multiferroic materials.

## 1.2 Multiferroic Materials and Magnetoelectric Effect

### 1.2.1 Definition and Properties of Multiferroic Materials

The concept of multiferroic was originally proposed by Schmid [18], and it has drawn much of the scientific interests and been extensively studied in recent years due to the novel physical phenomenon and great prospect in applications. Before understanding the concept of “Multiferroic,” we should first understand the concept of “Ferroic.” The concept of ferroic refers to a behavior that due to the interaction between the adjacent atoms or ions, the order of a certain physical parameter in materials spontaneously forms a regular structure with the physical parameter aligned in the same direction in some micro regions. Due to the existence of ferroic order, the parameter change of the ferroic materials with the external driving field exhibits a hysteretic behavior, such as the  $M-H$  and  $P-E$  loops in the ferromagnetic and ferroelectric materials [19], as shown in Fig. 1.9. As a result, the term of “Ferro” which represents a kind of physical order essentially has no relationship with the element of “Iron”.

Typical ferroic orders in materials include ferroelectric order, ferromagnetic order, ferrotoroidic order, and ferroelastic order. If the material exhibits two or more ferroic orders (such as ferroelectric order and ferromagnetic order), it is called multiferroic material. In addition to the coexistence of different ferroic orders, there is also a direct or an indirect coupling between the ferroic orders of multiferroic materials [20], as shown in Fig. 1.10.

Due to the coupling between the different ferroic orders, some interesting and useful physical phenomena can be produced. Such as the coupling between ferroelectric order and ferroelastic order can produce piezoelectric/converse piezoelectric effect, which plays a very important role in electromechanical conversion; the coupling between the ferromagnetic order and ferroelastic order can produce the magnetostriction/converse magnetostriction effect, which has important applications in the magnetic sensor; the coupling between the ferromagnetic order and ferroelectric order can produce new ME/converse ME effect, which will lead to a new generation of energy-efficient memory and has been extensively studied.

**Fig. 1.9** Different kind of “Ferroic” order in materials [19] (© IOP Publishing. Reproduced by permission of IOP Publishing. All rights reserved)

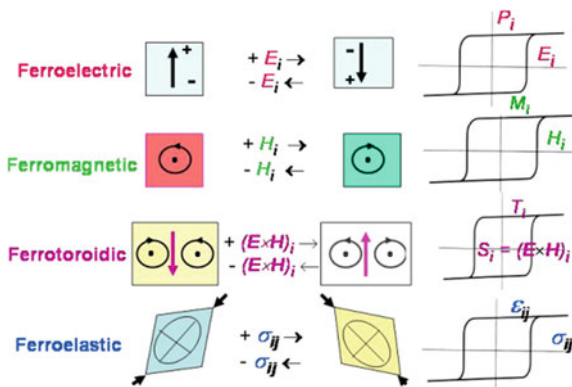
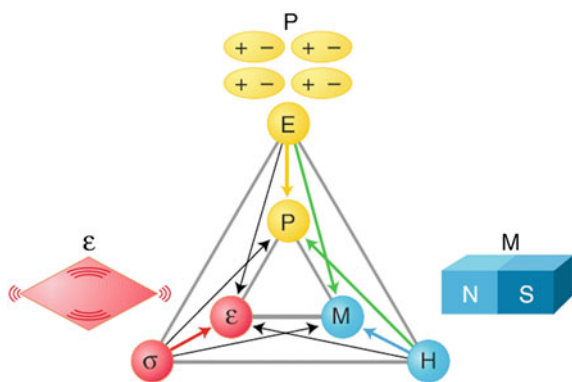


**Fig. 1.10** Coexistence of different ferroic orders and the mutual coupling (From Ref. [20]. Reprinted with permission from AAAS)



Since the presence of ferroelastic order is always accompanied by the ferroelectric order, the concept of multiferroic order mainly refers to coexistence and coupling between the magnetic order and the ferroelectric order. It should be emphasized that the coexistence of the different ferroic orders and the coupling effects in multiferroic materials enable us to manipulate the physical parameters in some new dimensions. For example, an applied electric field can not only induce or change the polarization in the ferroelectric materials, but also induce or change the magnetization in the multiferroic materials. Similarly, an external magnetic field can not only induce or change the magnetization in the ferromagnetic materials, but also induce or change the polarization in the multiferroic materials [21], as shown in Fig. 1.11. This magnetoelectric (ME) coupling between the magnetic order and ferroelectric order involves not only interesting physical issue in strongly correlated electron systems, but also significant applications in designing for the next generation multifunctional electronic devices, i.e., providing the opportunity of combining the advantages of the FeRAM and MRAM to realize high-speed, low power consumption, and nondestructive memory with the characteristics of electrical writing and magnetic reading [22–25].

**Fig. 1.11** Magnetoelectric coupling in multiferroic materials (Reprinted from Ref. [21], © 2007, with permission from Elsevier)

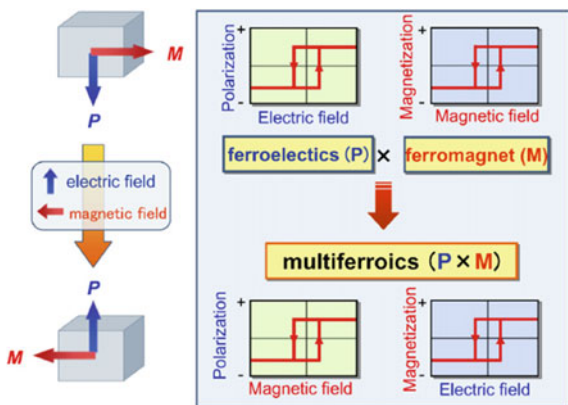
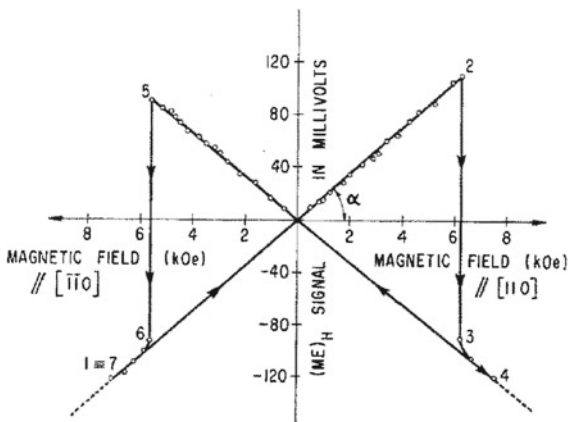


**Fig. 1.12** The magnetoelectric effect in the  $\text{Ni}_3\text{B}_7\text{O}_{13}\text{I}$  crystal (Reprinted with permission from Ref. [26]. © 1966, American Institute of Physics)

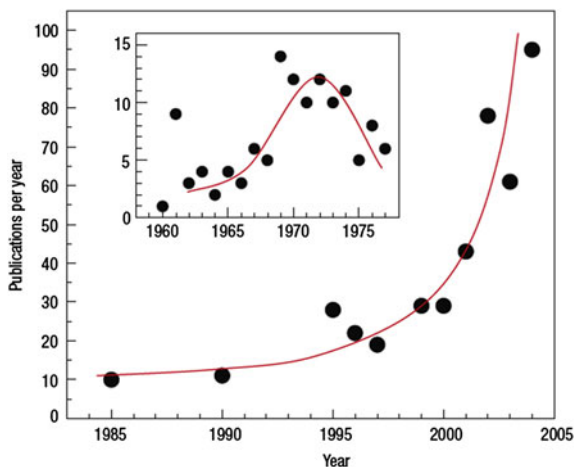


### 1.2.2 Historical Perspective of Multiferroics and ME Effect

The first multiferroic material was discovered by Schmid in 1966 [26], in which the borate crystal  $\text{Ni}_3\text{B}_7\text{O}_{13}\text{I}$  was found to exhibit ferromagnetic and ferroelectric order below 60 K. It was also found that there is an ME coupling effect in the system—the applied magnetic field can switch the sign of an electric signal, and this effect was also known as the ME switch effect, as shown in Fig. 1.12.

After the discovery of the first multiferroic material and the ME effect, some new multiferroic materials have been found and reported [27, 28]. However, the ferromagnetism, ferroelectricity, and ME coupling in these systems were too weak to be used in applications, and the experimental methods to investigate the ME coupling as well as the related theory to understand the microscopic mechanism of multiferroic were very limited. As a result, the research of multiferroic materials had been in the doldrums in the next two decades. Until recent years, due to the advances of experimental technologies (such as the thin film preparation technology and the

**Fig. 1.13** The number of published papers related multiferroic (Reprinted by permission from Macmillan Publishers Ltd: Ref. [25], © 2007 and Ref. [30] © IOP Publishing. Reproduced by permission of IOP Publishing. All rights reserved)



microscopic characterization method) as well as a deep understanding of the coexistence and coupling of the magnetic order and ferroelectric order in a single-phase material [21], a lot of important discoveries have been made in the rhombohedral ferroelectric structures and rare earth manganese oxides, and the research of multiferroic materials revivals and becomes an important issue in physics and material science, as shown in Fig. 1.13.

### 1.2.3 Origin and Classification of Multiferroicity

According to the definition, multiferroic materials require coexistence and coupling of different ferroic orders (such as the ferromagnetic order and the ferroelectric order). As a matter of fact, the ferromagnetic and ferroelectric orders are inherently mutually exclusive, as expounded by Hill in 2000 [29]. Generally speaking, the ferromagnetic order requires atoms with unfilled  $3d$  orbitals to get unpaired electron for magnetic moments, while the ferroelectric order requires atoms with filled or empty  $3d$  orbitals to facilitate the formation of a covalent bond and result in an offset effect of the center ion. As a result, the ferromagnetic and ferroelectric order can hardly coexist in the same material. Therefore, multiferroic materials are very rare, with the common case of antiferromagnetic and ferroelectric orders coexisting. In 2006, Eerenstein et al. published a review article in *Nature* to propose the idea of looking for multiferroic materials and magnetic coupling effects from the magnetic and electrical materials [24], as shown in Fig. 1.14.

The interplay between the electric and magnetic phenomena can be traced back to the year 1820, when Oster happened to find that a magnetic needle can be disturbed by the current in a wire. The electromagnetic phenomenon was further investigated by Ampere and Faraday, and finally completed by Maxwell's equation in the 1860s, as the discipline of electromagnetism in modern physics.

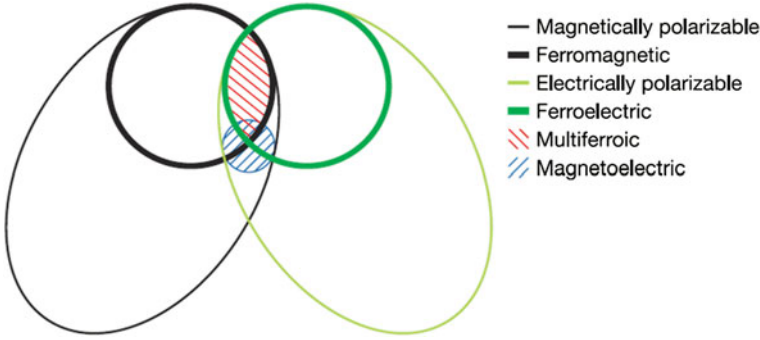


**Fig. 1.14** Relationship between multiferroic materials and magnetoelectric materials (Reprinted by permission from Macmillan Publishers Ltd.: Ref. [24], © 2006)

Different from the dynamic interaction between electric field and magnetic field in electromagnetism, the ME effect in multiferroic materials is a kind of static coupling relating the spin–phonon interaction, the electron–phonon interaction, and the correlation between electrons and multiple elementary excitations. Due to the inherent exclusion between the magnetic and ferroelectric orders, the investigation of coexistence and coupling effect between the magnetic and ferroelectric orders in multiferroic materials is an interesting and important physical issue.

The theory used to describe the multiferroic system and the ME coupling effect is Landau theory [24, 30]. The free energy  $F$  of a multiferroic material under external electric field  $\mathbf{E}$  and magnetic field  $\mathbf{H}$  can be expanded as follows:

$$\begin{aligned}
 -F(\mathbf{E}, \mathbf{H}) = & \frac{1}{2} \varepsilon_0 \varepsilon_{ij} E_i E_j + \frac{1}{2} \mu_0 \mu_{ij} H_i H_j + \alpha_{ij} E_i H_j \\
 & + \frac{\beta_{ijk}}{2} E_i H_j H_k + \frac{\gamma_{ijk}}{2} H_i E_j E_k + \dots
 \end{aligned} \quad (1.1)$$

where  $\varepsilon_0 \varepsilon_{ij}$  and  $\mu_0 \mu_{ij}$  represent the dielectric constant and magnetic susceptibility of the material, and  $\alpha_{ij}$ ,  $\beta_{ijk}$ ,  $\gamma_{ijk}$  represent the first-order and higher order ME coupling coefficients. Different components of the electric field and magnetic field are denoted by  $E_i$ ,  $E_j$ ,  $E_k$ , and  $H_i$ ,  $H_j$ ,  $H_k$ , respectively. Differentiating the Eq. 1.1, one can get the following expression:

$$P_i = \alpha_{ij} H_j + \frac{\beta_{ijk}}{2} H_j H_k + \dots \quad (1.2)$$

$$\mu_0 M_i = \alpha_{ji} E_j + \frac{\gamma_{ijk}}{2} E_j E_k + \dots \quad (1.3)$$

From Eqs. (1.2) and (1.3), one can see the interaction between the ferroelectric order and the ferromagnetic order in multiferroic materials. The effect of magnetic field inducing or controlling of the polarization ( $P$  in Eq. 1.2) is called the ME effect, and the effect of electric field inducing or controlling of the magnetization

( $M$  in Eq. 1.3) is called the converse ME effect. Since  $\beta_{ijk}$  and  $\gamma_{ijk}$  are the higher order ME coupling coefficients, which are typically much smaller than the first-order ME coupling coefficient ( $\alpha_{ij}$ ),  $\alpha_{ij}$  is customarily known as the ME coupling coefficient.

According to the research of multiferroic materials in recent years [31–33], the multiferroic materials can generally be divided into two categories: one is single-phase multiferroic materials, and the other is compound multiferroic system. According to the origin of the multiferroic order, single-phase multiferroic materials mainly include the following categories:

*Lone-pair-electrons-induced multiferroicity.* This kind of multiferroic materials are mainly composed of Bi and elements from IV to VI group with a perovskite  $ABO_3$  structure (e.g.,  $\text{BiMnO}_3$  [34] and  $\text{BiFeO}_3$  [35, 36]). The ferroelectricity originates from the orbital hybridization between the  $6s^2$  lone pair electrons of  $\text{Bi}^{3+}$  ion at  $A$ -site and  $2p$  electrons of  $\text{O}^{2-}$ , and the magnetic order is induced by the  $\text{Mn}^{3+}$  or  $\text{Fe}^{3+}$  ions at  $B$ -site. It should be noticed that, due to the coexistence of ferroelectric order and antiferromagnetic order as well as the ME coupling effect at room temperature,  $\text{BiFeO}_3$  is an important multiferroic material and has been intensively studied in recent years, with many important results reported by Ramesh's group.

$\text{BiFeO}_3$  exhibits a rhombohedral perovskite structure at room temperature, with a distortion that the  $\text{Bi}^{3+}$  ion shifts along the  $[111]$  direction referring to the surrounding oxygen ions of the cubic unit cell and the oxygen octahedron distorts around the  $[111]$  axis. However, this distortion of the  $\text{BiFeO}_3$  from the cubic structure is tiny, and the unit cell of  $\text{BiFeO}_3$  can be considered as a pseudocubic structure. Due to the rhombohedral distortion, the ferroelectricity is generated, with spontaneous polarizations along the  $\langle 111 \rangle$  directions, as shown in Fig. 1.15.

The magnetic order of  $\text{BiFeO}_3$  at ground state is antiferromagnetism, and the ME coupling is relatively weak, for the ferroelectricity and antiferromagnetism originate from different type of units (ions). However, the Dzyaloshinskii–Moriya (DM) interaction requires the polarization vector ( $\mathbf{P}$ ) and the uncompensated magnetic vector ( $\mathbf{M}$ ) to satisfy a certain relationship [35, 37], as shown in Fig. 1.15. As a result, when the polarization is switched by an external electric field, the plane of the magnetic vector will also be changed, resulting in the coupling effect between the magnetic domain and the ferroelectric domain, as shown in Fig. 1.16. What is more, the  $\text{BiFeO}_3$  also exhibits interesting behaviors in the structural, ferroelectric/ferroelastic, optical and electrical properties according to reports [36, 38, 39], indicating the promising applications.

*Geometric-configuration-induced multiferroicity.* These kinds of multiferroic materials mainly include hexagonal manganites ( $R\text{MnO}_3$ , where the term  $R$  represents rare-earth elements: Ho, Lu, or Y) [40, 41], in which the ferroelectricity are induced by the inclination of  $\text{MnO}_5$  triangular bipyramids due to electrostatic effect, and the magnetic order originates from the  $\text{Mn}^{3+}$  ions at  $B$ -site. Since the  $\text{Mn}^{3+}$  ion has a two-dimensional spin frustration configuration, the materials

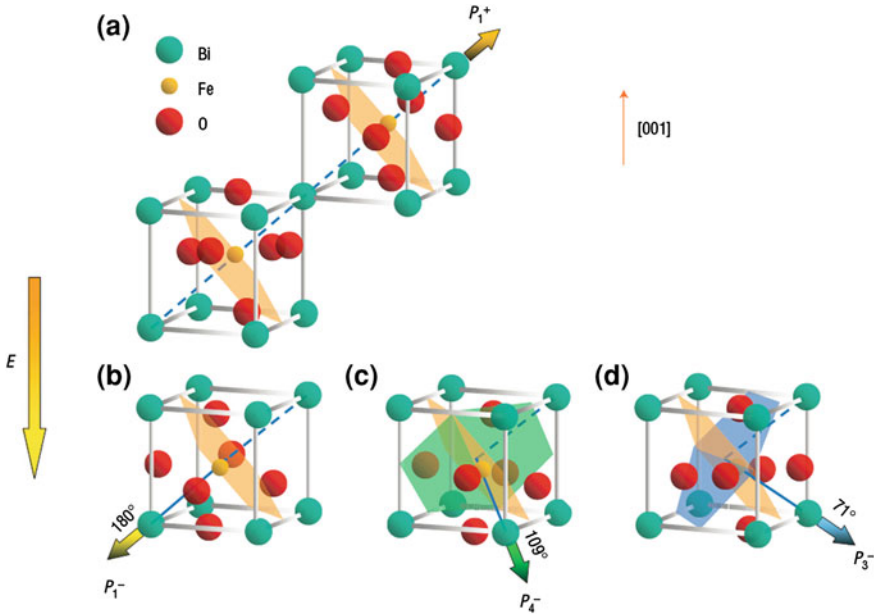


**Fig. 1.15** The pseudocubic unit cell and spontaneous polarizations of BiFeO<sub>3</sub>: **a** polarization before electrical poling, **b–d** 180°/109°/71° polarization switching under external electric field (Reprinted by permission from Macmillan Publishers Ltd.: Ref. [35], © 2006)

exhibit magnetic order only at low temperature. However, the ferroelectricity is available at room temperature and can be observed by scanning probe microscopy (SPM), as shown in Fig. 1.17. Comparing with other multiferroic materials, the ME coupling between the ferroelectric and magnetic orders are relatively strong in these hexagonal manganites, and the magnetic order can be easily controlled by an external electric field at low temperature, which makes them to be important multiferroic materials with potential applications.

*Spiral spin-order-induced multiferroicity.* These kind of multiferroic materials mainly include orthogonal manganites ( $RMnO_3$ , where the term  $R$  represents rare-earth elements: Tb, Dy, or Y), in which the ferroelectricity originates from the lattice modulation caused by the magnetoelastic coupling in the spiral spin order [42–44], as shown in Fig. 1.18. Since the ferroelectricity in this system is induced by the magnetic order, the effect of magnetic field control of polarization is very obvious, while the value of the saturated polarization is relatively small.

*Charge-order-induced multiferroicity.* These kind of multiferroic materials mainly include strongly correlated electron systems, such as  $LuFe_2O_4$  and  $R_{1-x}Ca_xMnO_3$  (where the term  $R$  represents rare-earth elements: La or Pr). The ions of  $Fe^{2+}$  and  $Fe^{3+}$  (or  $Mn^{3+}$  and  $Mn^{4+}$ ) in these systems will form a strong correlation and result

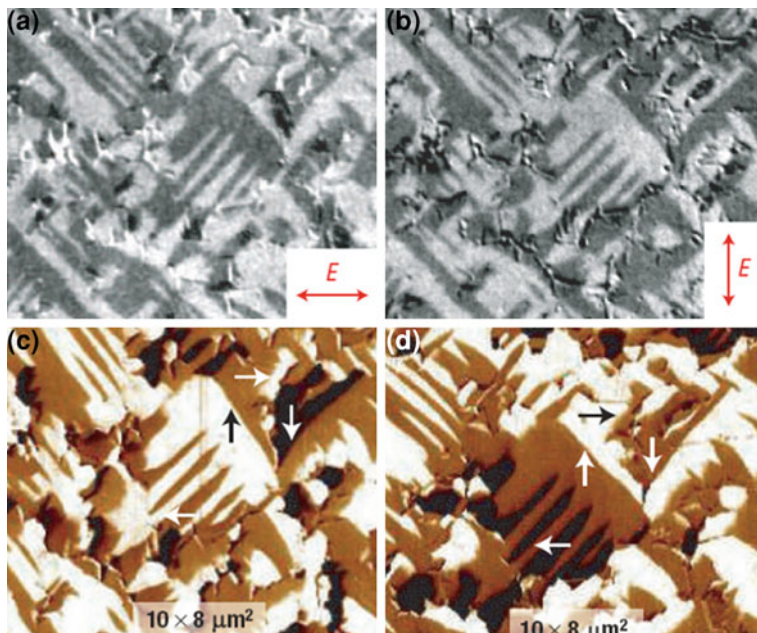


**Fig. 1.16** The ME coupling between the magnetic domain (PEEM images **a** before and **b** after 90° in-plane rotation in the up panel) and ferroelectric domain (in-plane PFM images **c** before and **d** after 90° in-plane rotation in the down panel) in BiFeO<sub>3</sub> (Reprinted by permission from Macmillan Publishers Ltd.: Ref. [35], © 2006)

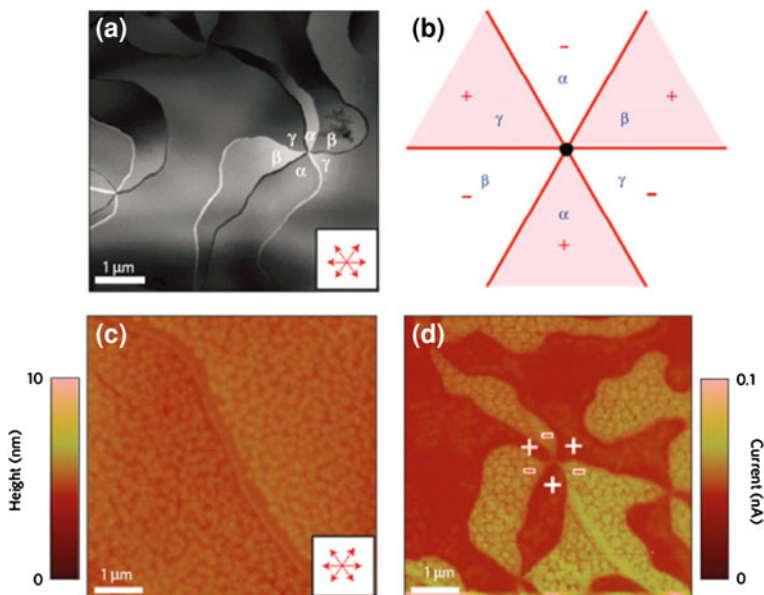


**Fig. 1.17** The ferroelectric domains of YMnO<sub>3</sub>: **a** TEM dark-field image, **b** proposed cloverleaf configuration, **c** topography and **d** C-AFM image of the of six antiphase/ferroelectric domains (Reprinted by permission from Macmillan Publishers Ltd.: Ref. [41], © 2010)

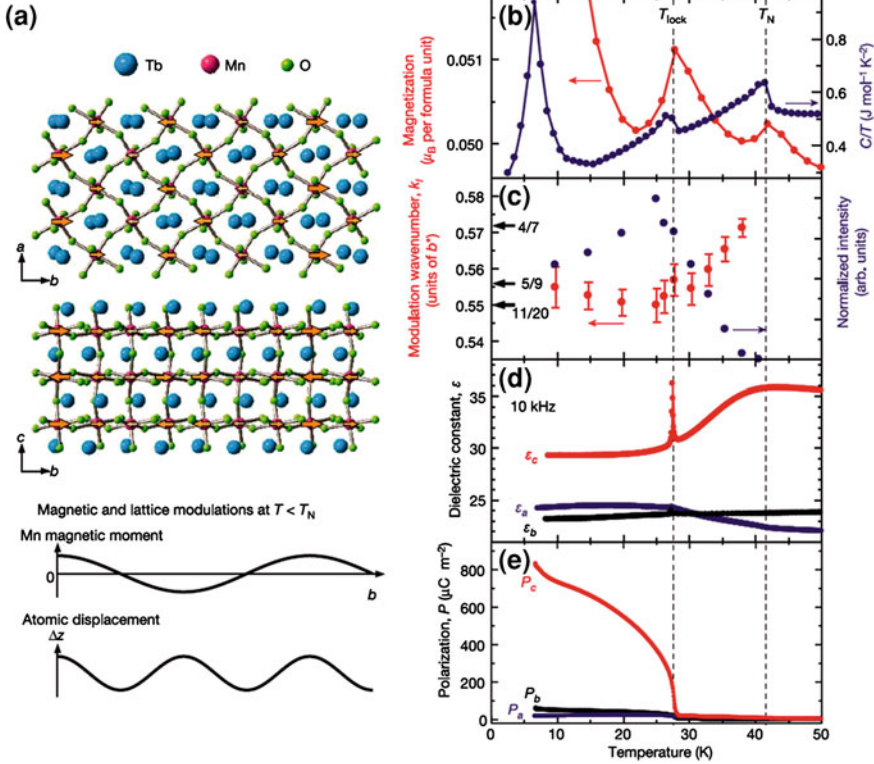


**Fig. 1.18** The ferroelectricity induced by lattice modulation due to the magnetoelastic coupling: **a** crystal structure and lattice modulation below  $T_N$ , **b** magnetization and specific heat, **c** lattice modulation, **d** dielectric constant and **e** electric polarization of TbMnO<sub>3</sub> variation with temperature (Reprinted by permission from Macmillan Publishers Ltd.: Ref. [42], © 2003)

in the charge order state. The charge order, magnetic order, and orbital order in these materials couple with each other and lead to the formation of multiferroicity [45].

Theoretical work shows that the magnetic coupling coefficient  $\alpha_{ij}$  in the single-phase multiferroic materials is limited by the dielectric constant and magnetic susceptibility:  $\alpha_{ij}^2 \leq \epsilon_0 \mu_0 \epsilon_{ii} \mu_{jj}$  [46]. As a result, it is hard to get large ME coupling effects in single-phase multiferroic materials. The most effective way to enhance the ME coupling effect is employing the materials with large dielectric constant and magnetic susceptibility, such as the ferroelectric and ferromagnetic materials. Therefore, the investigation of multiferroicity and ME coupling based on ferromagnetic and ferroelectric materials or their composite structures is particularly important.

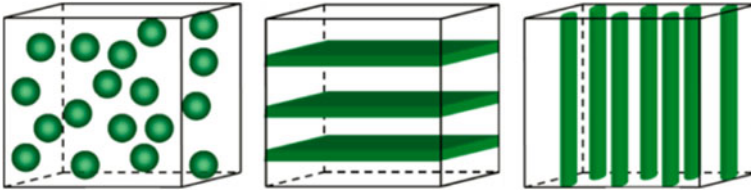


**Fig. 1.19** Different kinds of compounded multiferroic structure: 0–3 type (*left*), 2–2 type (*middle*) and 1–3 type (*right*) (Reprinted with permission from Ref. [47]. © 2008, American Institute of Physics)

## 1.3 Compounded Multiferroic Structures and Electric-Field Control of Magnetization

### 1.3.1 Classification of Compounded Multiferroic Structures

As discussed above, the ferromagnetic and ferroelectric orders are mutually exclusive in the same material. As a result, the single-phase multiferroic materials are rare, especially in the case of room temperature multiferroic materials. On the other hand, the theoretical ME coupling coefficient of the single-phase multiferroic materials is restricted by the relation:  $\alpha_{ij}^2 \leq \epsilon_0 \mu_0 \epsilon_{ii} \mu_{jj}$ , and the ME effect is too small to meet the requirements of applications. However, the above restrictions do not exist in the composite system, and there are vast of ferromagnetic and ferroelectric materials at room temperature. Thus, the ferromagnetic/ferroelectric (FM/FE) artificial compounded structure provides an alternative route to achieve multiferroicity and has been extensively studied [47–51].

According to the configuration of connectivity, the compounded multiferroic materials can be generally divided into three categories: particulate composite structure (0–3 type), layered composite structure (2–2 type), and columnar composite structure (1–3 type), as shown in Fig. 1.19.

The 0–3 type multiferroic structure is essentially a composite polycrystalline with piezoelectric and magnetic grains inside, which can be prepared by the sol-gel method [52] or pulsed laser deposition (PLD) [53]. The typical form of the 0–3 type particulate composites is ferromagnetic particles or grains distributed over the ferroelectric bulk or film, exhibiting good  $M$ – $H$  and  $P$ – $E$  loops at room temperature, as shown in Fig. 1.20. However, the biggest defect in this structure is the leakage problem: If the magnetic particles gather together or connect with each other inside the ferroelectric phase, it will result in local low resistance and leakage of the whole sample, which hinders the effect of external electric field and the observation of the ME coupling [51].

The 1–3 type multiferroic structure is columnar fibers of one phase (e.g., FM) embedded in the other phase (e.g., FE) with a matrix form. A typical 1–3 type composite is  $\text{BaTiO}_3$ – $\text{CoFe}_2\text{O}_4$  (BTO–CFO) columnar nanostructures on  $\text{SrTiO}_3$

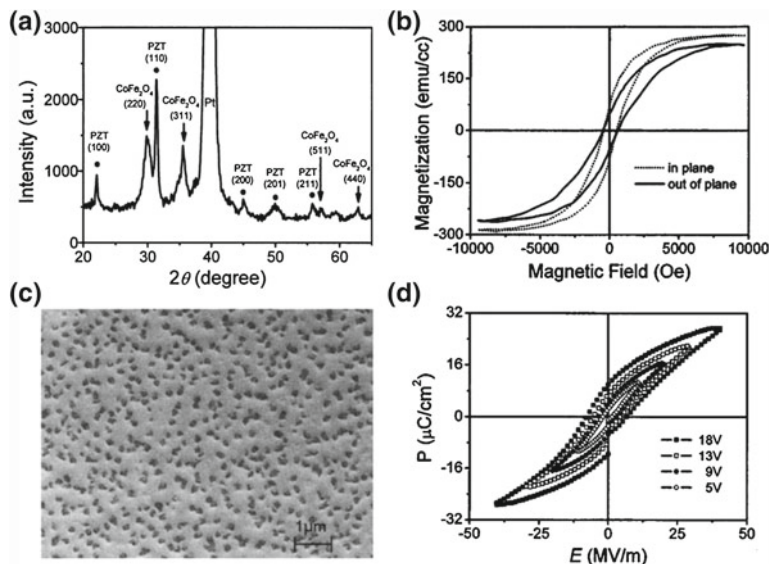


**Fig. 1.20** The **a** texture, **b** ferromagnetic property, **c** SEM image and **d** ferroelectric property of 0–3 type CFO-PZT particulate composite structure (Reprinted with permission from Ref. [52]. © 2005, American Institute of Physics)

substrate prepared by PLD method, as reported by Zheng et al. in 2003 [54]. A follow-up report shows that the magnetization can be locally reversed by switching the polarization [55], which gives the direct evidence electric control of magnetization in this system, as shown in Fig. 1.21. Besides, the ME coupling coefficient has also been quantitatively measured, and a large value up to 8–10 s/m has been achieved, which is several orders of magnitude larger than that of single-phase multiferroic materials. However, the problem of leakage also exists in this structure, which is a disadvantage for applications.

The 2–2 type multiferroic structure is a kind of laminate composites consisting of piezoelectric and magnetic layers, which can be divided into three subcategories: (i) The multilayer structure (such as  $[PZT/CZFO]_n$ ) prepared by the sol–gel [56] or the superlattice structure (such as  $R_{1-x}Ca_xMnO_3/Ba_{1-x}Sr_xTiO_3$ ) prepared by PLD [57, 58]. (ii) The double-layer structure (such as  $BaTiO_3/NiFe_2O_4$  (BTO/NFO)) epitaxial growth on the  $SrTiO_3$  substrate [59]. (iii) The ferromagnetic thin film deposited directly onto a ferroelectric single crystal or a ceramic substrate. Although the bilayer or multilayer composite structures can achieve a certain ME effect (as shown in Fig. 1.22), the “clamping” effect of the substrate onto the epitaxial ferroelectric thin film largely limits the strain effect of the FE film to achieve its fully capability [60–62]. What is more, large area and high-quality ferroelectric thin films are needed to eliminate the leakage current, which is very difficult to realize in the

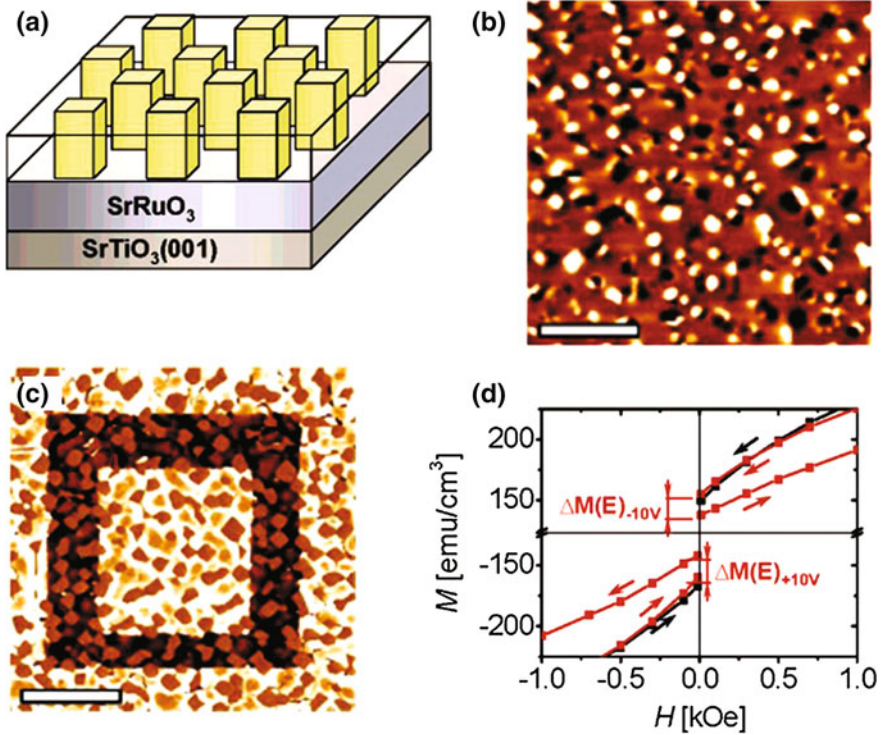


**Fig. 1.21** The **a** schematic BTO–CFO columnar nanostructure, **b** magnetic domain structure, **c** ferroelectric domain structure and **d** its electrical control of magnetization (Reprinted with the permission from Ref. [55]. © 2005 American Chemical Society)

sample preparation. Considering the “clamping” effect and leakage problem in the 2–2 type multiferroic structures, the combination of a ferromagnetic thin film deposited on top of a ferroelectric substrate is an optimal choice in the compounded multiferroic structure, in which large ME coupling can be easily achieved.

An important issue in the investigation of the multiferroic materials and the ME coupling is the electrical control of magnetization. In addition to finding the interesting physical mechanism of the ME effect, the aim of the research-related multiferroic materials mainly focuses on the application—the electric writing and magnetic reading spintronic device at room temperature, which is a critical technique for the next-generation energy-efficient memory based on the multiferroic materials in future. As a result, the investigation of electric-field control of magnetization in multiferroic materials or structures is important, and becomes the hot spots of the scientific research in recent years.

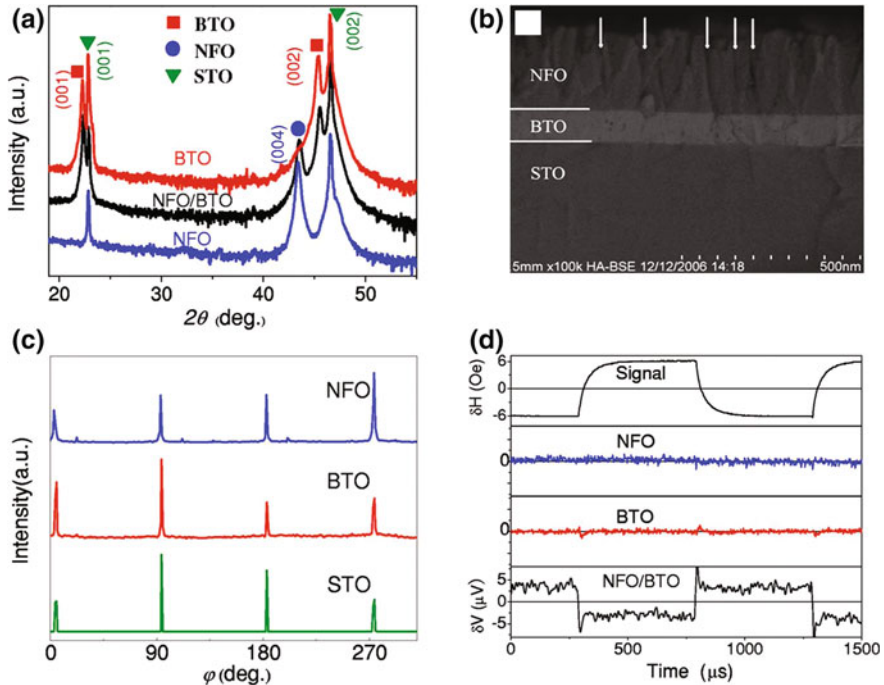


**Fig. 1.22** The **a** texture, **b** SEM image, **c** crystal symmetry of the NFO/BTO bilayer FM/FE multiferroic structure and **d** the ME coupling (Reprinted with permission from Ref. [59]. © 2007, American Institute of Physics)

### 1.3.2 Compounded Multiferroic Heterostructures and Electric-Field Control of Magnetization

According to the mechanism of ME coupling, the main progresses in the overall researches [50, 63, 64] of the electric-field control of magnetization in the compounded multiferroic structures can be divided into three categories as following.

*Exchange Bias-Mediated ME coupling.* The typical structure of the exchange bias-mediated multiferroic system consists of a ferromagnetic thin film deposited on top of a single-phase multiferroic material. The exchange bias effect originates from the exchange interaction between the ferromagnetic order and the antiferromagnetic order at the interface of the FM thin film and the multiferroic layer. Since the ferroelectric order and antiferromagnetic order are coupled with each other in the multiferroic materials, the electrical control of ferromagnetism can be achieved, mediated by the ferroelectric–antiferromagnetic coupling in the multiferroic layer and the antiferromagnetic–ferromagnetic exchange interaction at the interface [65], as shown in Fig. 1.23. In fact, this kind of ME coupling belongs to the ME effect in the single-phase multiferroic materials. However, the single-phase multiferroics are

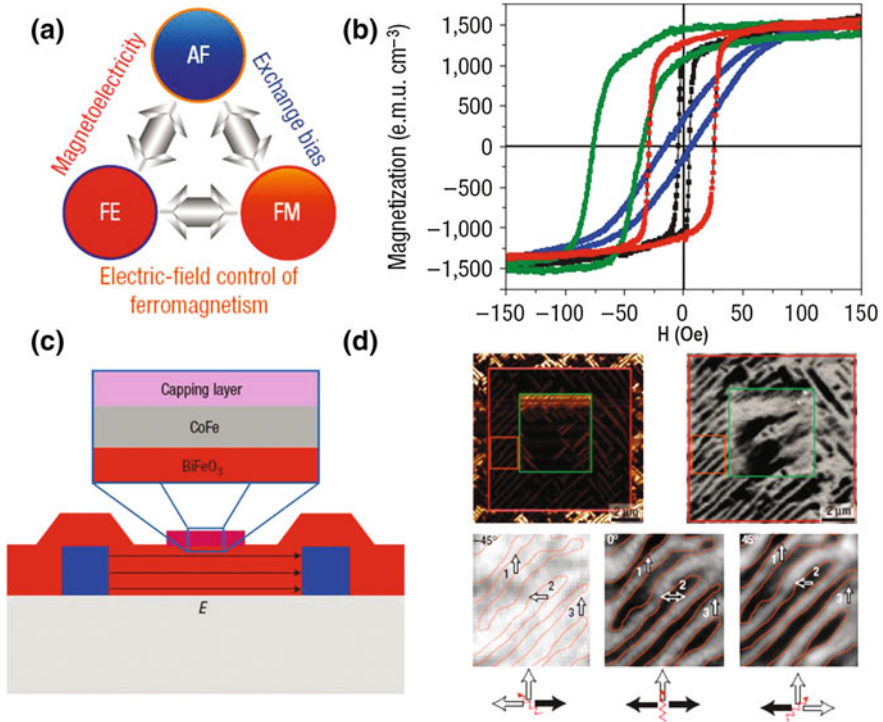


**Fig. 1.23** The **a** exchange bias-mediated ME coupling, **b** exchange bias effect in the **c** CoFe/BiFeO<sub>3</sub> multiferroic structure and **d** the ME coupling between the FE/FM domains (Reprinted by permission from Macmillan Publishers Ltd: Ref. [66], © 2008)

rare, with the common case that the ferroelectric order coexists with the antiferromagnetic order instead of ferromagnetic order. Therefore, the ME coupling of some single-phase multiferroic materials should be mediated by the exchange bias effect in the composite structure.

Due to the scarcity of single-phase multiferroic materials and strict interface requirement of exchange bias effect [67], the cases of electrical control of magnetization mediated by the exchange bias effect are rare, e.g., ME coupling in CoFe/BiFeO<sub>3</sub> at room temperature [66] and ME coupling in Py/YMnO<sub>3</sub> at low temperature [68]. On the other hand, the exchange bias often exhibits training effect, which is disadvantageous for the ME coupling in the exchange bias-mediated multiferroic system.

*Interfacial Charge-Mediated ME Coupling.* This kind of ME effect typically appears in a field-effect-transistor (FET)-like heterostructure consisting of an ultrathin ferromagnetic film and a ferroelectric layer. The polarizations of the ferroelectric layer can be switched by an external electric field, which results in the accumulation or dissipation of spin-related charges at the interface and produces a change in the interfacial magnetization as a consequence. Typical work of the

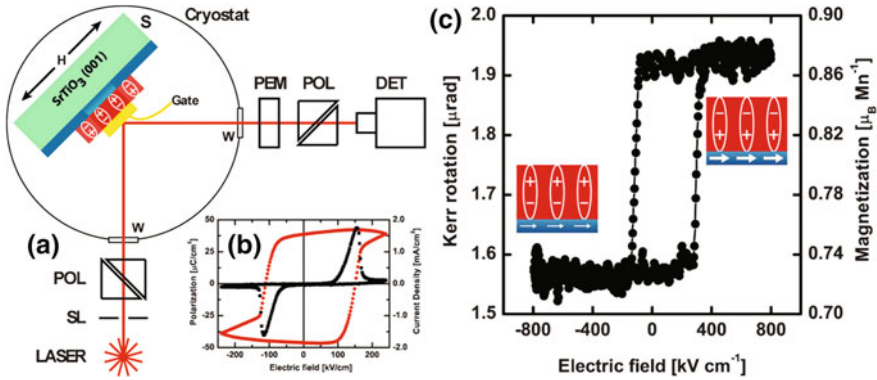


**Fig. 1.24** The charge-mediated ME coupling in LSMO/PZT multiferroic structure: **a** measurement configuration, **b** P-E loop of the PZT layer and **c** charge-mediated non-volatile electric field control of magnetization (Reproduced from Ref. [69] by permission of John Wiley & Sons Ltd)

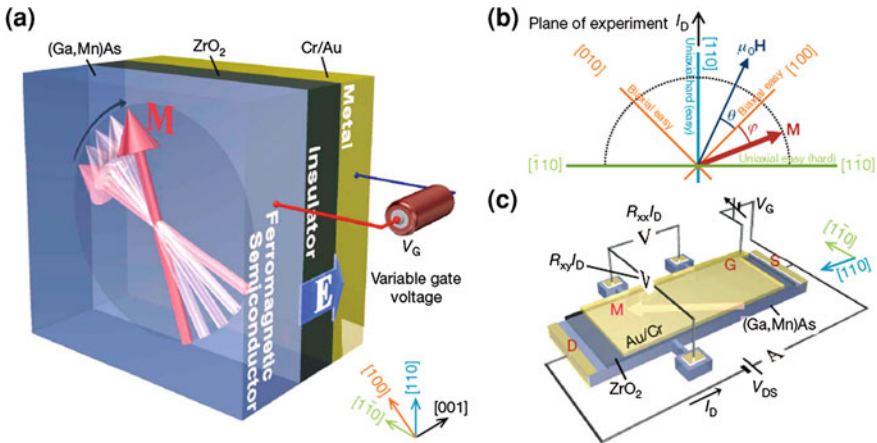


**Fig. 1.25** The electrical manipulation of the direction of magnetization in (Ga, Mn)As: **a** measurement configuration, **b** vector diagram of the magnetization  $M$  as well as external magnetic field  $H$  and **c** the Hall-bar-shaped device (Reprinted by permission from Macmillan Publishers Ltd: Ref. [70], © 2008)

charge-mediated multiferroic heterostructures is reported in the colossal magneto-resistance (CMR) system with a 4 nm thick nearly insulated  $\text{La}_{0.8}\text{Sr}_{0.2}\text{MnO}_3$  film [69], as shown in Fig. 1.24. What is more, similar results have also been reported in the dilute magnetic semiconductor (DMS) material [70, 71], as shown in Fig. 1.25.

Since the mechanism of the charge-mediated ME coupling is related to the ferroelectric polarization, the electrical control of magnetization exhibits *loop-like* behavior as the ferroelectric hysteresis loop, which is useful as a new type of nonvolatile information storage memory for the next generation. However, the

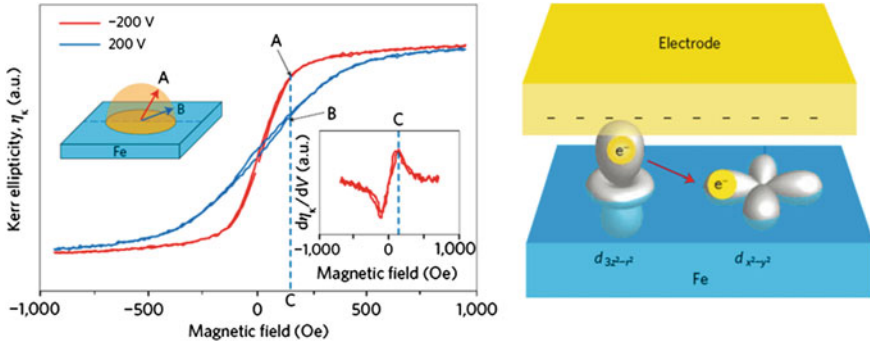


**Fig. 1.26** The Electric-field control of magnetization (*left*) and  $d$  elections (*right*) of iron film (Reprinted by permission from Macmillan Publishers Ltd: Ref. [72], © 2009)

FET configuration requires the ferromagnetic film with low carrier concentration (semiconductor or insulator), in order to deplete the whole ferromagnetic layer. But on the other hand, the ferromagnetic materials are often good conductors with high carrier concentration. As a result, appropriate ferromagnetic materials which can be used in the charge-mediated multiferroic structures are limited and the ME coupling effects are often realized at low temperatures, which are disadvantageous for applications.

It should be mentioned that there is an important work in the interfacial charge-mediated system which achieves electric-field control of magnetic anisotropy of an iron film with the thickness of a few atomic layers at room temperature [72]. The ME coupling mechanism is considered such that the applied electric field will modulate a number of unpaired  $d$  electrons at the surface and thereby changes the magneto-crystalline anisotropy in the iron film, as shown in Fig. 1.26. However, huge electric fields are required to change the orbital momentum of the electrons of the FM materials and only a few superficial atomic layers of the FM film can be modulated in this structure, which is hardly to be used in applications and other similar works are mainly of the theoretical calculations and propositions [73, 74].

*Strain-Mediated ME Coupling.* The basic principle of the strain-mediated ME coupling is that an external electric field will change the shape (expansion or contraction) of the ferroelectric phase through the electrostriction or inverse piezoelectric effect, and the strain will be transferred on to the ferromagnetic phase, which will alter the magnetic anisotropy of the ferromagnetic materials via the piezomagnetic effect or inverse magnetostriction, as shown in Fig. 1.27.

Different from the limited regulation in the single-phase multiferroic materials, the ME coupling coefficient in this system can be expressed as follows [75]:

$$\alpha_H = \frac{\text{magnetic}}{\text{mechanical}} \times \frac{\text{mechanical}}{\text{electrical}} \quad (1.4)$$

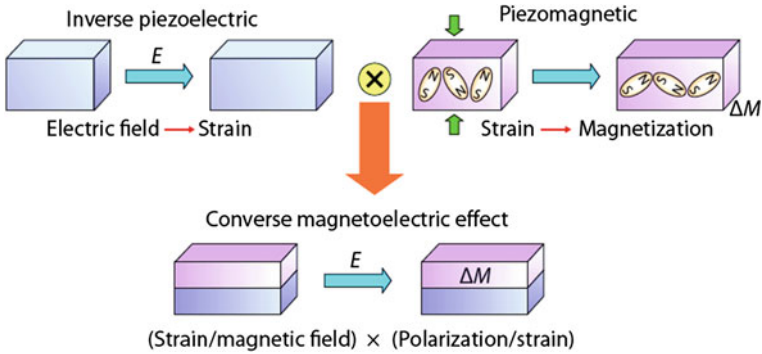


**Fig. 1.27** The electric-field control of magnetization in the strain-mediated system (Reprinted by permission from Macmillan Publishers Ltd: Ref. [64], © 2010)

$$\alpha_E = \frac{\text{electrical}}{\text{mechanical}} \times \frac{\text{mechanical}}{\text{magnetic}} \quad (1.5)$$

Seeing from the above formulas, as long as one can choose FE materials with large electrostriction (or piezoelectric effect) and FM materials with large piezomagnetic effect (or magnetostriction) for compounding, large ME coupling coefficients can be gotten. Although the coupling mechanism for the strain-mediated multiferroic system is only a simple mechanical coupling at the interface, the vast choices of ferroelectric/piezoelectric materials and ferromagnetic materials with high-performance at room temperature have made it to be the main route in the electrical control of magnetization and important for applications in the future. Several typical works related to electrical control of magnetization in the strain-mediated multiferroic system will be discussed as following.

The first representative work in this area was reported by Eerenstein et al., in which a 40 nm thick  $\text{La}_{0.67}\text{Sr}_{0.33}\text{MnO}_3$  (LSMO) film was epitaxially grown on top of the  $\text{BaTiO}_3$  (BTO) substrate, and nonvolatile electric-field control of magnetization was observed [76]. When the electric field applied on the sample is gradually increased and reaches a certain value, the magnetization will decrease sharply. This change of magnetization remains after removing the electric field, as shown in Fig. 1.28.

The mechanism for this phenomenon is understood as follows: The BTO is a kind of FE material with tetragonal phase at room temperature, and it exhibits two kinds of domain orientations (i.e., *a*-domain and *c*-domain) in the single crystal without an electric field. When poled by an external electric field, the *a*-domain inside of the BTO single crystal substrate occurs a 90° domain switching and develops into the *c*-domain. As a result, an in-plane local stress is generated by the domain switching, which is transferred onto the LSMO film by strain coupling at the interface and change the magnetization of sample. Since the switching of the domains in ferroelectric materials are irreversible (or nonvolatile), the electrical control of magnetization is also irreversible (or nonvolatile), as a consequence.

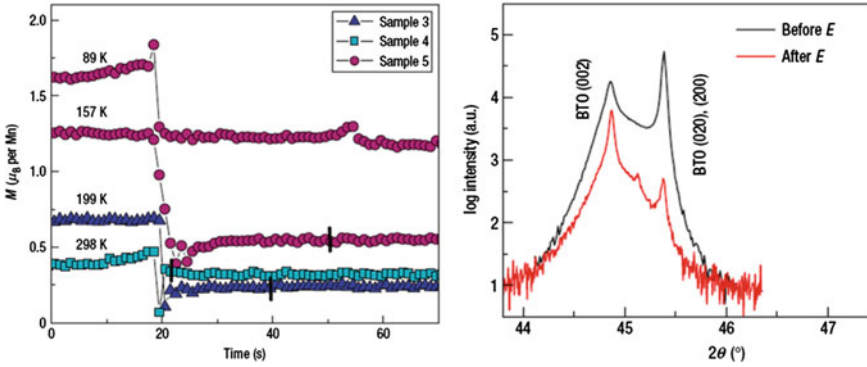


**Fig. 1.28** The nonvolatile electrical control of magnetization (*left*) and non-180 $^\circ$  FE domain switching (*right*) in the LSMO/BTO structure (Reprinted by permission from Macmillan Publishers Ltd: Ref. [76], © 2007)

Although the reproduction of this ME behavior requires a series of complicated processes (such as changing the temperature) to reset the sample, and BTO single crystal itself easily becomes fatigued and broken after repeatedly poled by high electric field, this work first introduces the idea of nonvolatile electrical control of magnetization by means of certain kind of ferroelectric domain switching (or reorientation), which is important for applications. What is more, this work also first brings forward the definition of static ME coupling coefficient in experiment:  $\alpha = (\partial P / \partial P)_E = \mu_0 (\partial M / \partial E)_H = \mu_0 \Delta M / \Delta E$ , and the obtained maximum value of  $\alpha$  in the system reaches  $2.3 \times 10^{-7}$  m/s, which is much higher than the results in the single-phase multiferroic materials.

At the same time, Thiele et al. also reported the investigation of electric-field control of magnetization in the compounded multiferroic heterostructure consisting of the (001)-oriented  $\text{Pb}(\text{Mg}_{1/3}\text{Nb}_{2/3})_{0.72}\text{Ti}_{0.28}\text{O}_3$  (PMN-PT) single crystal and the epitaxial manganese oxide  $\text{La}_{0.7}\text{A}_{0.3}\text{MnO}_3$  ( $A = \text{Sr}, \text{Ca}$ ) film [77]. In their work, they have first measured the in-plane strain of PMN-PT at room temperature, which exhibits *butterfly-like* strain–electric field ( $S$ – $E$ ) curve. Then the magnetization of LSMO was measured under different electric fields, and the magnetic response to the electrical stimulation also exhibits a similar *butterfly* behavior, corresponding to the  $S$ – $E$  curve, as shown in Fig. 1.29.

The mechanism for the ME coupling in this structure is considered as that the piezoelectric PMN-PT substrate generates uniform in-plane biaxial strain under electric field, which is transferred onto the epitaxial LSMO film and changes the length and angle of the Mn–O bond, resulting in the modification of magnetization and Curie temperature of the LSMO film. The maximum ME coupling coefficient in this structure is  $6.23 \times 10^{-8}$  m/s, which is comparable to the result in LSMO/BTO structure. Notably, different from the work in LSMO/BTO, the electric-field control of magnetization in LSMO/PMN-PT is completely reversible without the complicated temperature changing process, which exhibits the advantages of easy

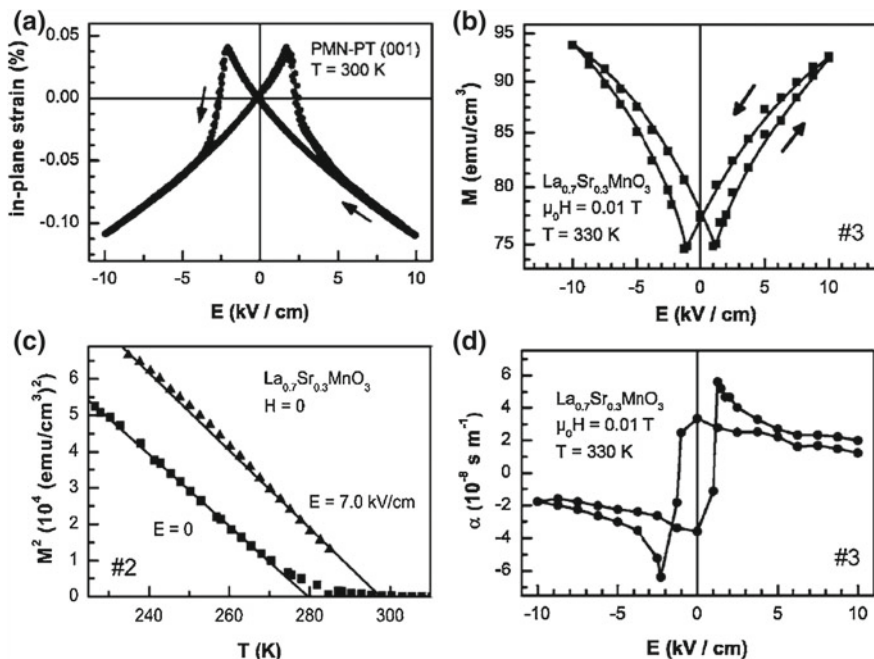


**Fig. 1.29** The **a** in-plane S–E curve of the PMN-PT substrate, the electrical control of **b** magnetization as well as **c** Curie temperature of the LSMO film and **d** the deduced ME coupling coefficient (Reprinted with permission from Ref. [77]. © 2007 by American Physical Society)

operability in practical applications and initiates a large number of similar studies in the compounded multiferroic heterostructures, such as Fe/BaTiO<sub>3</sub> [78, 79], FeCoV/PZN-PT [80], CoFe<sub>2</sub>O<sub>4</sub>/PMN-PT [81], FeGaB/PZN-PT [82], Fe<sub>3</sub>O<sub>4</sub>/PZT, and Fe<sub>3</sub>O<sub>4</sub>/PMN-PT [83], ZFO/PMN-PT [84], FeBSiC/PZT [85], Ni/BaTiO<sub>3</sub> [86], Ni/PZT, Fe–Ge/PZT, and Fe–Ge/BSPT [87], Ni/PMN-PT/Ni [88], and many other heterostructures. In another aspect, Hu et al. has carried out some theoretical research related to the strain-mediated multiferroic structures and presents some quantitative results [89, 90].

Since nearly all the S–E curves of the ferroelectric material under bipolar electric field exhibit similar *butterfly-like* behaviors as shown in Fig. 1.29a, almost all of the behaviors of electrical modulation of magnetism (magnetization or coercive field) in these strain-mediated system also exhibit similar *butterfly-like* curves as shown in Fig. 1.29b. The biggest problem of this type of ME behavior is that the electrical modulation of magnetization is “volatile,” that is, when the electric field applied onto the sample returns to zero, the change of magnetization tuned by electric field vanishes due to the strain restoring to the initial state without electric field, which is disadvantageous for applications. Later, Geprags et al. [86] and Wu et al. [91] report the reversible and nonvolatile ME effects under unipolar electric field in the structures of Ni/BaTiO<sub>3</sub> and Ni/PMN-PT(011), respectively,

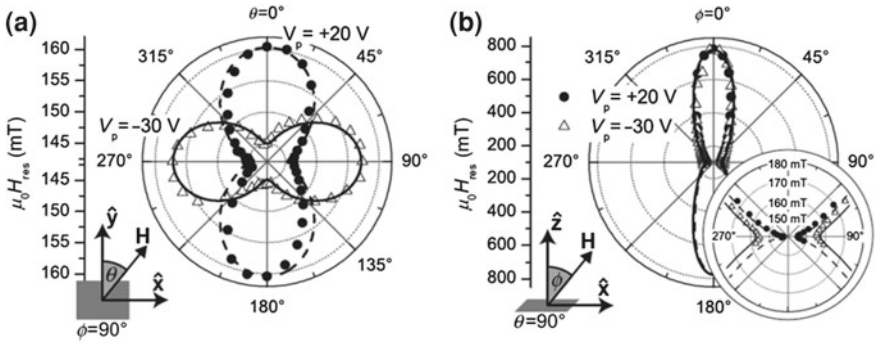


**Fig. 1.30** Investigation of the electrical control of magnetic anisotropy **a** parallel and **b** perpendicular to the sample plane by FMR method [92] (© IOP Publishing. Reproduced by permission of IOP Publishing. All rights reserved)

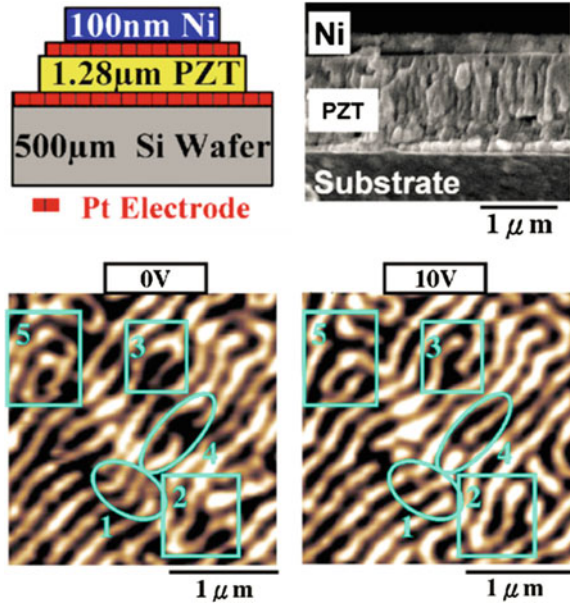
in which the residual strain or intermediate ferroelectric domain states are important for the ME effects. However, these works require precise controlling of the electric field to an appropriate value and electric-field control of magnetization exhibits obviously relaxation behavior, which are disadvantageous for applications. How to realize the electrical control of magnetization combining the advantages of nonvolatile behavior as the result in LSMO/BTO [76] and full reversibility as the result in LSMO/PMN-PT [77] at room temperature is an interesting and important issue, especially for realizing electric-writing and magnetic-reading random access memories.

Finally, it is worth to mention that the relevant researchers have employed ferromagnetic resonance (FMR) to investigate the electrical control of magnetic anisotropy in the compounded system [92, 93]. Combined with detailed theoretical analysis, the angle dependences of the magnetic properties under different electric fields were well understood, as shown in Fig. 1.30. On the other hand, researchers have also employed magnetic force microscopy (MFM) or Lorentz force microscopy (LFM) to observe the changes in the magnetic domains under in situ electric field [94, 95], which enable us to investigate ME coupling with spatial resolution and understand the mechanisms in the microscopic view, as shown in Fig. 1.31.

## 1.4 Application of Multiferroic Materials in Information Storage

So far, according to the all the progresses and the latest developments [96, 97] in multiferroic materials, the applications of multiferroicity and ME coupling effect in information storage technology can be divided into three kinds as follows: (i) Utilizing the coexistence of ferroelectric and magnetic orders in multiferroic materials to perform four or eight logic state in one memory unit. (ii) Utilizing the converse ME effect (i.e., electrical control of magnetism) to realize electrical writing and

**Fig. 1.31** Investigation of the electrical control of magnetic domains by MFM (Reprinted with permission from Ref. [94]. © 2008, American Institute of Physics)



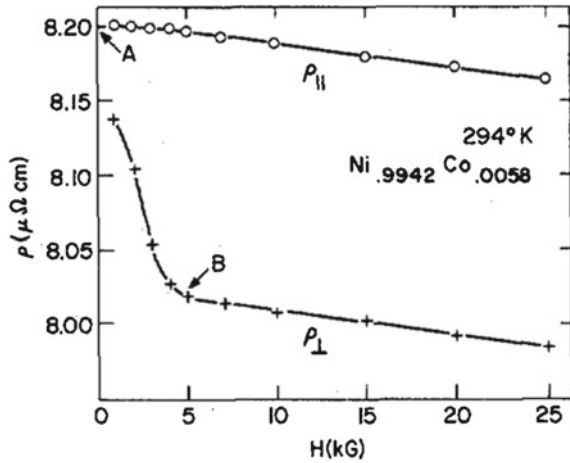
magnetic reading devices for the new generation memories. and (iii) Utilizing the positive ME effect (i.e., magnetic control of polarization) to realize passive read head in the form of directly reading out the magnetic information by voltage.

### 1.4.1 Magnetoresistance and its Classification

Magnetoresistance (MR) effect is a kind of phenomenon that the resistivity of the material changes with external magnetic field. Nearly all kinds of conductive material exhibit MR effect, for the conducting paths of the carriers are roundabout under magnetic field due to Lorentz force, resulting in the increasing of the resistance. This kind of MR effect is called the ordinary magnetoresistance (OMR), which has nothing to do with the electronic spin and the effect is generally small, unless the material has a strong anisotropic Fermi surface or a special geometry [98, 99]. While the MR effect is spin-related in the magnetic materials, which can be divided into different categories according to the mechanism. They are anisotropic magnetoresistance (AMR) effect, giant magnetoresistance (GMR) effect, tunneling magnetoresistance (TMR) effect, and colossal magnetoresistance (CMR) effect [100].

*The Anisotropic Magnetoresistance (AMR) effect* means that the resistivity of the magnetic materials will change with the angle between the directions of magnetic field and current, which was found by Thomson in the nickel-iron alloy in the year 1857 [101]. The AMR effect can be defined as  $AMR = (\rho_{\parallel} - \rho_{\perp})/\rho_0$ , in which  $\rho_0$  is the resistivity of the material without magnetic field or in an ideal demagnetization

**Fig. 1.32** The AMR effect in the nickel–iron alloy (© [1975] IEEE. Reprinted, with permission, from Ref. [102])



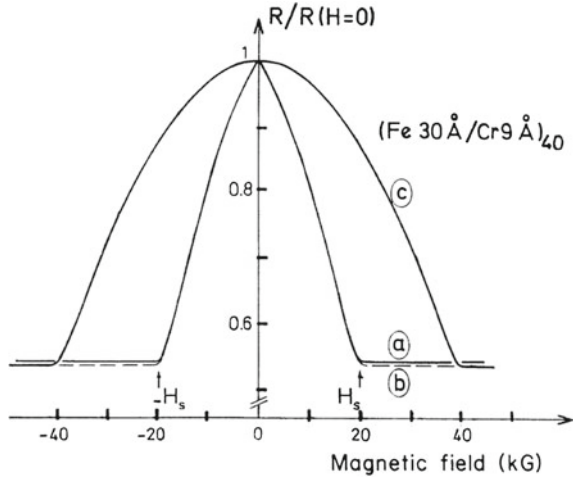
state,  $\rho_{||}$  is the resistivity of the material when the magnetic field is parallel to the current,  $\rho_{\perp}$  is the resistivity of the material when the magnetic field is perpendicular to the current [102], as shown in Fig. 1.32.

The AMR effect originates from the spin–orbit coupling of electrons and the anisotropic scattering by low symmetry potential centers in the process of electronic transportation. As a result, the ratio of the AMR effect strongly depends on the geometric size of the sample. When the thickness of the sample is comparable to the average free path of electrons, the superficial scattering of electrons is largest, resulting in maximum resistivity and minimum AMR effect. Investigation reveals that the nickel alloys exhibit large AMR effect with high sensitivity at room temperature, which was employed as the reading head in the magnetic recording in the year 1990, improving the storage density up to the magnitude of Gb/in<sup>2</sup>.

*The Giant Magnetoresistance (GMR)* was discovered by Baibich et al. in the ferromagnetic coupled Fe/Cr superlattice under 4.2 K and external magnetic field of 20 kOe in the year 1988 [103]. Since the MR effect was giant (up to 100 %) comparing to the AMR effect, this kind of MR effect was called GMR effect, as shown in Fig. 1.33.

The GMR effect originates from the scattering of electrons in spin-dependent transport between ferromagnetic/nonmagnetic metal/ferromagnetic multilayer structures [104]. When the directions of magnetization of the two FM layers are antiparallel, the spin-dependent scattering of electrons is maximum, resulting in the high resistance state. When the directions of magnetization of the two FM layers are parallel under large magnetic field, the spin-dependent scattering of electrons is minimum, resulting in the low resistance state. The measurement of GMR effect has to kinds of configurations, i.e., current in plane (CIP) and current perpendicular-to-plane (CPP), as shown in Fig. 1.34. Generally speaking, the GMR ratio is larger in the case of CPP than CIP, and the GMR ratio in the CPP configuration depends less critically on individual layer-thickness constraints. In another aspect, the GMR

**Fig. 1.33** The GMR effect in the Fe/Cr superlattice (Reprinted with permission from Ref. [103]. © 1988 by American Physical Society)



effect will be larger under lower temperature, for the background resistivity of the system will be smaller at lower temperature, resulting in higher MR ratio. The discovery of the GMR effect creating a new field named spintronics in physics, is significant for the electronic devices in magnetic recording. Soon after the discovery of the GMR effect, the relevant technics have been intensively studied and developed quickly. Due to the advantage of higher sensitivity, GMR replaces the AMR to become a new generation of magnetic reading head and occupies a pivotal position in the modern information storage technology. As a result, the two scientists Albert Fert and Peter Grünberg, who have discovered the GMR effect, were awarded the Nobel Prize in Physics in the year of 2007.

*The Tunneling magnetoresistance (TMR) effect* is a kind of MR effect in which the tunneling current is affected by the spin-dependent scattering of during the transportation. Being slightly different from the GMR effect, the multilayer structure in which the TMR effect happens consists of ferromagnetic metal/nonmagnetic insulator/ferromagnetic metal, which is also known as magnetic tunnel junctions (MTJs). When the directions of magnetizations are parallel with each other in both sides of the ferromagnetic electrodes, the electrons with majority spin are unlikely to be scattered while tunneling from one electrode to the other, resulting in a low-resistance state. When the directions of magnetizations are antiparallel with each other, the tunneling probability of electrons between the two ferromagnetic electrodes will be smaller due to the impact of the spin-dependent scattering, resulting in a high-resistance state. The TMR effect was discovered by Julliere in 1975 [105], in which a 14 % TMR ratio was observed in the structure of Fe/Ge/Co at 4.2 K and the relevant theory was also proposed as the following expression.

$$\text{TMR} = \frac{\Delta R}{R_P} = \frac{R_{AP} - R_P}{R_P} = \frac{2P_1P_2}{1 + P_1P_2} \quad (1.6)$$

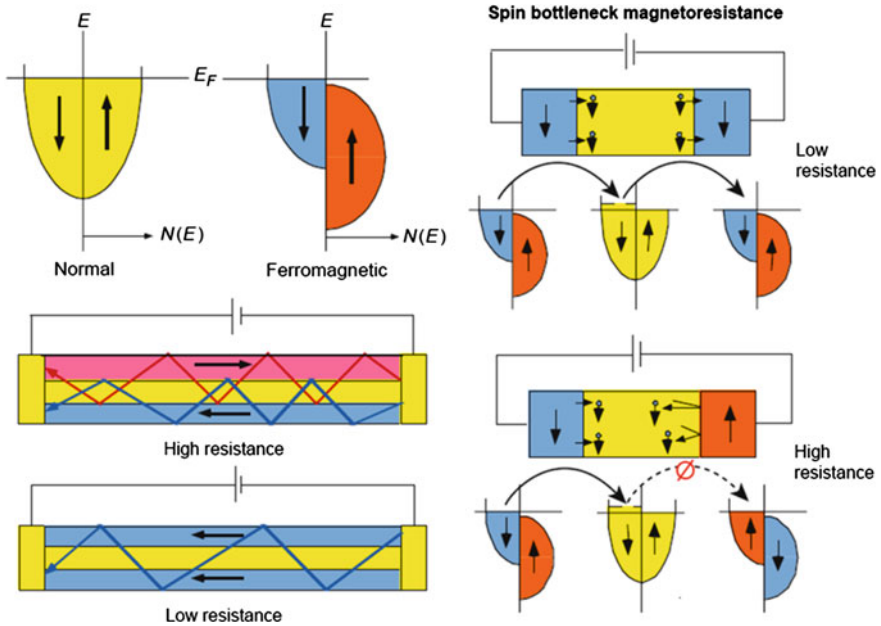


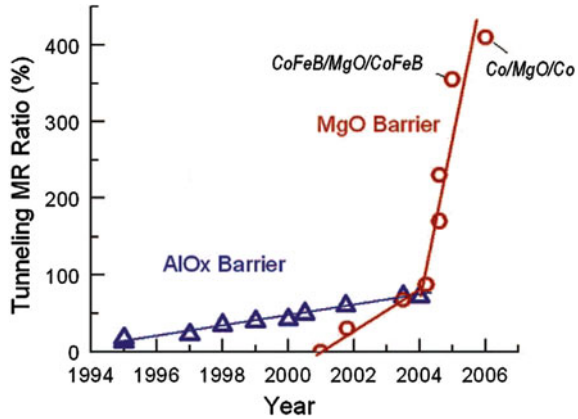
**Fig. 1.34** The GMR effect and the two measurement configurations: CIP (*left*) and CPP (*right*) (From Ref. [104]. Reprinted with permission from AAAS)

where  $R_P$  and  $R_{AP}$  are tunneling resistances of MTJ with the directions of magnetizations in the two magnetic electrodes aligned in parallel and anti-parallel, respectively, and  $P_1$  and  $P_2$  are the spin polarization ratios of the two ferromagnetic electrodes. With the continuous exploration of new materials, development of sample preparing and microprocessing techniques, the ratio of the TMR effect has been significantly improved in recent years (Fig. 1.35) and it has been reported to achieving 604 % at room temperature in the MTJ based on amorphous CoFeB alloy and MgO barrier [106]. Since the TMR effect has much higher sensitivity than the GMR effect in detecting the magnetic field, and the resistance of MTJ can be easily adjusted by changing the thickness of the barrier without affecting the ratio of the TMR effect, the MTJ is inevitably to be utilized as reading heads in the magnetic recording for the next generation and also the nonvolatile magnetic random access memory (MRAM) for the future applications [107].

### 1.4.2 Multiferroics and Magnetoelectric Multistate Memory

In the traditional information storage technology, a memory unit can only record two states “0” and “1” by switching the magnetization “UP” or “DOWN” (or the electronic states “ON” or “OFF”). However, there are both ferromagnetic order

**Fig. 1.35** The improvement of the TMR effect in the recent years (Reprinted from Ref. [107], © 2006, with permission from Elsevier)



with magnetization “UP” or “DOWN” and ferroelectric order with polarization “UP” or “DOWN” in the multiferroic materials, therefore four kinds of memory states ( $\pm P, \pm M$ ) can be used for information recording, which will greatly increase the storage capacity. A possible way to realize the four-state memory is employing the ferroelectric materials instead of the normal insulator in conventional MTJs as the barrier layer, to produce a kind of multiferroic tunnel junction (MFTJ) with the ferromagnetic/ferroelectric/ferromagnetic multilayer structure [108], as shown in Fig. 1.36.

The first experimental result of MFTJ was reported by Gajek et al. in the year of 2007 [109]. They have employed a 2 nm thick  $\text{La}_{0.1}\text{Bi}_{0.9}\text{MnO}_3$  (LBMO) film as the barrier layer in the MTJ to produce a kind of MFTJ with the structure of ferromagnetic oxide/multiferroic barrier/nonmagnetic metal. Utilizing the spin filter effect of the ferromagnetic order and the polarization switching of the ferroelectric order, they have achieved four-state tunneling resistance by changing the electric and magnetic fields, as shown in Fig. 1.37.

Subsequently, Garcia et al. reported another experimental work about the MFTJ in a structure of Fe/BTO/LSMO (ferromagnetic metal/ferroelectric barrier/ferromagnetic oxide) in the year 2010 [110], as shown in Fig. 1.38. According to the latest reports, Pantel et al. achieved a four-state tunneling resistance at 50 K in the structure of Co/PZT/LSMO [111], which is the highest temperature that the MFTJ can work so far. Unfortunately, all of these four-state tunneling resistance behaviors are realized at low temperatures, in which there is still a long way to go for room temperature applications. It is worth to mention that there is another work reported by Chien’s group in a perpendicularly magnetized CoFeB/MgO/CoFeB MTJ, in which the applying of electric field will reduce the coercive field of the CoFeB layer and result in a change of the TMR effect [112]. Although the MTJ structure in this report essentially does not belong to the MFTJ system, the so-called electric field controllable MTJ is first realized at room temperature in this work, which has an indubitable significance for applications.

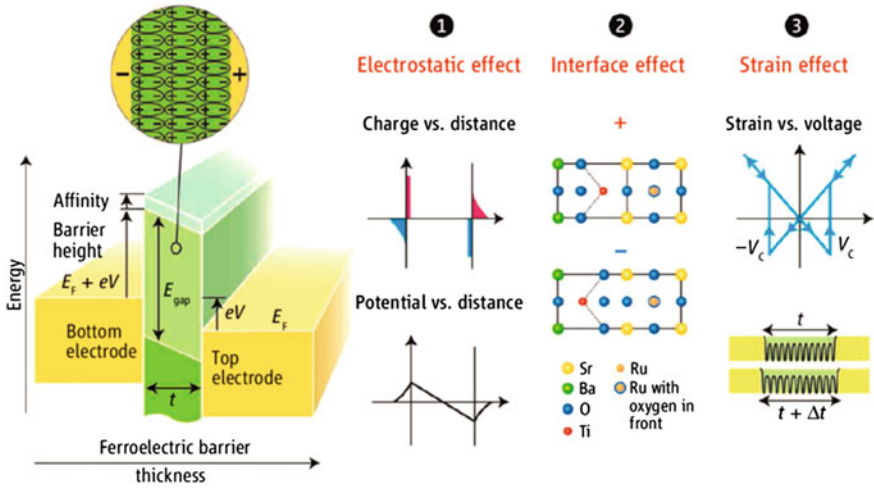


**Fig. 1.36** The ferroelectric barrier in a multiferroic tunnel junction (From Ref. [108]. Reprinted with permission from AAAS)

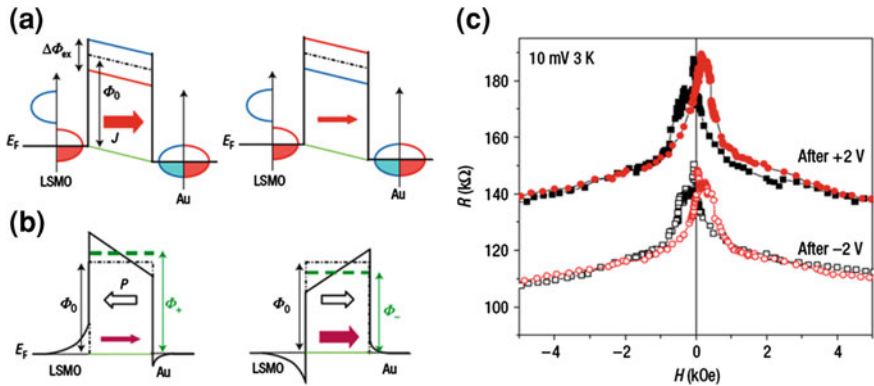


**Fig. 1.37** Sketch of the tunnel barrier potential profiles as well as tunnel currents for a multiferroic barrier due to the **a** exchange splitting and **b** ferroelectric polarization, and **c** the four-state tunneling resistance in LSMO/LBMO/Au structure (Reprinted by permission from Macmillan Publishers Ltd: Ref. [109], copyright 2007)

On the other hand, Shi et al. designed another kind of simple four-state memory prototype based on Co/PZT compound multiferroic structure [113], as shown in Fig. 1.39. This memory unit can be written into four logical states by the associated operation of DC electric field and magnetic field and read out the corresponding four states by means of detecting the response of the sample under AC electric stimulation with the lock-in amplifier technology. However, according to the symmetrical analysis, the states I and III (also II and IV) with both opposite

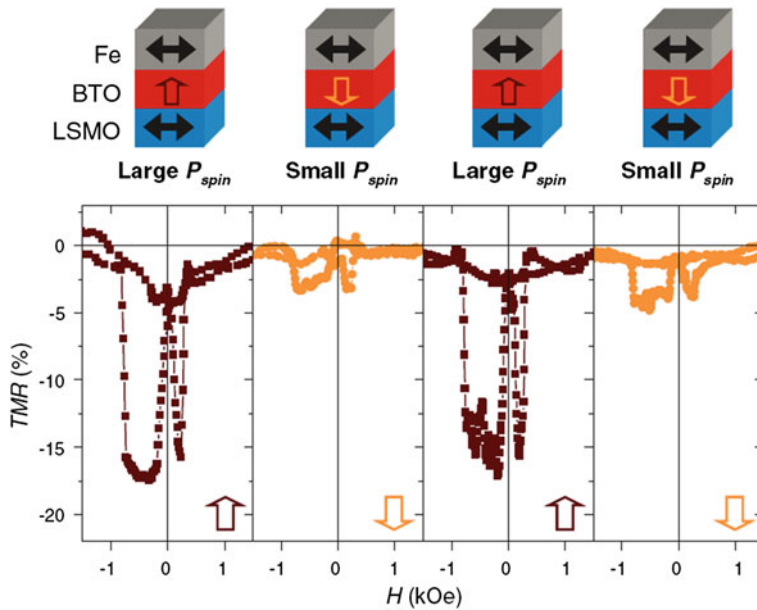
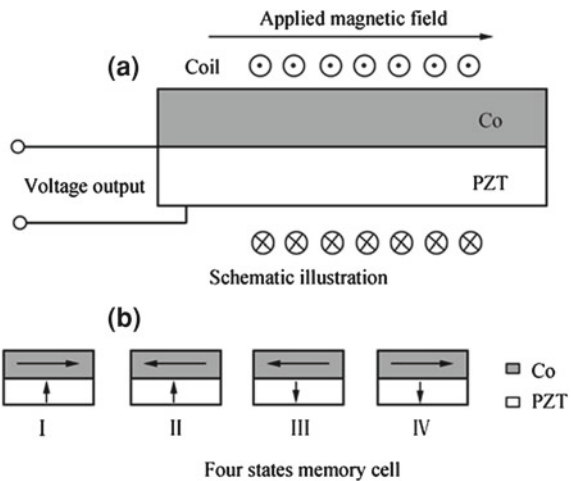


**Fig. 1.38** The four-state tunneling resistance in Fe/BTO/LSMO structure (From [110]. Reprinted with permission from AAAS)

**Fig. 1.39** The four-state memory based on the Co/PZT structure: **a** schematic illustration and **b** four-state memory cells (Reprinted from Ref. [113], with kind permission from Springer Science+Business Media)



magnetization directions and polarization directions will exhibit the same signal while reading out. As a result, a bias external magnetic field is needed to break the symmetry of the system and read out the four different states.

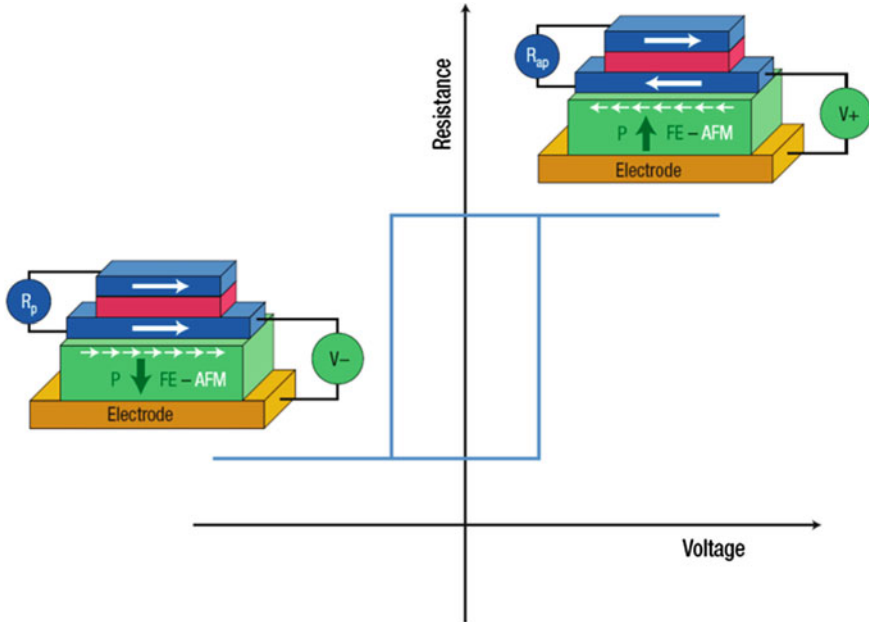


**Fig. 1.40** The electric-writing and magnetic-reading memory based on the multiferroic exchange bias effect (Reprinted by permission from Macmillan Publishers Ltd: Ref. [114], © 2008)

### 1.4.3 Multiferroic Structures and Electric-Writing and Magnetic-Reading Memory

One of the purposes of investigating the multiferroic materials and their ME coupling effects is to realize the electric-writing and magnetic-reading memory. Since the idea of using multiferroic materials for the new generation information storage device, a lot of new concept memories based on multiferroic materials have been proposed. In addition to the four-state memories based on MFTJs as discussed in the previous section, Bibes et al. has also put forward another way to realize the electric-writing and magnetic-reading random access memories (MERAMs) by directly fabricating the MTJ structure on top of the multiferroic layer [114], as shown in Fig. 1.40. In this MERAM, the information bit can be electrical writing mediated by the ME coupling between the ferroelectric order and antiferromagnetic order in the multiferroic substrate and the exchange bias (EB) coupling between the antiferromagnetic order and ferromagnetic order at the interface, resulting in the change of magnetization at the bottom layer. The data reading process can be easily realized by the TMR or GMR effect in the MTJ or spin valve structure.

Subsequently, Pertsev et al. [115] and Hu et al. [116, 117] also proposed a similar idea to realize the MERAMs by directly fabricating the MTJ structure on top of a ferroelectric or piezoelectric substrate as shown in Fig. 1.41, in which the

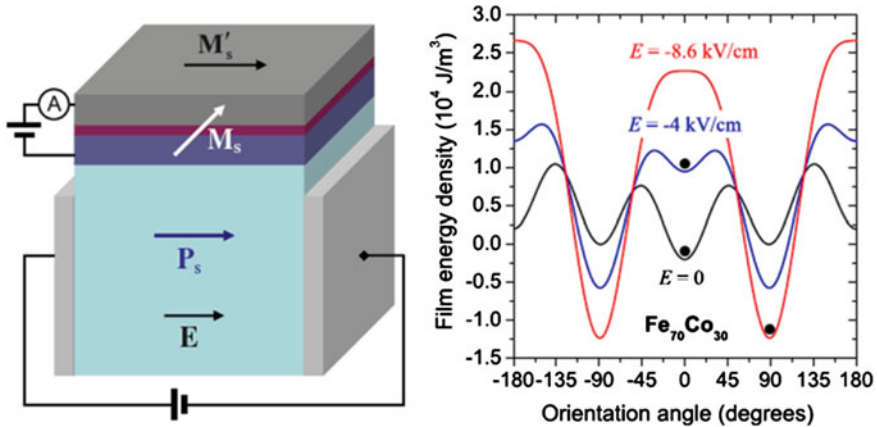


**Fig. 1.41** The MERAM structure (*left*) and theoretical simulation (*right*) based on the strain-mediated ME coupling (Reprinted with permission from Ref. [115]. © 2009, American Institute of Physics)

information can be written by the strain-mediated ME coupling between the FE substrate and the bottom ferromagnetic layer and read by the TMR or GMR effect. These creative designs and theoretical analysis are important and helpful for the experimental work.

In the experiment, the first electrical tunable MR device based on the multiferroic exchange bias effect was by Wu et al. in the year 2010 [118]. In which the magneto-resistance and coercive field of the LSMO film can be tuned at low temperature via the exchange bias coupling between the multiferroic  $\text{BiFeO}_3$  and ferromagnetic LSMO, as shown in Fig. 1.42. Later, Heron et al. reported an electrical tunable AMR effect in a  $\text{CoFe/BiFeO}_3$  structure at room temperature [119]. According to the latest report [120], Allibert et al. fabricated a spin valve structure on top of epitaxial  $\text{BiFeO}_3$  film and observed the electrical tunable GMR effect at room temperature, which is important for applications, as shown in Fig. 1.43.

In the experimental exploration of strain-mediated MERAMs, the first attempt has been made by Cavaco et al. in the year of 2007 [121] and another similar work was carried out by Liu et al. recently [122], as shown in Fig. 1.44. In this kind of strain-mediated memory, the strain induced by an external electric field via the converse piezoelectric effect of the substrate can be transmitted onto the ferromagnetic layer, which changes the magnetic anisotropy and the orientation of magnetization to realize the electrical modulation of the magnetoresistance.

It is worth to mention that there are also some interesting works in the design and exploration of the passive reading head in magnetic recording device based on multiferroic materials and ME coupling [123], as shown in Fig. 1.45. In this kind of multiferroic reading head, the stored information (i.e., magnetic signals) can be directly converted into voltage signals for output via the ME coupling, thereby eliminating the requirement of constant current source to read the magnetoresistance of spintronic devices and reducing the energy consumption.

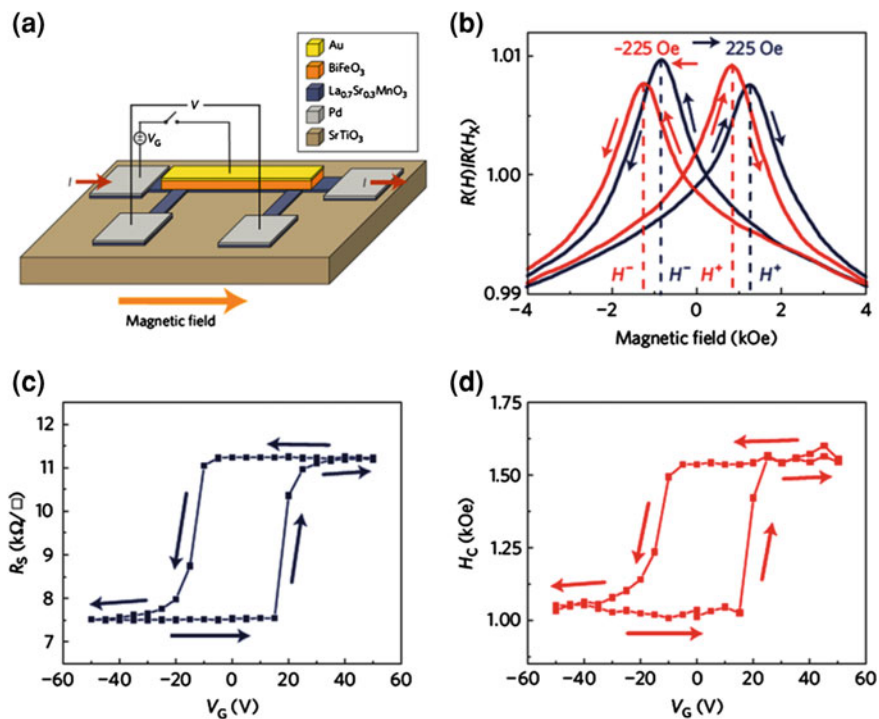


**Fig. 1.42** The electrical tunable MR device based on LSMO/BFO structure: **a** schematic of the BFO/LSMO field-effect device, **b** MR measurements after field cooling, **c** hysteresis of the channel resistance with respect to  $V_G$  at 5.5 K and **d** magnetic coercivity of the LSMO with respect to  $V_G$  at 5.5 K (Reprinted by permission from Macmillan Publishers Ltd: Ref. [118], © 2010)

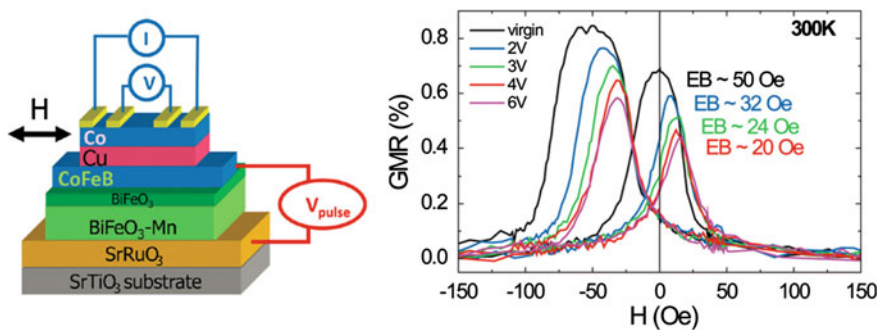


**Fig. 1.43** The electrical tunable GMR device based on EB effect (*left*) and the electric-field control of GMR effect (*right*) at room temperature (Reprinted with the permission from Ref. [120], © 2012 American Chemical Society)

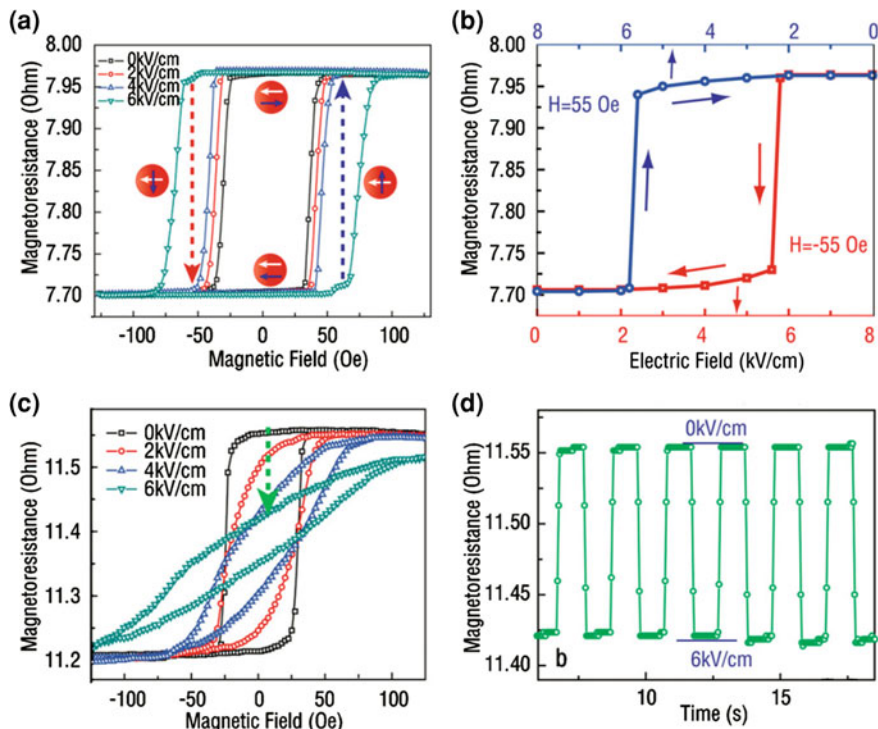


Fig. 1.44 The electrical control of GMR effect in the strain-mediated MERAMs along the a, b [100] direction and c, d [01-1] direction respectively (Reprinted with permission from Ref. [122]. © 2011, American Institute of Physics)

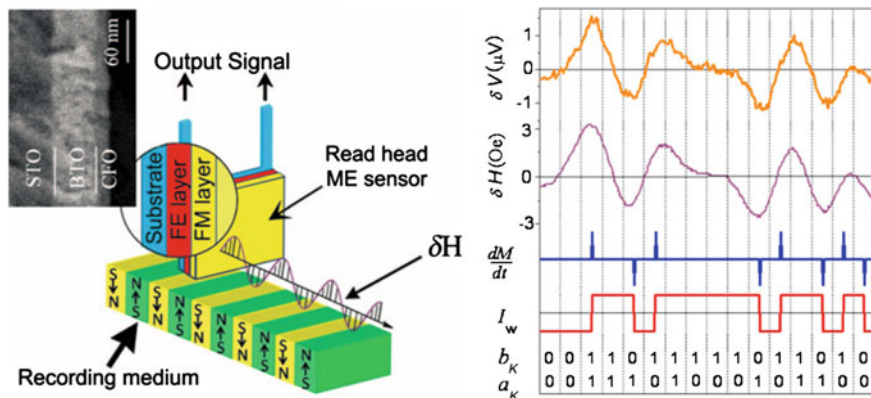


Fig. 1.45 The passive multiferroic reading head (left) and the experimental results (right) in the magnetic recording devices (Reprinted with permission from Ref. [123]. © 2008, American Institute of Physics)

## 1.5 General Topics and Brief Content of the Thesis

In summary, the investigation of multiferroic materials and ME coupling effect is a significant and challenging task. The ME coupling effect in multiferroic materials is not only interesting for scientific research, but also significant for applications. However, the single-phase multiferroic materials are rather rare at room temperature, and the ME coupling coefficients are also too small to be useful. As a result, the widespread FM/FE compound structures have become the main route in the multiferroic investigation, with relatively large ME coupling coefficients and better applied prospects. With the mission of realizing the electric-writing and magnetic-reading random access memory for the next generation, the investigation of electric-field control of magnetization in multiferroic materials or structures has become the key point and hot spot in the area of material science and condensed matter physics.

For the information storage technology, the convenient writing in and nonvolatile recording out are both important. Although a lot of work have demonstrate the convenient electric-writing in the FM/FE compound multiferroic structures at room temperature, in terms of electric-field control of magnetism. However, almost all of the magnetic responses to the electric stimulations exhibit “butterfly-like” behaviors, which is “volatile” and disadvantageous for applications. On the other hand, the main purpose of investigating the electrical control of magnetization is to realize the electric-writing and magnetic-reading memories. Although there are a lot of works reporting the progress in electric-writing, the works of combining electric-writing with magnetic-reading are still limited, and the practical electrical tunable RAMs base on the multiferroics is still under exploration.

Based on the above issues, the thesis mainly focuses on the investigation of electric-field control of magnetism and the spin-dependent transportation in the FM/FE compounded multiferroic heterostructure at room temperature, with the mission of realizing a reversible and nonvolatile electrical control of magnetization, and applying the ME coupling into the spin-dependend transport devices to realize the electric-writing and magnetic-reading random access memories at room temperature.

Regarding the selection of FM and FE materials for the compounded multiferroic heterostructure, the  $\text{Pb}(\text{Mg}_{1/3}\text{Nb}_{2/3})_{0.7}\text{Ti}_{0.3}\text{O}_3$  is a well-known ferroelectric relax or with the highest piezoelectric effect among the common ferroelectric/piezoelectric materials. Moreover, it also has rich domain structures and complicated FE phases, which may be utilized to realize the “nonvolatile” behavior in electrical control of magnetization. In another aspect, the ferromagnetic  $\text{Co}_{40}\text{Fe}_{40}\text{B}_{20}$  possesses the highest spin polarization among the amorphous Co–Fe–B alloys and has been demonstrated to achieve a very large TMR in magnetic tunnel junctions. What is more, different from the other crystalline or epitaxial materials, the amorphous CoFeB has no magneto-crystalline anisotropy, which may be interesting to investigate the ME coupling effect. In all, we choose the CoFeB/PMN-PT FM/FE compounded multiferroic heterostructures for the investigation of the electrical control of magnetization and magneto-resistance, with the two aspects as following.

First, the CoFeB/PMN-PT multiferroic heterostructure will be prepared by depositing 20 nm thick CoFeB film on top of the (001)-oriented PMN-PT single crystal in an ultra-high vacuum magnetron sputtering system. The electric-field control of magnetism of the sample will be investigated via magnetic measurement technologies with in situ electric fields. Utilizing the properties of non-magneto-crystalline anisotropy in CoFeB and the ferroelectric/ferroelastic domain in PMN-PT, it is possible to realize a kind of “nonvolatile” behavior in the electrical control of magnetization.

Second, another kind of CoFeB/PMN-PT multiferroic heterostructure will be prepared by depositing CoFeB film on top of the (011)-oriented PMN-PT single crystal in the ultra-high vacuum magnetron sputtering system. Since the (011)-oriented PMN-PT is reported to have a strong in-plane anisotropic piezostain with electric fields applied along the [011] crystalline direction, thereby it is expected to achieving large ME coupling effect in the CoFeB/PMN-PT(011) heterostructure. Moreover, a spin valve structure can also be prepared based on the FM/FE multiferroic structure. Utilizing the large in-plane strain anisotropy of (011)-cut PMN-PT substrate, it is possible to realize the electric-field control of GMR effect in this spintronic device and further achieve the electric-writing and magnetic-reading memory.

There are all together five chapters in this thesis: [Chap. 1](#) introduces the requirements and challenges of the current information storage technology, the phenomenon and concept of multiferroic materials and ME coupling effects, as well as some prospective work related to multiferroic materials or structures, which can be applied in information storage device. [Chapter 2](#) describes some experimental methods used in the investigation of electrical control of magnetization. [Chapters 3](#) and [4](#) are the works of realizing the nonvolatile electrical control of magnetization and electric field tunable GMR, respectively, [Chap. 5](#) which is also the last chapter of the thesis, is the summary and outlook.

## References

1. L. Zhang, Status and development trend for information storage technology. *Inf. Rec. Mater.* **5**, 47–54 (2006). (in Chinese)
2. W.W. Zhuang, W. Pan, B.D. Ulrich, et al., Novel colossal magnetoresistive thin film nonvolatile resistance random access memory (RRAM), in *International Electron Devices 2002 Meeting*, Technical Digest, pp. 193–196 (2002)
3. D.S. Dai, K.M. Qian, *Ferromagnetism (Volume 1)* (Science Press, Beijing, 1998). (in Chinese)
4. J.M.D. Coey, T. College, J.M.D. Dublin, *Magnetism and Magnetic Materials* (Cambridge University Press, UK, 2010)
5. D.E. Speliotis, Magnetic recording beyond the first 100 years. *J. Magn. Magn. Mater.* **193**, 29–35 (1999)
6. I. Zutic, J. Fabian, S. Das Sarma, Spintronics: fundamentals and applications. *Rev. Mod. Phys.* **76**, 323–410 (2004)

7. B. Ma, D.F. Shen, G.Q. Di, et al., Outlook of superhigh density magnetic recording. *J. Funct. Mater. Devices* **2**, 205–210 (2001) (in Chinese)
8. W.P. Sun, Recent developments in magnetic recording technology. *Inf. Rec. Mater.* **1**, 34–44 (2004). (in Chinese)
9. C. Chappert, A. Fert, F.N. Van Dau, The emergence of spin electronics in data storage. *Nat. Mater.* **6**, 813–823 (2007)
10. Z.L. Peng, X.F. Han, S.F. Zhao, et al., Perpendicular current-driven magnetization switching in free layer of magnetic tunneling junctions and MRAM. *Acta Physica Sinica* **2**, 860–864 (2006) (in Chinese)
11. X.W. Wu, Z.Z. Guo, The principle and research development of magnetoresistive random access memory. *Rec. Media* **2**, 52–57 (2009). (in Chinese)
12. W.L. Zhong, *Ferroelectrics* (Science Press, Beijing, 1996). (in Chinese)
13. M. Dawber, K.M. Rabe, J.F. Scott, Physics of thin-film ferroelectric oxides. *Rev. Mod. Phys.* **77**, 1083–1130 (2005)
14. J.F. Scott, *Ferroelectric Memories* (Springer-Verlag, Berlin, 2000)
15. J.S. Liu, S.R. Zhang, Y.R. Li, Ferroelectrics memories technology. *Phys. Eng.* **2**, 37–40 (2002). (in Chinese)
16. X.J. Hong, C.F. Yu, H.H. Yu et al., The design and testing of a ferroelectric memory cell. *Res. Prog. SSE* **1**, 45–53 (1999). (in Chinese)
17. L. Ma, The work principle and device structure of FeRAM. *Electron. Packaging* **8**, 35–38 (2008). (in Chinese)
18. H. Schmid, Multi-ferroic magnetolectrics. *Ferroelectrics* **162**, 317–338 (1994)
19. H. Schmid, Some symmetry aspects of ferroics and single phase multiferroics. *J. Phys. Condens. Matter* **20**, 434201 (2008)
20. N.A. Spaldin, M. Fiebig, The renaissance of magnetolectric multiferroics. *Science* **309**, 391–392 (2005)
21. Y. Tokura, Multiferroics—toward strong coupling between magnetization and polarization in a solid. *J. Magn. Magn. Mater.* **310**, 1145–1150 (2007)
22. K.F. Wang, J.M. Liu, Z.F. Ren, Multiferroicity: the coupling between magnetic and polarization orders. *Adv. Phys.* **58**, 321–448 (2009)
23. N.A. Spaldin, S.W. Cheong, R. Ramesh, Multiferroics: past, present, and future. *Phys. Today* **63**, 38–43 (2010)
24. W. Eerenstein, N.D. Mathur, J.F. Scott, Multiferroic and magnetoelectric materials. *Nature* **442**, 759–765 (2006)
25. R. Ramesh, N.A. Spaldin, Multiferroics: progress and prospects in thin films. *Nat. Mater.* **6**, 21–29 (2007)
26. E. Ascher, H. Rieder, H. Schmid et al., Some properties of ferromagnetolectric nickel-iodine boracite  $\text{Ni}_3\text{B}_7\text{O}_{13}\text{I}$ . *J. Appl. Phys.* **37**, 1404 (1966)
27. J.F. Scott, Mechanisms of dielectric anomalies in  $\text{BaMnF}_4$ . *Phys. Rev. B* **16**, 2329–2331 (1977)
28. T. Watanabe, K. Kohn, Magnetolectric effect and low-temperature transition of  $\text{PbFe}_{0.5}\text{Nb}_{0.5}\text{O}_3$  single-crystal. *Phase Transitions* **15**, 57–68 (1989)
29. N.A. Hill, Why are there so few magnetic ferroelectrics? *J. Phys. Chem. B* **104**, 6694–6709 (2000)
30. M. Fiebig, Revival of the magnetoelectric effect. *J. Phys. D-Appl. Phys.* **38**, R123–R152 (2005)
31. W. Prellier, M.P. Singh, P. Murugavel, The single-phase multiferroic oxides: from bulk to thin film. *J. Phys. Condens. Matter* **17**, R803–R832 (2005)
32. Z.H. Chi, C.Q. Jin, Recent advances in single-phase magnetoelectric multiferroic (ferroelectromagnet). *Prog. Phys.* **2**, 225–238 (2007). (in Chinese)
33. K.F. Wang, J.M. Liu, Y. Wang, Single-phase multiferroics—the coupling between magnetic and polarization orders. *Chin. Sci. Bull.* **53**, 1098–1135 (2008). (in Chinese)
34. T. Kimura, S. Kawamoto, I. Yamada et al., Magnetocapacitance effect in multiferroic  $\text{BiMnO}_3$ . *Phys. Rev. B* **67**, 180401 (2003)

35. T. Zhao, A. Scholl, F. Zavaliche et al., Electrical control of antiferromagnetic domains in multiferroic BiFeO<sub>3</sub> films at room temperature. *Nat. Mater.* **5**, 823–829 (2006)
36. S.H. Baek, H.W. Jang, C.M. Folkman et al., Ferroelastic switching for nanoscale non-volatile magnetoelectric devices. *Nat. Mater.* **9**, 309–314 (2010)
37. C. Ederer, N.A. Spaldin, Weak ferromagnetism and magnetoelectric coupling in bismuth ferrite. *Phys. Rev. B* **71**, 060401 (2005)
38. R.J. Zeches, M.D. Rossell, J.X. Zhang et al., A strain-driven morphotropic phase boundary in BiFeO<sub>3</sub>. *Science* **326**, 977–980 (2009)
39. T. Choi, S. Lee, Y.J. Choi et al., Switchable ferroelectric diode and photovoltaic effect in BiFeO<sub>3</sub>. *Science* **324**, 63–66 (2009)
40. T. Lottermoser, T. Lonkai, U. Amann et al., Magnetic phase control by an electric field. *Nature* **430**, 541–544 (2004)
41. T. Choi, Y. Horibe, H.T. Yi et al., Insulating interlocked ferroelectric and structural antiphase domain walls in multiferroic YMnO<sub>3</sub>. *Nat. Mater.* **9**, 253–258 (2010)
42. T. Kimura, T. Goto, H. Shintani et al., Magnetic control of ferroelectric polarization. *Nature* **426**, 55–58 (2003)
43. N. Hur, S. Park, P.A. Sharma et al., Electric polarization reversal and memory in a multiferroic material induced by magnetic fields. *Nature* **429**, 392–395 (2004)
44. Y. Tokura, S. Seki, Multiferroics with spiral spin orders. *Adv. Mater.* **22**, 1554–1565 (2010)
45. S.W. Cheong, M. Mostovoy, Multiferroics: a magnetic twist for ferroelectricity. *Nat. Mater.* **6**, 13–20 (2007)
46. W.F. Brown Jr, R.M. Hornreich, S. Shtrikman, Upper bound on the magnetoelectric susceptibility. *Phys. Rev.* **168**, 574 (1968)
47. C.W. Nan, M.I. Bichurin, S.X. Dong et al., Multiferroic magnetoelectric composites: historical perspective, status, and future directions. *J. Appl. Phys.* **103**, 031101 (2008)
48. L. Martin, S.P. Crane, Y.H. Chu et al., Multiferroics and magnetoelectrics: thin films and nanostructures. *J. Phys. Condens. Matter* **20**, 434220 (2008)
49. J.P. Velev, S.S. Jaswal, E.Y. Tsymbal, Multi-ferroic and magnetoelectric materials and interfaces. *Philos. Trans. R. Soc. A Math. Phys. Eng. Sci.* **369**, 3069–3097 (2011)
50. J. Ma, J.M. Hu, Z. Li et al., Recent progress in multiferroic magnetoelectric composites: from bulk to thin films. *Adv. Mater.* **23**, 1062–1087 (2011)
51. H.C. He, Y.H. Lin, C.W. Nan, Ferromagnetic and ferroelectric compound multiferroic thin films. *Chin. Sci. Bull.* **10**, 1136–1148 (2008). (in Chinese)
52. J.G. Wan, X.W. Wang, Y.J. Wu et al., Magnetoelectric CoFe<sub>2</sub>O<sub>4</sub>-Pb(Zr, Ti)O<sub>3</sub> composite thin films derived by a sol–gel process. *Appl. Phys. Lett.* **86**, 122501 (2005)
53. H. Ryu, P. Murugavel, J.H. Lee et al., Magnetoelectric effects of nanoparticulate Pb(Zr<sub>0.52</sub>Ti<sub>0.48</sub>)O<sub>3</sub>-NiFe<sub>2</sub>O<sub>4</sub> composite films. *Appl. Phys. Lett.* **89**, 102907 (2006)
54. H. Zheng, J. Wang, S.E. Lofland et al., Multiferroic BaTiO<sub>3</sub>-CoFe<sub>2</sub>O<sub>4</sub> nanostructures. *Science* **303**, 661–663 (2004)
55. F. Zavaliche, H. Zheng, L. Mohaddes-Ardabili et al., Electric field-induced magnetization switching in epitaxial columnar nanostructures. *Nano Lett.* **5**, 1793–1796 (2005)
56. H.C. He, J. Wang, B.P. Zhou et al., Ferroelectric and ferromagnetic behavior of Pb(Zr<sub>0.52</sub>Ti<sub>0.48</sub>)O<sub>3</sub>-Co<sub>0.9</sub>Zn<sub>0.1</sub>Fe<sub>2</sub>O<sub>4</sub> multilayered thin films prepared via solution processing. *Adv. Funct. Mater.* **17**, 1333–1338 (2007)
57. P. Murugavel, P. Padhan, W. Prellier, Enhanced magnetoresistance in ferromagnetic Pr<sub>0.85</sub>Ca<sub>0.15</sub>MnO<sub>3</sub>/ferroelectric Ba<sub>0.6</sub>Sr<sub>0.4</sub>TiO<sub>3</sub> superlattice films. *Appl. Phys. Lett.* **85**, 4992–4994 (2004)
58. M.P. Singh, W. Prellier, C. Simon et al., Magnetocapacitance effect in perovskite-superlattice based multiferroics. *Appl. Phys. Lett.* **87**, 022505 (2005)
59. C.Y. Deng, Y. Zhang, J. Ma et al., Magnetic-electric properties of epitaxial multiferroic NiFe<sub>2</sub>O<sub>4</sub>-BaTiO<sub>3</sub> heterostructure. *J. Appl. Phys.* **102**, 074114 (2007)
60. M. Al Ahmad, R. Coccetti, R. Plana, The effect of substrate clamping on piezoelectric thin-film parameters, in *2007 Asia Pacific Microwave Conference*, vols 1–5, New York, IEEE, pp. 946–949 (2007)

61. C.W. Nan, G. Liu, Y.H. Lin et al., Magnetic-field-induced electric polarization in multiferroic nanostructures. *Phys. Rev. Lett.* **94**, 197203 (2005)
62. J.X. Zhang, Y.L. Li, D.G. Schlom et al., Phase-field model for epitaxial ferroelectric and magnetic nanocomposite thin films. *Appl. Phys. Lett.* **90**, 052909 (2007)
63. C.G. Duan, Progress in the study of magnetoelectric effect. *Prog. Phys.* **3**, 215–238 (2009). (in Chinese)
64. Y. Wang, J.M. Hu, Y.H. Lin et al., Multiferroic magnetoelectric composite nanostructures. *NPG Asia Mater.* **2**, 61–68 (2010)
65. J. Nogues, I.K. Schuller, Exchange bias. *J. Magn. Magn. Mater.* **192**, 203–232 (1999)
66. Y.H. Chu, L.W. Martin, M.B. Holcomb et al., Electric-field control of local ferromagnetism using a magnetoelectric multiferroic. *Nat. Mater.* **7**, 478 (2008)
67. M. Kiwi, Exchange bias theory. *J. Magn. Magn. Mater.* **234**, 584–595 (2001)
68. V. Laukhin, V. Skumryev, X. Marti et al., Electric-field control of exchange bias in multiferroic epitaxial heterostructures. *Phys. Rev. Lett.* **97**, 227201 (2006)
69. H. Molegraaf, J. Hoffman, C. Vaz et al., Magnetoelectric effects in complex oxides with competing ground states. *Adv. Mater.* **21**, 3470 (2009)
70. D. Chiba, M. Sawicki, Y. Nishitani et al., Magnetization vector manipulation by electric fields. *Nature* **455**, 515–518 (2008)
71. C. Bihler, M. Althammer, A. Brandlmaier et al.,  $\text{Ga}_{(1-x)}\text{Mn}_{(x)}\text{As}$ /piezoelectric actuator hybrids: a model system for magnetoelastic magnetization manipulation. *Phys. Rev. B* **78**, 045203 (2008)
72. T. Maruyama, Y. Shiota, T. Nozaki et al., Large voltage-induced magnetic anisotropy change in a few atomic layers of iron. *Nat. Nanotechnol.* **4**, 158–161 (2009)
73. C.G. Duan, S.S. Jaswal, E.Y. Tsymlal, Predicted magnetoelectric effect in  $\text{Fe}/\text{BaTiO}_3$  multilayers: ferroelectric control of magnetism. *Phys. Rev. Lett.* **97**, 047201 (2006)
74. C.G. Duan, J.P. Velev, R.F. Sabirianov et al., Surface magnetoelectric effect in ferromagnetic metal films. *Phys. Rev. Lett.* **101**, 137201 (2008)
75. C.W. Nan, Magnetoelectric effect in composites of piezoelectric and piezomagnetic phases. *Phys. Rev. B* **50**, 6082–6088 (1994)
76. W. Eerenstein, M. Wiora, J.L. Prieto et al., Giant sharp and persistent converse magnetoelectric effects in multiferroic epitaxial heterostructures. *Nat. Mater.* **6**, 348–351 (2007)
77. C. Thiele, K. Dorr, O. Bilani, et al., Influence of strain on the magnetization and magnetoelectric effect in  $\text{La}_{0.7}\text{A}_{0.3}\text{MnO}_3/\text{PMN-PT}(001)$  ( $A = \text{Sr}, \text{Ca}$ ). *Phys. Rev. B* **75**, 054408 (2007)
78. S. Sahoo, S. Polisetty, C.G. Duan et al., Ferroelectric control of magnetism in  $\text{BaTiO}_3/\text{Fe}$  heterostructures via interface strain coupling. *Phys. Rev. B* **76**, 092108 (2007)
79. S. Brivio, D. Petti, R. Bertacco et al., Electric-field control of magnetic anisotropies and magnetic coercivity in  $\text{Fe}/\text{BaTiO}_3(001)$  heterostructures. *Appl. Phys. Lett.* **98**, 92505 (2011)
80. Y.J. Chen, J.S. Gao, T. Fitchorov et al., Large converse magnetoelectric coupling in  $\text{FeCoV}/\text{lead zinc niobate-lead titanate}$  heterostructure. *Appl. Phys. Lett.* **94**, 082504 (2009)
81. J.J. Yang, Y.G. Zhao, H.F. Tian et al., Electric field manipulation of magnetization at room temperature in multiferroic  $\text{CoFe}_2\text{O}_4/\text{Pb}(\text{Mg}_{1/3}\text{Nb}_{2/3})_{0.7}\text{Ti}_{0.3}\text{O}_3$  heterostructures. *Appl. Phys. Lett.* **94**, 212504 (2009)
82. J. Lou, M. Liu, D. Reed et al., Giant electric field tuning of magnetism in novel multiferroic  $\text{FeGaB}/\text{lead zinc niobate-lead titanate}$  (PZN-PT) heterostructures. *Adv. Mater.* **21**, 4711 (2009)
83. M. Liu, O. Obi, J. Lou et al., Giant electric field tuning of magnetic properties in multiferroic ferrite/ferroelectric heterostructures. *Adv. Funct. Mater.* **19**, 1826–1831 (2009)
84. M. Liu, O. Obi, J. Lou et al., Strong magnetoelectric coupling in ferrite/ferroelectric multiferroic heterostructures derived by low temperature spin-spray deposition. *J. Phys. D-Appl. Phys.* **42**, 045007 (2009)

85. J. Ma, Y.H. Lin, C.W. Nan, Anomalous electric field-induced switching of local magnetization vector in a simple FeBSiC-on-Pb(Zr, Ti)O<sub>3</sub> multiferroic bilayer. *J. Phys. D-Appl. Phys.* **43**, 012001 (2010)
86. S. Geprags, A. Brandlmaier, M. Opel et al., Electric field controlled manipulation of the magnetization in Ni/BaTiO<sub>3</sub> hybrid structures. *Appl. Phys. Lett.* **96**, 142509 (2010)
87. J. Wang, J. Ma, Z. Li et al., Switchable voltage control of the magnetic coercive field via magnetoelectric effect. *J. Appl. Phys.* **110**, 043919 (2011)
88. H.C. Xuan, L.Y. Wang, Y.X. Zheng et al., Electric-field control of magnetism without magnetic bias field in the Ni/Pb(Mg<sub>1/3</sub>Nb<sub>2/3</sub>)O<sub>3</sub>-PbTiO<sub>3</sub>/Ni composite. *Appl. Phys. Lett.* **99**, 032509 (2011)
89. J.M. Hu, C.W. Nan, Electric-field-induced magnetic easy-axis reorientation in ferromagnetic/ferroelectric layered heterostructures. *Phys. Rev. B* **80**, 224416 (2009)
90. J.M. Hu, C.W. Nan, L.Q. Chen, Size-dependent electric voltage controlled magnetic anisotropy in multiferroic heterostructures: interface-charge and strain mediated magnetoelectric coupling. *Phys. Rev. B* **83**, 134408 (2011)
91. T. Wu, A. Bur, P. Zhao et al., Giant electric-field-induced reversible and permanent magnetization reorientation on magnetoelectric Ni/(011)[Pb(Mg<sub>1/3</sub>Nb<sub>2/3</sub>)O<sub>3</sub>]<sub>(1-x)</sub>-[PbTiO<sub>3</sub>]<sub>x</sub> heterostructure. *Appl. Phys. Lett.* **98**, 012504 (2011)
92. M. Weiler, A. Brandlmaier, S. Geprags et al., Voltage controlled inversion of magnetic anisotropy in a ferromagnetic thin film at room temperature. *New J. Phys.* **11**, 01302 (2009)
93. M. Liu, O. Obi, Z.H. Cai et al., Electrical tuning of magnetism in Fe<sub>3</sub>O<sub>4</sub>/PZN-PT multiferroic heterostructures derived by reactive magnetron sputtering. *J. Appl. Phys.* **107**, 073916 (2010)
94. T.K. Chung, G.P. Carman, K.P. Mohanchandra, Reversible magnetic domain-wall motion under an electric field in a magnetoelectric thin film. *Appl. Phys. Lett.* **92**, 112509 (2008)
95. T. Brintlinger, S.H. Lim, K.H. Baloch et al., In situ observation of reversible nanomagnetic switching induced by electric fields. *Nano Lett.* **10**(4), 1219–1223 (2010)
96. L.W. Martin, Y.H. Chu, R. Ramesh, Advances in the growth and characterization of magnetic, ferroelectric, and multiferroic oxide thin films. *Mater. Sci. Eng. R Rep.* **68**, 133 (2010)
97. K. Shi, H.C. He, N. Wang, Recent progress in application of multiferroic magnetoelectric materials on storage technology. *J. Chin. Ceram. Soc.* **11**, 1792–1799 (2011). (in Chinese)
98. F.Y. Yang, K. Liu, K.M. Hong et al., Large magnetoresistance of electrodeposited single-crystal bismuth thin films. *Science* **284**, 1335–1337 (1999)
99. S.A. Solin, T. Thio, D.R. Hines et al., Enhanced room-temperature geometric magnetoresistance in inhomogeneous narrow-gap semiconductors. *Science* **289**, 1530–1532 (2000)
100. S. Jin, T.H. Tiefel, M. McCormack et al., Thousandfold change in resistivity in magnetoresistive La–Ca–Mn–O films. *Science* **264**, 413–415 (1994)
101. W. Thomson, On the electro-dynamic qualities of metals: effects of magnetization on the electric conductivity of nickel and of iron. *Proc. R. Soc.* **8**, 546–550 (1857)
102. T.R. McGuire, R.I. Potter, Anisotropic magnetoresistance in ferromagnetic 3d alloys. *IEEE Trans. Magn.* **11**, 1018–1038 (1975)
103. M.N. Baibich, J.M. Broto, A. Fert et al., Giant magnetoresistance of (001)Fe/(001) Cr magnetic superlattices. *Phys. Rev. Lett.* **61**, 2472–2475 (1988)
104. G.A. Prinz, Magnetoelectronics. *Science* **282**, 1660–1663 (1998)
105. M. Julliere, Tunneling between ferromagnetic films. *Phys. Lett. A* **54**, 225–226 (1975)
106. S. Ikeda, J. Hayakawa, Y. Ashizawa et al., Tunnel magnetoresistance of 604 % at 300 K by suppression of Ta diffusion in CoFeB/MgO/CoFeB pseudo-spin-valves annealed at high temperature. *Appl. Phys. Lett.* **93**, 082508 (2008)
107. J. Zhu, C.D. Park, Magnetic tunnel junctions. *Mater. Today* **9**, 36–45 (2006)
108. E.Y. Tsymbal, H. Kohlstedt, Tunneling across a ferroelectric. *Science* **313**, 181–183 (2006)
109. M. Gajek, M. Bibes, S. Fusil et al., Tunnel junctions with multiferroic barriers. *Nat. Mater.* **6**, 296–302 (2007)

110. V. Garcia, M. Bibes, L. Bocher et al., Ferroelectric control of spin polarization. *Science* **327**, 1106–1110 (2010)
111. D. Pantel, S. Goetze, D. Hesse et al., Reversible electrical switching of spin polarization in multiferroic tunnel junctions. *Nat. Mater.* **11**, 289–293 (2012)
112. W.G. Wang, M.G. Li, S. Hageman et al., Electric-field-assisted switching in magnetic tunnel junctions. *Nat. Mater.* **11**, 64–68 (2012)
113. Z. Shi, C.P. Wang, X.J. Liu et al., A four-state memory cell based on magnetoelectric composite. *Chin. Sci. Bull.* **53**(14), 2135–2138 (2008)
114. M. Bibes, A. Barthelemy, Multiferroics: towards a magnetoelectric memory. *Nat. Mater.* **7**, 425–426 (2008)
115. N.A. Pertsev, H. Kohlstedt, Magnetic tunnel junction on a ferroelectric substrate. *Appl. Phys. Lett.* **95**, 163503 (2009)
116. J.M. Hu, Z. Li, J. Wang et al., Electric-field control of strain-mediated magnetoelectric random access memory. *J. Appl. Phys.* **107**, 093912 (2010)
117. J.M. Hu, Z. Li, L.Q. Chen et al., High-density magnetoresistive random access memory operating at ultralow voltage at room temperature. *Nat. Commun.* **2**, 553 (2011)
118. S.M. Wu, S.A. Cybart, P. Yu et al., Reversible electric control of exchange bias in a multiferroic field-effect device. *Nat. Mater.* **9**, 756–761 (2010)
119. J.T. Heron, M. Trassin, K. Ashraf et al., Electric-field-induced magnetization reversal in a ferromagnet-multiferroic heterostructure. *Phys. Rev. Lett.* **107**, 217202 (2011)
120. J. Allibe, S. Fusil, K. Bouzheouane et al., Room temperature electrical manipulation of giant magnetoresistance in spin valves exchange-biased with BiFeO<sub>3</sub>. *Nano Lett.* **12**, 1141–1145 (2012)
121. C. Cavaco, M. van Kampen, L. Lagae et al., A room-temperature electrical field-controlled magnetic memory cell. *J. Mater. Res.* **22**, 2111–2115 (2007)
122. M. Liu, S.D. Li, O. Obi et al., Electric field modulation of magnetoresistance in multiferroic heterostructures for ultralow power electronics. *Appl. Phys. Lett.* **98**, 222509 (2011)
123. Y. Zhang, Z. Li, C.Y. Deng et al., Demonstration of magnetoelectric read head of multiferroic heterostructures. *Appl. Phys. Lett.* **92**, 152510 (2008)

# Chapter 2

## Experimental Methods

This chapter will introduce the relevant technologies and experimental methods employed for the work of the thesis. It mainly includes the sample preparation techniques: pulsed laser deposition (PLD) and magnetron sputtering; the sample measurement and characterization techniques: (i) the experimental methods used to characterize the macroscopic magnetic properties of the samples, including the superconducting quantum interference device (SQUID), electron spin resonance (ESR), magneto-optical Kerr effect (MOKE) techniques; (ii) the experimental methods used to characterize the macroscopic ferroelectric and piezoelectric properties of the samples, including ferroelectric hysteresis loops and strain curves measurement techniques; (iii) the experimental methods used to characterize the microscopic magnetic and ferroelectric properties, including scanning probe microscopy (SPM), X-ray diffraction (XRD), and transmission electron microscopy (TEM) techniques; and the electric transport measurement techniques used for the investigation of electric field tunable spintronic devices.

### 2.1 Sample Preparation Techniques

#### 2.1.1 Pulsed Laser Deposition Method

With the development of laser technology and the relevant applications, a new kind of thin film preparation technology which employs laser as the heat source, i.e., pulsed laser deposition, was first attempted by Smith et al. Later it was developed by Vankatesan et al. in Bell Laboratories of the USA [1] and was widely used in the preparation of high-temperature superconducting, ferroelectric materials, and magnetic oxides.

The principle and basic configuration of the pulsed laser deposition [2, 3] is shown in Fig. 2.1. When a high-energy pulsed laser beam emitted by a laser generator passes through a series of optical system and is finally focused on the target inside a chamber, the temperature of the target surface is instantaneously heated up

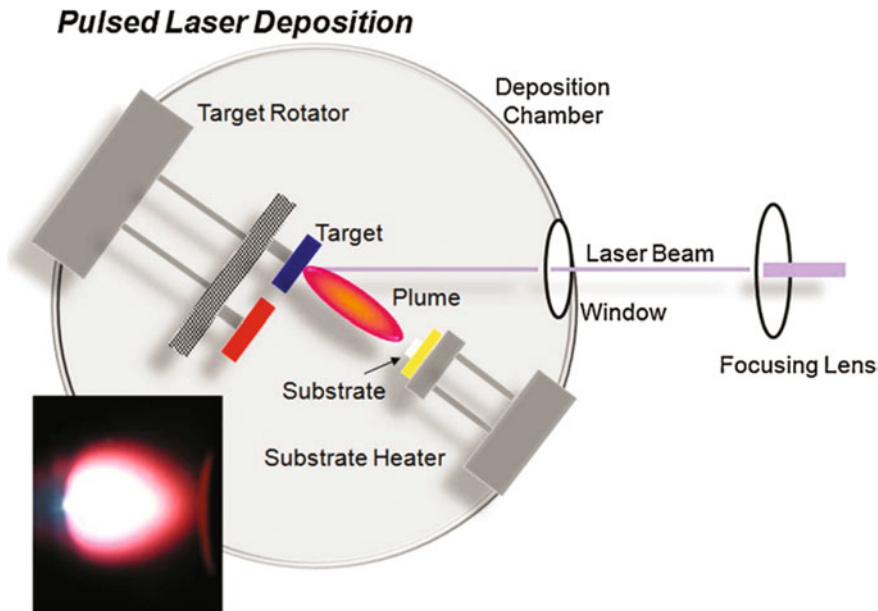


**Fig. 2.1** Schematic diagram of the PLD technology (Reprinted from Ref. [3], Copyright 2010, with permission from Elsevier)

to 2000–3000 K by the high-energy density released from the focused laser beam. Due to the high temperature, the materials inside the target are instantaneously vaporized and ionized, forming complex plasma containing atoms, molecules, ions, and neutral particles. With the continuous absorption of laser energy and further ionization of the materials in the target, the temperature and pressure inside the plasma increase rapidly. As a result, the plasma is ejected perpendicular to the target surface due to the ultra-high-pressure gradient and forms a plume (plasma plume). In the diffusion process of the plasma plume, the interaction between the plasma and the atmosphere inside the chamber will continuously increase the ionization process and the collisions between the components of the plasma, which is finally sprayed onto a substrate placed on a heater. By optimizing the factors such as laser density, pressure of the atmosphere, and heating temperature, epitaxial thin films can be prepared with a right copy of material composition of the targets.

Preparing thin films based on the kinetic and thermodynamic process, the PLD technology has the following characteristics. The advantages are (i) Good component reproduction: Since the majority of the target surface can be ionized into plasma under the heating of the high-energy laser shot, the composition of the film has a high consistency with the target components, which is advantageous for the preparation of the polyhydric compound thin film. (ii) High preparing efficiency and target utilization: Since the plasma plume produced by the laser is always perpendicular to the target surface and sprays directly toward the substrate with a high concentration, PLD has a higher efficiency in thin film deposition and target

utilization than other film preparation methods, which is especially advantageous for preparing films containing toxic elements such as Pb. (iii) It can be operated under higher atmosphere pressure, especially for the film growth which requires an oxygen atmosphere. (iv) It can solve the problem of film preparation of many refractory materials, such as silicides, oxides, carbides, and borides, as the temperature of the target surface can be easily heated as high as 2000–3000 K to vapor any kinds of materials by the highly concentrated laser, which is difficult to achieve in other deposition techniques. In another aspect, PLD technique also has some drawbacks: (i) It is difficult to prepare uniform thin film with a large area, because the plume generated from the target by the irradiation of laser is highly directional with a solid angle  $2\theta_{\max} < 30^\circ$ , which is disadvantageous to prepare thin film with a uniform thickness and a large area. In order to overcome this drawback, a variety of complicated scanning methods are used, such as the substrate scanning, target scanning, and laser scanning. (ii) The film surface prepared by PLD may not be smooth and uniform enough compared with other methods, as the plume generated from the sintered polycrystalline target under the excitation of the high-energy, high-intensity, and high-momentum pulsed laser contains some large neutral particles in addition to the atoms, molecules, ions, etc., which results in the uneven growth of the thin film. In addition to optimizing the deposition conditions, methods of secondary laser ionization as well as placing velocity filter between the target and substrate are employed to prevent the large particles in the plume from arriving at the substrate and solve this problem. It is worth mentioning that the PLD system was equipped with a reflection high-energy electron diffraction (RHEED) for in situ monitoring the film growth process by Kanai et al. in the year 1991 [4], and a new updated PLD system named laser molecular beam epitaxy (laser MBE) was born, which marks a new stage in the development of PLD technology and is sufficient for the preparation of high-quality film by this method.

In the film preparing process via PLD technology, there are mainly three kinds of growth modes depending on factors such as the lattice mismatch between the film and substrate, surface energy of the film, and interface energy. They are island growth, layered growth, and mixed growth, as shown in Fig. 2.2.

(i) Island growth (Volmer–Weber mode, island growth, 3D): Due to the poor wettability between the film and the substrate, the film surface tends to form a smaller contact with the substrate, resulting in an island-like distribution of atom nucleation at the interface and three-dimensional growth of the nucleus. With the continuous growth of the atom islands during the deposition, islands are connected with each other and finally form the thin film. (ii) Layered growth (Frank-van der Merwe mode, layer-by-layer growth, 2D): Due to the good wettability between the film and the substrate, the film surface tends to form a larger contact with the substrate, resulting in a two-dimensional extension of atom nucleation at the interface and layer-by-layer growth of the thin film. (iii) Mixed growth (Stranski–Krastanov mode, layer plus island growth, 2D–3D): Despite the good wettability between the film and the substrate, the lattice parameters of the film and the substrate do not match with each other. As a result, the film first grows layer-by-layer to

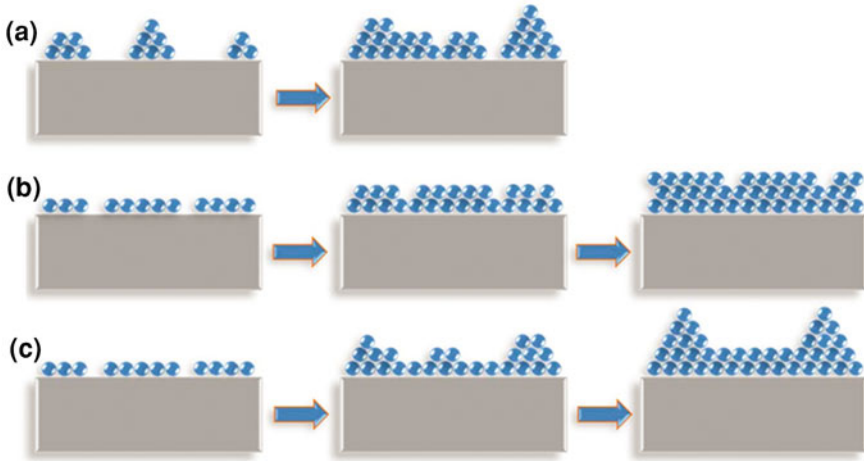


**Fig. 2.2** Three kinds of film growth modes in PLD technology: **a** island growth, **b** layer-by-layer growth, **c** mixed growth (Reprinted from Ref. [3], Copyright 2010, with permission from Elsevier)

reduce the interface energy and then it changes to island growth to reduce the strain energy.

Since the PLD technique can achieve the epitaxial growth of crystalline thin films without special limitation and requirements of the materials, it is easy to use this method for epitaxially growing different materials onto different substrates, forming different heterostructures or superlattice. Due to the lattice parameter mismatches between the films and substrates made from different materials, there are different epitaxial modes in film growth, including nearly perfectly lattice matched film growth, strained film growth, and relaxed heteroepitaxial film growth, as shown in Fig. 2.3, which can ultimately achieve the exact control of the film or interface resulting in interesting physical phenomena and issues [3].

### 2.1.2 Magnetron Sputtering Method

Magnetron sputtering is a kind of thin film preparing technology, in which high-energy particles or ions are employed to bombard the target for providing materials source for the thin film growth under the combined effects of the electric and magnetic fields, as shown in Fig. 2.4. The atoms and molecules of the target materials are sputtered out and deposited onto the substrate, as a result, a thin film with the component of the target materials can be prepared [5].

The working principle of the magnetron sputtering is described as follows. The target for sputtering is used as the cathode, behind which there is a piece of strong magnet (about 1,000 Gauss). The substrate to grow the thin film is used as the anode and placed on the substrate stage opposite the target. Before sputtering, the

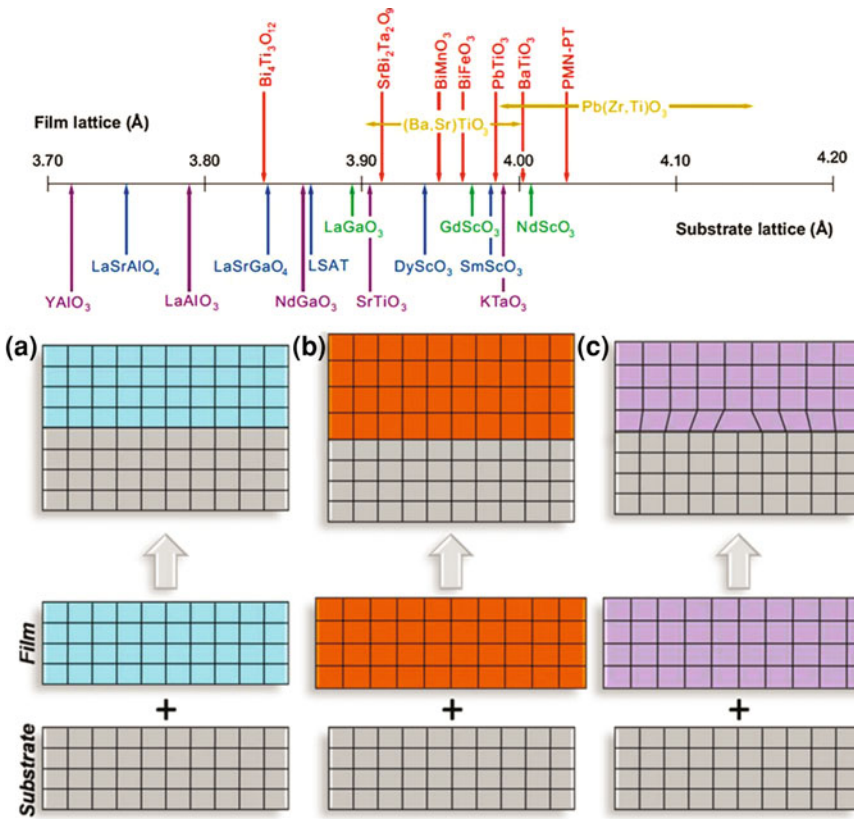
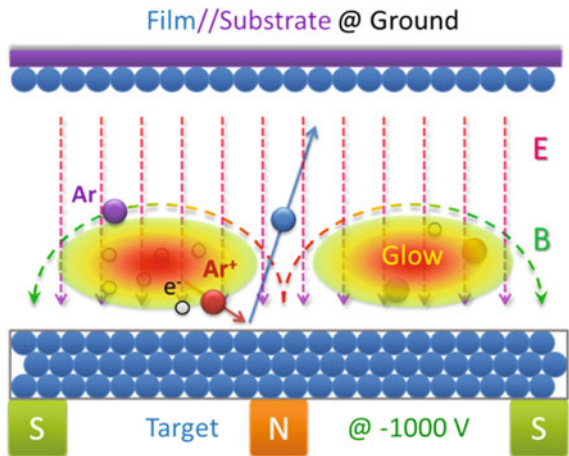
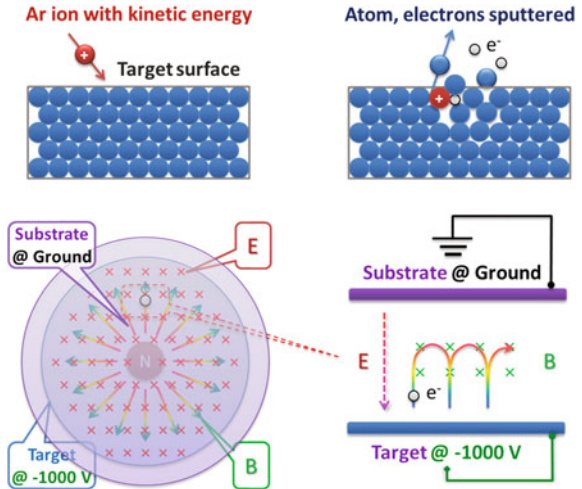


Fig. 2.3 Lattice parameters of different materials and different epitaxial modes: **a** matched growth, **b** strained growth, **c** relaxed heteroepitaxial growth (Reprinted from Ref. [3], Copyright 2010, with permission from Elsevier)

Fig. 2.4 Configuration of the magnetron sputtering device



**Fig. 2.5** Cycloid movement of the secondary electrons during sputtering



chamber should be pumped into vacuum and filled with a certain amount of inert gas (Ar) with the pressure about 0.1 Pa, which can be served as the carrier during discharge. When the high voltage is turned on, the electrons are accelerated by the electric field and rush toward the anode. During the running process from the cathode to the anode, the electron may collide with the argon atom, ionizing it and producing an  $\text{Ar}^+$  ion and a new electron (secondary electron). The negatively charged electron continuously flies toward the anode, and the positively charged  $\text{Ar}^+$  ion accelerates under the strong electric field, moves toward the cathode, and finally hits into the target surface with a high energy, engaging the sputtering. In the sputtering process, the neutral atoms or molecules of the target are bombarded and exited from the target surface by the  $\text{Ar}^+$  ions, sputtering onto the substrate and forming a thin film. The secondary electrons will be subject to the combined action of electric field and circular magnetic field after leaving the target surface, repeating a specific performance as follows. The secondary electron first enters the dark region near the cathode, in which it is accelerated by the electric field ( $E$ ) and begins to fly toward the glow region. Once in the glow region, the electron is exposed to the magnetic field ( $B$ ) and begins to rotate perpendicular to the magnetic field driven by the Lorentz force. After flying a half circle in the glow region, the electron returns to the dark region again near the cathode. Inside this dark region, the velocity of the electron is slowed down and reversed under the action of electric field. As a result, this electron speeds up again under the electric field and flies toward the glow region to start a new cycle. Thus, the electrons perform a circular cycloid motion repeatedly and drift around the target surface, as shown in Fig. 2.5. This ingenious design of magnetron sputtering extends the movement path of the electrons and bounds the electrons inside the plasma near the target surface, by means of which the probability of collision between the electrons and the inert gas and the efficiency of the energy utilizing of the electrons have been largely increased, ultimately making the sputtering more effective.

Compared with PLD, the magnetron sputtering method has the following advantages. (i) It can be used to grow thin films with a large area, good uniformity, and high flatness. (ii) Since the conditions of magnetron sputtering are relatively fixed, the deposition rate is pretty stable. By precisely controlling the sputtering time, the accurate thickness of the film can be easily controlled with good repeatability. (iii) Since the energy of electron or atom arriving at the substrates is relatively low, there is no obvious thermal effect generated on the substrate, which is important for the growth of some heat-sensitive materials. If needed, a cooling system can be integrated inside the substrate stage to keep the substrate at a certain low temperature and meet some special requirements. The disadvantages of the magnetron sputtering are mainly as follows. (i) In the preparation of multicomponent film, the sputtering efficiencies of different components in the target are different. As a result, the components of thin film prepared are not consistent with the components of the target, which is known as component segregation. (ii) Since the distribution of the magnetic field is limited inside a small circular space around the target, only a small circular region of the target is corroded by the ions during sputtering, forming a deep annular groove in the target. This nonuniform consumption of the target causes a serious waste of the target, with the utilization efficiency less than 50 %.

Overall, magnetron sputtering technology is a kind of effective film preparation method. With the continuous development of the relevant technologies, magnetron sputtering has been widely and successfully used in many areas, especially in the preparation of microelectronic devices, optical thin films, and the surface treatment of different materials, with a great significance [6].

## **2.2 Measurement, Characterization, and Analysis Techniques for Multiferroic Properties**

### ***2.2.1 Measurement and Characterization of Macroscopic Magnetic Properties***

Technologies used for characterization of the magnetic samples are various, while only a few of the magnetism measurement technologies related to the thesis work are introduced here. They are superconducting quantum interference devices (SQUID) used for measuring magnetization and magnetic hysteresis loop, electron spin resonance (ESR), and magneto-optical Kerr effect (MOKE) used for measuring the magnetic anisotropy.

*Superconducting quantum interference device* (SQUID) is an apparatus used for measuring weak magnetic signals or magnetic moments via the quantum interference effect of the superconductor, due to its sensitivity to the magnetic flux. The core assembly of the SQUID is called Josephson tunnel junction, which consists of

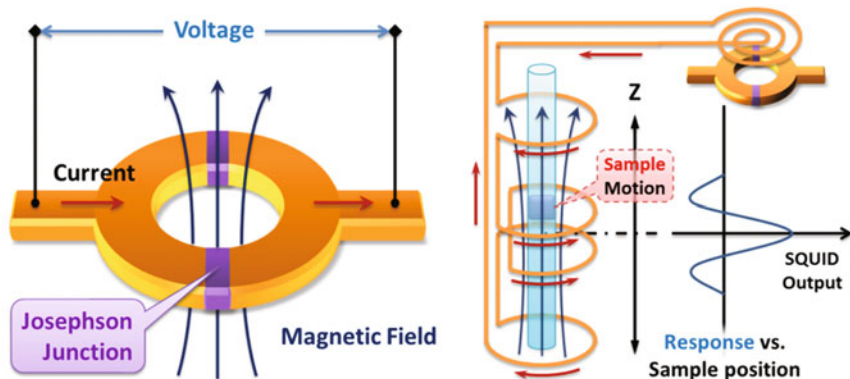
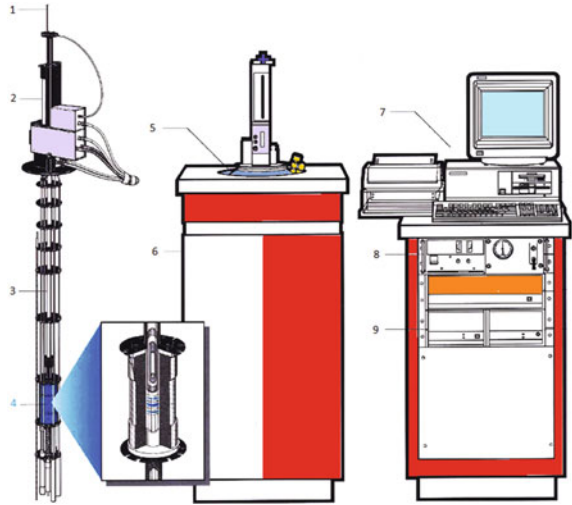


**Fig. 2.6** Configuration of Josephson junction (*left*) and the basic principle of SQUID (*right*)

two pieces of superconductors separated by a thin barrier layer. When the Josephson tunnel junction is connected to a superconducting circuit, a kind of macroscopic quantum interference phenomenon will present. That is, the voltage across the Josephson tunnel junction exhibits a periodic function with the change of magnetic flux inside the circuit. When a magnetic sample is moving in the superconducting coil, the change in the external magnetic flux will induce a change in superconducting current in the circuit. Due to the coupling attenuation in the SQUID, the changed current will change the magnetic flux in the Josephson tunnel junction and finally change the voltage of the device. SQUID is essentially a magnetic flux-voltage converter which can output voltage with amplitude proportional to the detected magnetic signal, as shown in Fig. 2.6. The minimum magnetic flux which can cause quantum interference phase change in the Josephson tunnel junction is a single flux quantum ( $\Phi_0 = 2.07 \times 10^{-15}$  Wb), thereby the SQUID has an ultra-high-sensitivity in detecting the magnetization [7, 8].

In addition to the function of accurate magnetization measurement, the SQUID is also an integrated magnetic property measurement system (MPMS) controlled by a computer with the ability of measuring all kinds of magnetic properties, such as saturated magnetization, coercivity, Curie temperature, and susceptibility, under variable temperatures and magnetic fields, as shown in Fig. 2.7. The MPMS employs a heater and liquid helium cooling system to control the temperature and utilizes the superconducting coil to generate strong and precision magnetic fields. Combined with different electrometers, the measurement of the electrical properties of the sample varying with temperature and magnetic field, such as the spin-dependent transport, can be achieved. The SQUID used in the work related to this thesis is a Quantum Design MPMS-XL, with the abilities of accurately controlling the temperature in the range of 1.9–800 K with a maximum rate up to 10 K per minute, accurately controlling the magnetic field in the range of  $-7.0$  to  $7.0$  T with the precision of 0.2 Oe, and accurately measuring the magnetic moments in the range of  $-2.0$  to  $2.0$  emu with the resolution of  $1 \times 10^{-8}$  emu.

**Fig. 2.7** Configuration and basic hardware parts of the MPMS: 1 sample rod, 2 sample transport, 3 sample chamber, 4 superconducting coils, 5 Dewar, 6 isolation cabinet, 7 computer, 8 controller units, 9 power units (Reprinted with permission from Ref. [8], Copyright Quantum Design 1994)



Despite the varied functions in measuring the magnetic properties, the existing MPMS cannot take the magnetic measurements under in situ electric fields, which is important for investigating ME coupling effect of the multiferroics in this thesis. After the pioneer work of a previous member in our group [9], we have developed MPMS and achieved the technique of measuring the magnetic properties under in situ electric field, which is significant for the investigation of multiferroic materials.

*Magnetic resonance* is a kind of phenomenon where materials with nonzero magnetic moments of atoms or nuclei exhibit obvious resonance absorption of the electromagnetic radiation under a static magnetic field, including nuclear magnetic resonance (NMR), paramagnetic resonance (PMR), optical magnetic resonance (OMR), and ferromagnetic resonance (FMR). If the magnetic resonance is caused by the magnetic moment of the electron spin in the material, it is called electron spin resonance (ESR) or electron paramagnetic resonance (EPR). Materials with unpaired electrons can be studied by the ESR method, such as atoms and molecules with an odd number of electrons, ions with unfilled inner electron shells, and radicals induced by radiation damage. The ESR spectra of the sample can give the information or states of the molecules, atoms, and ions related to the spin of electrons, and therefore, the ESR method has become an important experimental technique in modern physics, with wide applications in physics, chemistry, materials science, biology, medicine, and many other fields [10].

The basic principle of the ESR measurement is as follows. As we know, the spin orientations of an isolated electron have only two possible directions, which produce two possible spin-related magnetic moments  $\pm\mu_B$  ( $\mu_B$  is called Bohr magneton). When the electron is in an external magnetic field, the magnetic potential energy provided by the magnetic field will split the spin of the electron into two states (Zeeman effect), with the energy gap proportional to the magnetic

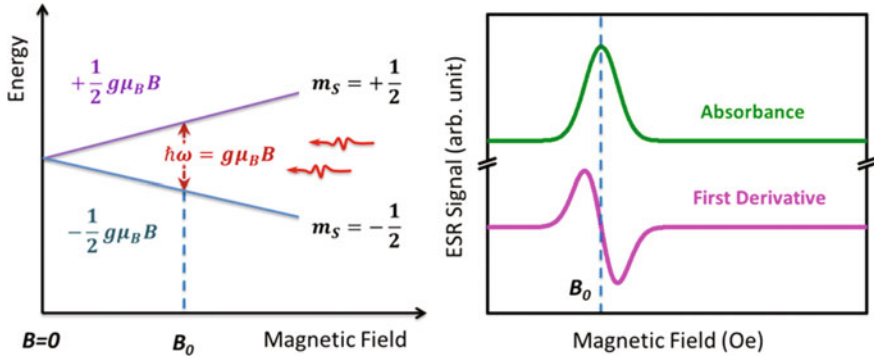


**Fig. 2.8** Principle of ESR (*left*) and derivation of the resonance field (*right*)

field  $\Delta E = g\mu_B B$  ( $g$  is called the electron spin  $g$ -factor). If an electromagnetic wave with an appropriate frequency  $\hbar\omega = \Delta E$  is applied along the vertical direction of the magnetic field, a transition from the low-energy spin state to the high-energy spin state can be induced, accompanied with a strong absorption of the incident electromagnetic wave and producing the ESR signal. By measuring the resonance frequency  $\omega$  and the corresponding external magnetic field  $B$ , the electron spin  $g$ -factor can be calculated and the atomic structure as well as other information related to the electron spin can be deduced. The resonance condition  $\hbar\omega = g\mu_B B$  can be achieved by either scanning the magnetic field  $B$  under fixed frequency  $\omega_0$  or scanning the frequency  $\omega$  under fixed magnetic field  $B_0$ . We employ the method of scanning magnetic field under fixed frequency to investigate the magnetic anisotropy in this thesis, from which the resonant magnetic field can be obtained by differentiating the ESR signal, as shown in Fig. 2.8.

*Magneto-Optical Kerr Effect (MOKE)* is one of the magneto-optical effects which occur in the interaction between light and magnetic materials. When a beam of linearly polarized light is incident to a magnetic thin film, part of the light will transmit through the magnetic material and part of the light will be reflected from the magnetized surface. The polarization directions as well as the intensities of both the transmitted light and reflected light will be changed, which are known as magneto-optical effects and can be divided into two kinds. The one that describes changes in light in the transmitted case is called Faraday effect, and the other that describes changes in light in the reflected case is called Kerr effect [11]. Thereby, the angles between the incident light and transmitted/reflected lights are called magneto-optical Faraday/Kerr rotation angles ( $\theta_F/\theta_K$ ), respectively, as shown in Fig. 2.9.

There are three kinds of configurations that are mostly used in the investigation of magnetic samples by MOKE, including (i) polar Kerr effect, in which the magnetization vector is parallel to the plane of incidence and perpendicular to the sample surface (i.e., reflection surface); (ii) longitudinal Kerr effect, in which the magnetization vector is parallel to both the plane of incidence and the sample surface;

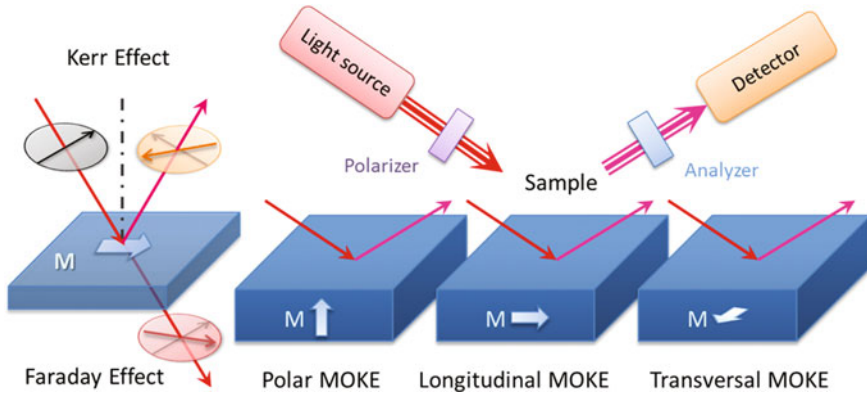


**Fig. 2.9** Classification of the magneto-optical effects and configurations of the Kerr effect

(iii) transversal Kerr effect, in which the magnetization is perpendicular to the plane of incidence and parallel to the sample surface, as shown in Fig. 2.9. Since the results of the MOKE measurement mainly reveal the information about magnetization at the sample surface, the MOKE is also called surface magneto-optical Kerr effect (SMOKE). Moreover, the amplitude and direction of the Kerr rotation angle  $\theta_K$  are related to the magnetization states of the sample near the surface. As a result, the local and surface magnetic hysteresis loop ( $M-H$ ) can also be obtained by the SMOKE method.

Considering the advantages and characteristics of the three kinds of magnetic measurement methods discussed above, we employ SQUID for the main magnetic measurements, such as magnetic hysteresis loops ( $M-H$ ) and in situ electrical control of magnetization, ESR to investigate the bulk magnetic anisotropy, and MOKE to detect the local and surface magnetic properties as well as the magnetic anisotropy evolution of the sample under in situ electric fields, respectively.

### 2.2.2 Characterization of Macroscopic Ferroelectric and Piezoelectric Properties

The most important feature indicating the ferroelectricity of material is the existence of spontaneous polarization and ferroelectric hysteresis loop, in which the polarization  $P$  can be switched hysteretically by an external electric field  $E$ . As a result, the ferroelectric hysteresis loop is also called  $P-E$  loop. From the  $P-E$  loop, the important parameters of the ferroelectric material, such as the spontaneous polarization  $P_S$  and the coercive electric field  $E_C$ , can be learned. Thereby, the  $P-E$  loop measurement of the ferroelectric materials is an important method to characterize the ferroelectric properties.

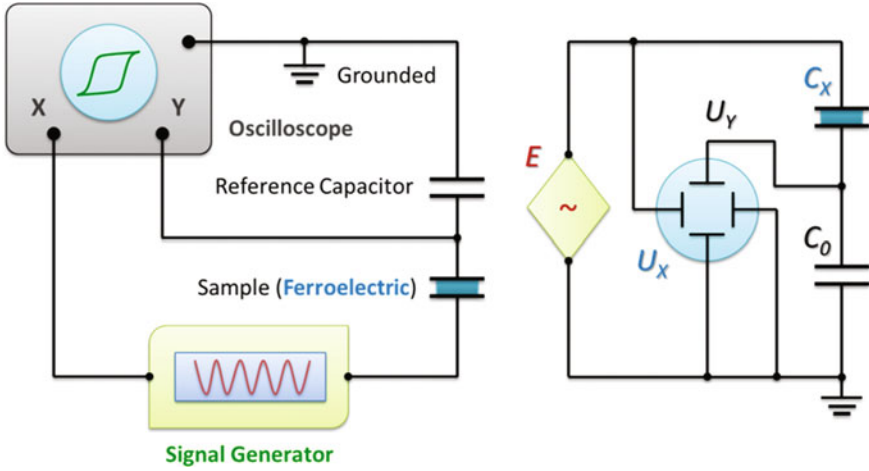


**Fig. 2.10** Configuration of the Sawyer-Tower circuit (*left*) and the equivalent circuit (*right*)

A conventional and most often quoted method for the  $P$ - $E$  loop measurement is called Sawyer-Tower circuit [12], which consists of an oscilloscope, a signal generator  $E$ , a reference capacitor  $C_0$ , and another capacitor  $C_x$  with the ferroelectric sample to be measured, as shown in Fig. 2.10. The basic principle and detailed working process are as follows. The signal generator generates an alternating electric signal in the circuit, which changes the current and charge in the electronic devices. Since the reference capacitor  $C_0$  and the sample capacitor  $C_x$  are series wound, they are loaded with the same amount of charge  $Q$ . For the situation of the reference capacitor  $C_0$ , there is equation  $Q = C_0 \times U_y$ , in which  $U_y$  is the voltage of  $C_0$ . Therefore, the charge  $Q$  of the sample capacitor  $C_x$  can be deduced from the reference capacitance  $C_0$  and the voltage  $U_y$  across it. As for the sample capacitor  $C_x$ , the polarization  $P$  of the ferroelectric sample is proportional to the charge  $Q$  of it according to the equation  $Q = P \times A$ , where  $A$  is the area of the electrode on the sample. Overall, the polarization  $P$  of the sample is proportional to the voltage  $U_y$  of the reference capacitor, so the electric signal  $U_y$  can wholly represent the ferroelectric polarization  $P$ . In another aspect, the voltages across the reference capacitor and sample capacitor can be expressed by equations  $U_x = Q/C_x$  and  $U_y = Q/C_0$ . In the design of the Sawyer-Tower circuit, the value of the reference capacitance  $C_0$  is larger than that of the sample capacitance  $C_x$ . Therefore, the voltage of the sample capacitance is larger than that of reference capacitance ( $U_x \gg U_y$ ), and  $U_x$  is approximately equal to the voltage of the signal generator  $E$ . Inputting  $U_x$  as the  $x$ -channel of the oscilloscope and  $U_y$  as the  $y$ -channel which represent the driving electric field  $E$  and polarization  $P$  of the sample, respectively, the ferroelectric hysteresis loop can be directly displayed on the oscilloscope.

In the Sawyer-Tower circuit, the reference capacitor  $C_0$  will induce a back voltage to the sample, and a parasitic capacitance  $C_p$  is inevitable during the charge and discharge process, which will affect the accuracy of the ferroelectric hysteresis

loop measurement. To overcome these defects, an integrated circuit with the virtual ground technique is employed for the Premier II-type ferroelectric hysteresis loop measurement system designed by Radiant Company. Using this measurement system, the ferroelectric samples can be effectively and accurately measured with a frequency range of 0.03–100 kHz, charge range of 0.80 fC–5.26 mC, and voltage range from –10 to 10 kV. On the other hand, the widespread problems in the ferroelectric thin film, such as the parasitic conductance (i.e., leakage), parasitic capacitance, and parasitic diode, can be possibly avoided by using the positive-up negative-down (PUND) method [13] or the double-wave method (DWM) [14] in the Radiant Premier II system, with the core idea that the remanent polarization  $P_r$  can be obtained by subtracting the electric signal without polarization switching from the electric signal with polarization switching. Since the most used ferroelectric samples in this thesis work are high-quality PMN-PT single crystals with high polarization and low leakage, the above problems do not exist in the measurement, and therefore, the PUND and DWM methods are not amplified here.

Generally speaking, the ferroelectric material is also piezoelectric, and the piezostain of the sample exhibits a *butterfly* behavior under bipolar electric field due to the polarization switching in the ferroelectrics. Under small electric field, the magnitude of the strain of the ferroelectric material is generally less than 0.1 %, and therefore, precision displacement measurement devices, such as laser interferometer and strain gauge, are employed for the piezostain measurement. Since the strain gauge measurement has advantages such as small size, flexible, and easy to be integrated, it has been successfully used to characterize the strain properties of the ferroelectric materials [15–18]. The basic principle of the strain gauge measurement comes from the law that the resistance of a sample varies with its geometrical dimensions. When the strain gauge and sample (ferroelectric or piezoelectric) are firmly bonded, the strain of the sample induced by the external electric field via converse piezoelectric effect will be transmitted to the strain gauge and changes the geometrical dimensions of the resistance wire, thereby changing the total resistance of the strain gauge. As a result, the strain of the sample can be deduced by measuring the resistance of the strain gauge. Since the strain of the sample is very small, the resistance change of the strain gauge is also small. To detect this slight change in resistance, the quarter-bridge (Wheatstone bridge) is employed to realize the precise strain measurement, as shown in Fig. 2.11. Thanks to the flexibility of the strain gauge-based measurement method, we can easily obtain the strain in any direction of the ferroelectric sample by aligning the sensitive direction of the strain gauge with the interested direction of the sample while bonding. Moreover, by combining the strain gauge with a temperature controlling equipment such as SQUID in an automatic controlling program, we have successfully developed an integrated system with the function of measuring strain as well as other properties of the ferroelectric sample under low temperature, which has expanded the scope of strain investigation in materials. Since the work related to strain measurement in this thesis is mainly at room temperature, the low-temperature strain measurement system is not necessary to be introduced here.

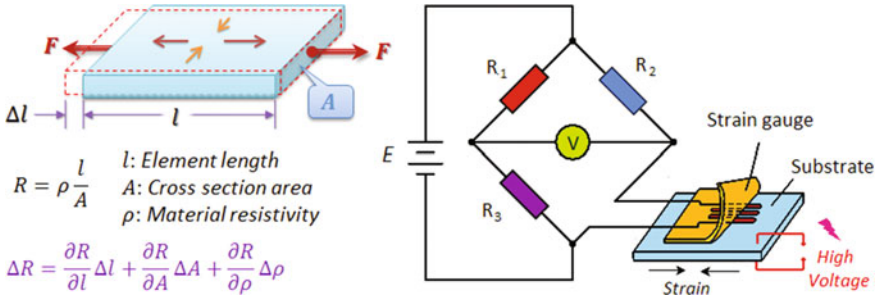


**Fig. 2.11** Basic principle of the strain gauge (*left*) and configuration of the strain measurement of piezoelectric/ferroelectric samples (*right*)

### 2.2.3 Characterization of Microscopic Ferromagnetic and Ferroelectric Properties

The microscopic characterization techniques for the multiferroic samples in this thesis are mainly based on the scanning probe microscopy (SPM), which is a new kind of microscopic characterization technology developed from the scanning tunneling microscopy (STM) and involves a variety of new functional microscopies, such as atomic force microscopy (AFM), lateral force microscopy (LFM), magnetic force microscopy (MFM), and piezoresponse force microscopy (PFM). The common feature of these techniques is that they employ a sharp tip to scan the sample surface and probe the local information with contact or non-contact modes, for which they are collectively called SPM [19, 20]. Using different kinds of tips which have different kinds of interactions with the sample surface, different kinds of physical properties of the sample can be probed with the different operating modes in SPM, described as follows.

*The basic principle and work process of AFM* are described as follows. Just as a blind man using a stick to explore the obstacles on the road ahead of him, the AFM technique employs a sharp tip to probe the sample within a very short distance to the surface and scans the tip in two dimensions for imaging. The positions of the tip which contain the height information about the sample surface can be amplified by an optical lever method and detected by the laser beam deflection in a four-quadrant detector, as shown in Fig. 2.12. However, in the real imaging process, the tip maintains a fixed contacting force or tapping amplitude with the sample surface, controlled by a feedback system. Therefore, the height information about the undulating sample surface can be reflected in the feedback system, which finally gives the topography. Since the dominant interactions between the tip and the sample surface are van der Waals forces between molecules and atoms, this kind of microscopic characterization technique is called atomic force microscopy.

*The magnetic force microscopy (MFM)* is a functionalized variant of atomic force microscopy, in which a sharp magnetized tip is employed in the two-dimensional scanning to detect the magnetic signals of the magnetic samples and

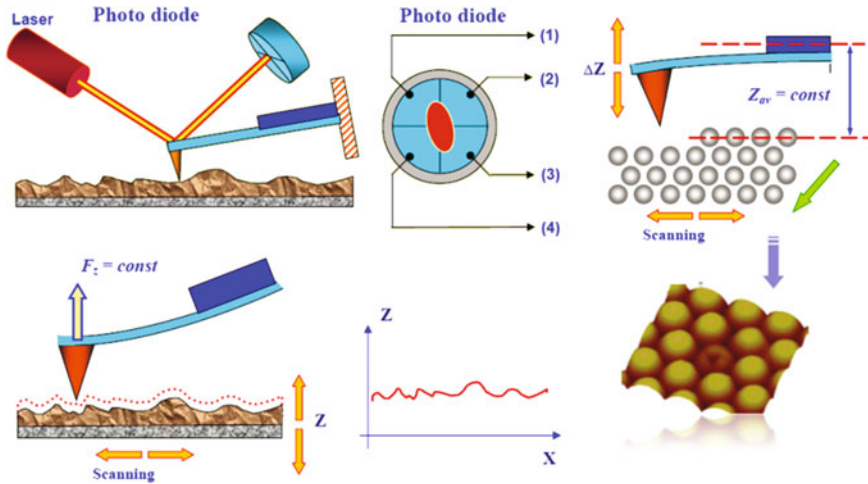


**Fig. 2.12** Basic principle and configuration of AFM (Reprinted with permission from Ref. [20], Copyright 2004 NT-MDT, All right reserved)

reconstruct the magnetic structure of the sample surface [21]. The scanning operation in MFM is relatively complicated with a lift mode, in which each line of the sample surface must be scanned twice. First, the tip carries on the scanning closely to the sample surface ( $<10$  nm), in which not only the magnetic forces are sensed, but also the van der Waals forces. Then, the tip is lifted further away from the sample surface (usually 10–200 nm) and scans the sample along the topographic profile obtained from the first scanning. On this second pass, since the short-range van der Waals force between the tip and the sample atoms does not exist, only the magnetic forces related to the gradient of the leakage magnetic field near the sample surface are detected and the effects of the undulating sample surface can be ruled out by the profile-consulted scanning. As a result, the magnetic signal is extracted and the magnetic domains can be reconstructed together with the topography, as shown in Fig. 2.13. Limited by the working principle, the MFM can only observe the magnetic domain structure perpendicular to the sample surface. However, compared with the optical method used for the magnetic domain observation, the MFM has higher resolution with detailed magnetic information and is significant for the investigation of micromagnetics.

The *piezoresponse force microscopy* (PFM) is another functionalized variant of atomic force microscopy, which utilizes the converse piezoelectric effect to investigate the ferroelectric domain structure or piezoelectric coefficients of ferroelectric samples. The working principle of PFM is described as follows. When a small alternative electric field is applied onto the sample via a conductive tip, different kinds of surface deformation can be induced by the AC voltage depending on the piezoresponse of different ferroelectric domains. For example, ferroelectric domain with polarization downward will always exhibit in-phase piezoelectric resonance, in which the ferroelectric domain stretches under positive

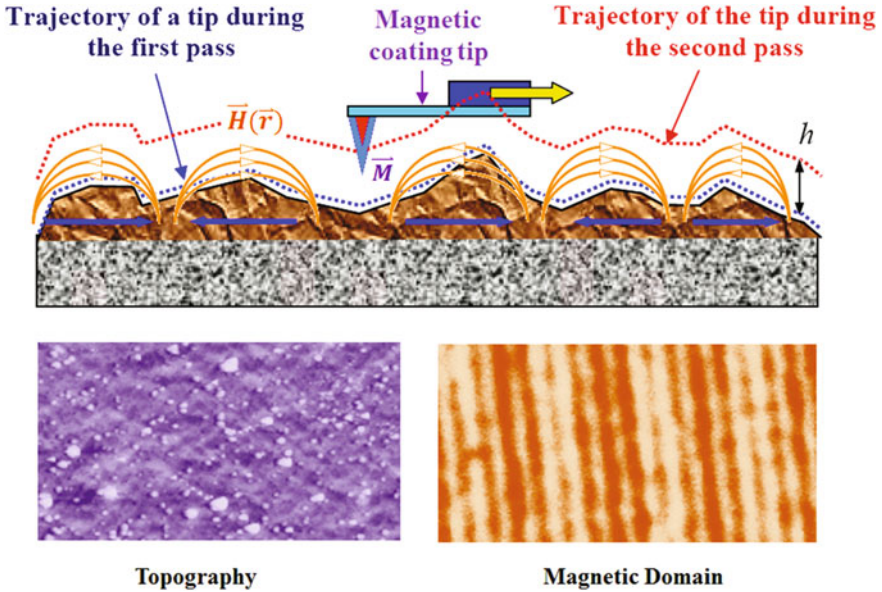


**Fig. 2.13** Basic principle and operation process of MFM (Reprinted with permission from Ref. [20], Copyright 2004 NT-MDT, All right reserved)

electric field and contracts under negative electric field. As for the situation with polarization upward, the piezoresponse of the ferroelectric domain is opposite to the AC driving electric field, which is called out-of-phase piezoelectric resonance. Using the lock-in amplifier, the amplitude and phase information can be deduced from the piezoresponse signal, which reflect the piezoelectric coefficients (such as  $d_{33}$  and  $d_{15}$ ) and the polarization orientations of the ferroelectric domains, as shown in Fig. 2.14. As a result, the ferroelectric domain structure can be reconstructed in terms of amplitude and phase images via the two-dimensional scanning of the sample surface. By PFM, various ferroelectric samples have been successfully characterized with a better understanding of the ferroelectricity in the microscale [22, 23].

In the PFM measurement process, the tip and sample surface keep in contact with each other (contact mode) to detect the piezoresponse of the ferroelectric domains. If the ferroelectric sample under measurement is single crystal with a rhombohedral structure such as  $\text{BiFeO}_3$  [24], the spontaneous polarizations of the sample, which have eight possible directions lying along the diagonal of the pseudo-cubic unit cell, have not only out-of-plane components but also in-plane ones. As a result, the tip on top of the ferroelectric domain can not only feel the piezoelectric component with direction perpendicular to the sample surface, but also feel the piezoresponse along the in-plane direction. The out-of-plane piezoresponse will move the tip up and down under AC driving signal, while the in-plane one will twist the tip left and right. Both the in-plane and out-of-plane tip

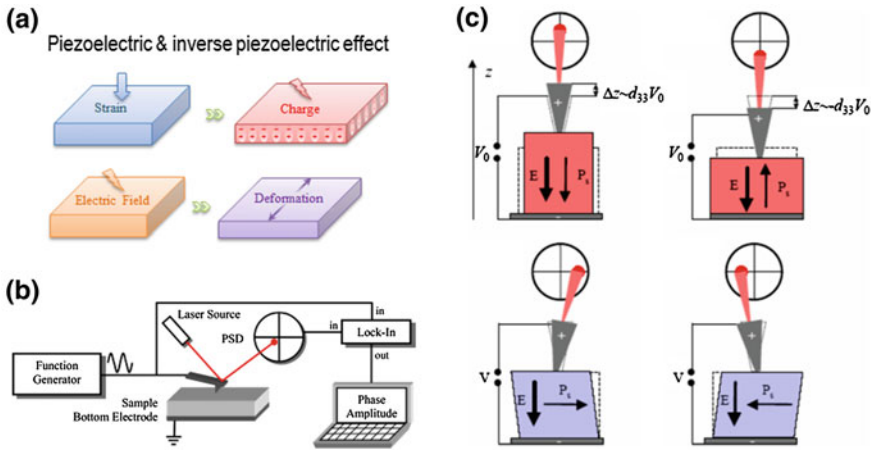


**Fig. 2.14** The **a** piezoelectric effect, **b** configuration and **c** the basic principle of PFM (Reproduced from Ref. [22] by permission of John Wiley & Sons Ltd.)

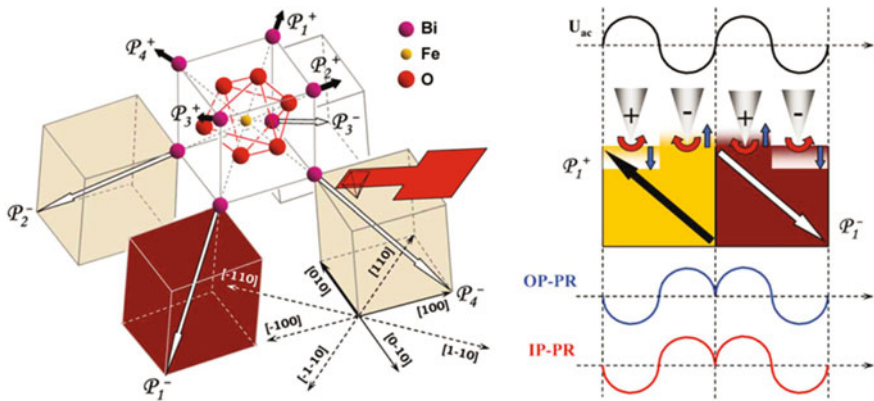


**Fig. 2.15** Piezoresponse of different polarization vectors to the PFM tip (Reprinted from Ref. [24] by permission of Taylor & Francis Ltd.)

movements can be sensed and quantified by the quadrant photodetector, which change the lateral and vertical deflections, respectively. According to the in-plane and out-of-plane piezoresponse obtained by PFM, the domain structure as well as the polarization orientation of the sample can be reconstructed, as shown in Fig. 2.15.

Notably, since the in-plane piezoresponse component with direction parallel to the tip cantilever cannot be detected, the in-plane ferroelectric domain image will exhibit different results depending on the orientation of the tip cantilever. Especially in some directions, the contrast of in-plane phase image will exhibit triple

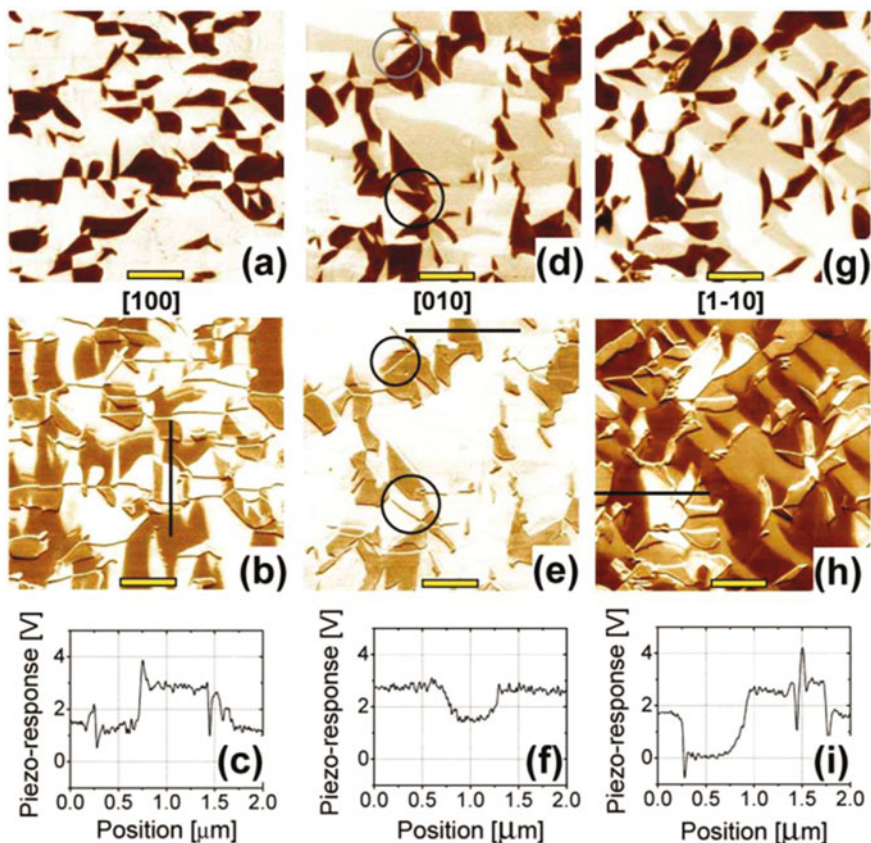


**Fig. 2.16** Out-of-plane (a, d, g) and in-plane (b, e, h) PFM phase images as well as in-plane piezoresponse signals (c, f, i) with tip cantilever along different directions (Reprinted from Ref. [24] by permission of Taylor & Francis Ltd.)

colors, representing polarization pointing left, right, and along the cantilever direction. However, the out-of-plane ferroelectric domain image does not exhibit much difference with the variation in cantilever direction, with a typical two-color contrast in the phase image, as shown in Fig. 2.16.

Moreover, it is also possible to switch the polarizations of the ferroelectric domains by the DC bias voltage applied on the sample through the tip and perform the in situ observation via PFM, as shown in Fig. 2.17, which is helpful to thoroughly investigate the different domain switching categories and further understand the dynamic process of domain switching in ferroelectric materials.

The SPM system used in the work related to this thesis is MultiMode-8 microscope equipped with NanoScope V controller produced by the Veeco Instruments Inc. This SPM system has a variety of functions such as the AFM, MFM, and PFM as described above, by which the surface topography, magnetic

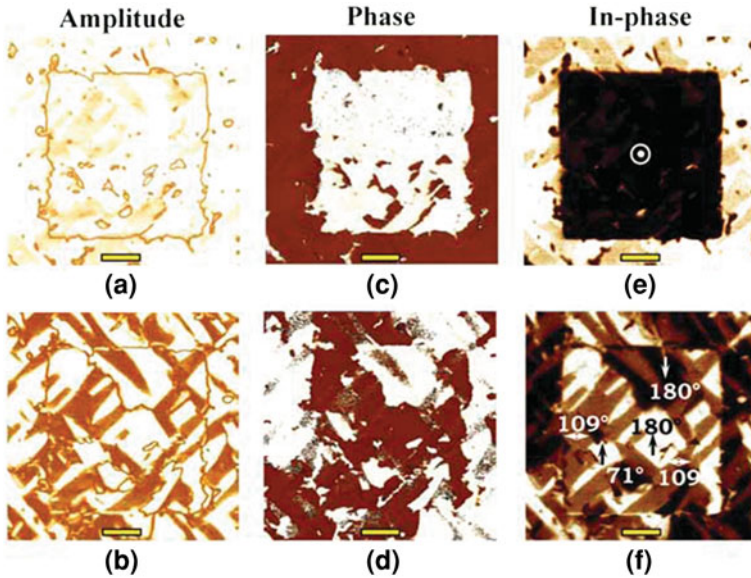


**Fig. 2.17** Domain switching investigation by PFM: **a, b** the amplitude images **c, d** out-of-plane phase images **e, f** in-plane phase images (Reprinted from Ref. [24] by permission of Taylor & Francis Ltd.)

domain, and ferroelectric domain of the sample can be measured. Moreover, photoemission electron microscopy (PEEM) has also been attempted in part of the work to visualize the in-plane magnetic domain [25]. Since the work is mainly completed by collaborators, the PEEM method is not enlarged here.

#### **2.2.4 X-ray Diffraction Techniques and Crystal Structure Analysis**

X-ray diffraction (XRD) is a kind of diffraction phenomenon that originates from the interaction between the X-ray and atoms inside materials. If the material has a crystal structure which consists of atoms with periodic arrangement, regular diffraction patterns will be generated. By analyzing the diffraction patterns, the structure and lattice parameters of the crystal can be deduced. Therefore, XRD has been a powerful and commonly used characterization method in determining the crystal structure, crystallographic plane orientation, texture, and grain size of materials [26].

The basic principle of XRD is described as follows. A beam of collimated X-ray is incident to a crystal surface with lattice parameter  $d$  at an angle  $\theta$ . If the

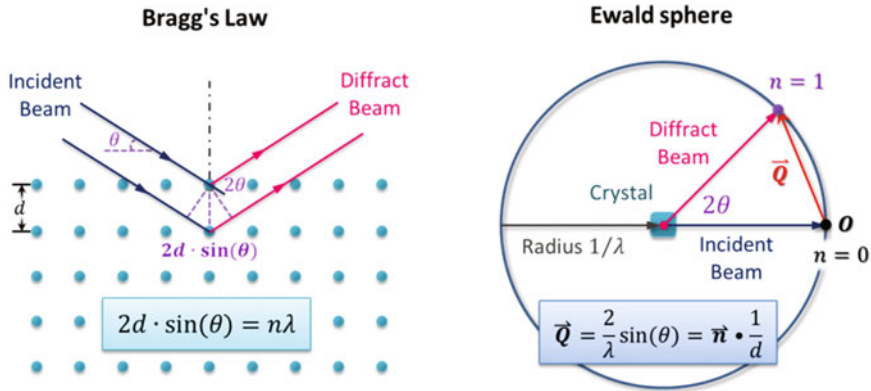


Fig. 2.18 Bragg's law (left) and the Ewald sphere (right)

incident light and diffraction light meet certain condition, the diffraction light will be enhanced due to superposition, which generates the regular diffraction spot. The diffraction condition required for the superposition can be simply described by Bragg's law:  $2d_{hkl} \cdot \sin(\theta) = n\lambda$ , where  $d_{hkl}$  is the interplanar distance between crystal faces,  $\theta$  is the angle between the incident light and the sample surface,  $n$  is the diffraction order, and  $\lambda$  is the wavelength of the X-ray. The Bragg's law describes the requisite condition for X-ray diffraction in real space. As for the reciprocal space, Bragg's law can be easily transformed into a simple geometric description, namely Ewald sphere, as shown in Fig. 2.18.

In the experiment, the XRD diffractometer has a complicated three-dimensional (3D) configuration with many tunable perimeters and different kinds of scanning modes. The use of Ewald sphere has largely simplified the 3D configuration and is helpful for understanding the relationship between different perimeters in XRD. The real space parameters in the 3D configuration of XRD include incident vector  $\mathbf{K}_0$ , diffraction vector  $\mathbf{K}$ , diffraction angle  $2\theta$ , and the orientation angle of the sample surface  $\omega$ , while in the reciprocal space, parameters are reduced to a simple reciprocal vector  $\mathbf{Q}$  with two orthonormal components, i.e.,  $Q_z$  and  $Q_x$ , as shown in Fig. 2.19.

According to the relationship between the real space coordinates and reciprocal space coordinates, transformation of the parameters in real space and reciprocal space can be deduced as follows:

$$\begin{aligned} Q_x &= K[\cos(\theta - \omega) - \cos(\theta + \omega)] \\ Q_z &= K[\sin(\theta - \omega) - \sin(\theta + \omega)] \end{aligned} \quad (2.1)$$

in which  $K = 2\pi/\lambda$  is the radius of the Ewald sphere and is also used as the primitive vector in reciprocal space. The restrictions in the reciprocal space, which are determined by Bragg's law and the geometrical configuration in real space, can be expressed as follows:

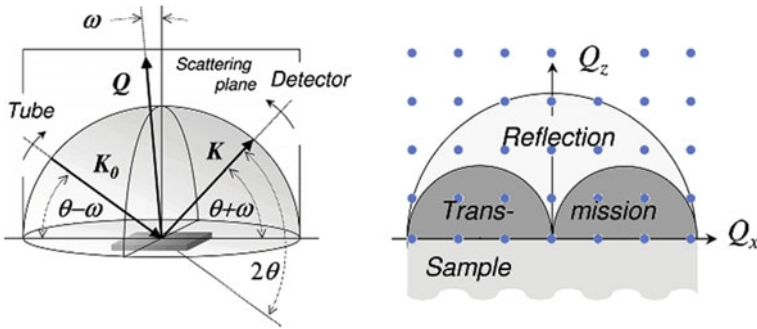


**Fig. 2.19** Parameter corresponding between real space (left) and reciprocal space (right) (Reproduced from Ref. [26] with permission from John Wiley & Sons Ltd.)

$$\begin{aligned}
 -2K &\leq Q_x \leq 2K \\
 0 &\leq Q_z \leq 2K \\
 Q_x^2 + Q_z^2 &\leq 4K^2
 \end{aligned}
 \tag{2.2}$$

The common scanning modes of XRD have three different cases, including  $\theta$ - $2\theta$  linkage scanning,  $\omega$  scanning (also known as the rocking curve scanning), and  $\omega$ - $2\theta$  linkage scanning (a kind of 2D mapping scanning, also known as the reciprocal space mapping, RSM [27]).

The  $\theta$ - $2\theta$  linkage scanning is the most commonly used scanning method in XRD, in which the direction of the incident X-ray is fixed and the Bragg diffraction condition is achieved by rotating the sample and the detector in the diffraction plane. When the sample rotates an angle  $\theta$ , the detector has to rotate  $2\theta$  in order to meet the Bragg condition. As a result, this kind of scanning mode is called  $\theta$ - $2\theta$  linkage. In the reciprocal space, this kind of scanning mode corresponds to an equivalent motion that the reciprocal diffraction vector  $Q$  scans in one dimension along the  $Q_z$ -axis, as shown in Fig. 2.20a. Thereby, the crystal information and lattice parameter perpendicular to the sample surface can be detected.

The  $\omega$  scanning or rocking curve scanning refers to a kind of scanning method in which the directions of the incident X-ray and X-ray detector are fixed at the position that a certain diffraction peak appears, and the Bragg diffraction condition is achieved by rocking the normal direction of the sample surface in the diffraction plane. In the reciprocal space, this kind of scanning mode corresponds to an equivalent motion that the reciprocal diffraction vector  $Q$  takes a one-dimensional scanning along the arc of a circle with the radius  $Q$ , as shown in Fig. 2.20b. According to the rocking curve obtained from the  $\omega$  scanning, full width at half maximum (FWHM) of the diffraction peak can be deduced, which is an important index to characterize the quality of a crystal sample. Generally speaking, if the FWHM value of a crystal sample is small, i.e., the corresponding rocking curve is narrow, the crystal is supposed to be in a good uniformity and crystallinity.

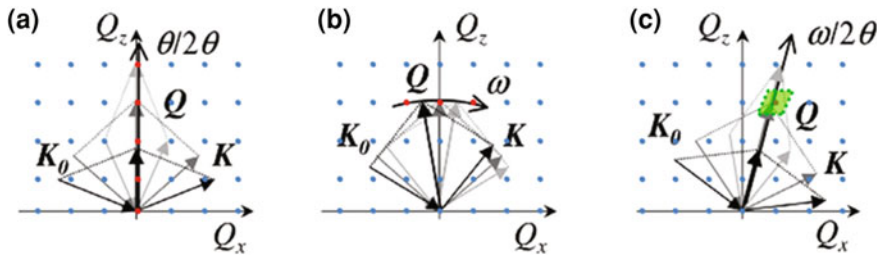


**Fig. 2.20** Reciprocal space configurations of the three kinds of scanning methods: **a**  $\theta$ - $2\theta$  linkage scanning, **b**  $\omega$  scanning, and **c**  $\omega$ - $2\theta$  linkage scanning (Reproduced from Ref. [26] by permission of John Wiley & Sons Ltd.)

The  $\omega$ - $2\theta$  linkage scanning (RSM scanning) is a kind of scanning method that combines the  $\theta$ - $2\theta$  linkage with the  $\omega$  scanning, and the detailed operation process is described as follows. First, the normal direction of the sample surface is fixed at a certain angle  $\omega$ , and then the  $\theta$ - $2\theta$  linkage scanning is performed. After that, the normal direction of the sample surface is rotated to another angle  $\omega + \Delta\omega$ , and then the  $\theta$ - $2\theta$  linkage scanning is performed for another time. Repeating the above process by continuously taking the  $\theta$ - $2\theta$  linkage scanning under stepping changed  $\omega$  value, the  $\omega$ - $2\theta$  linkage scanning can be achieved. In the reciprocal space, this kind of scanning mode corresponds to an equivalent motion that the reciprocal diffraction vector  $\mathbf{Q}$  takes a two-dimension scanning in a small parallelogram around a reciprocal lattice point, as shown in Fig. 2.20c. Utilizing this kind of scanning method, various information about the crystal sample such as the in-plane and out-of-plane lattice parameters, quality of the epitaxial film, and elastic distortion of the unit cell can be quantitatively or qualitatively determined from the RSM results, which have vital significance and wide applications in material science [28, 29].

In addition to the three kinds of scanning methods described above, there is another kind of scanning mode in XRD named  $\varphi$  scan, in which the sample has to rotate along its surface normal direction ( $\varphi$ ) to meet the Bragg diffraction condition. In  $\varphi$  scan, the directions of the incident X-ray and X-ray detector are fixed at the positions that meet the diffraction condition of a certain crystal face, and the selected crystal face is always not parallel to the sample surface but is at an angle to it. In the sample rotation along its surface normal direction, diffraction peaks can be detected whenever the selected crystal face or the equivalent one appears. As a result, the in-plane symmetry of the sample and the relative lattice orientation between the epitaxial film and the single crystal substrate can be detected by the  $\varphi$  scanning method.

The model of X-ray diffractometer employed in the investigations related to the thesis is Rigaku-D/max-RB, equipped with Cu target as the emitter of X-ray with the wavelength of  $K_\alpha \sim 1.5406 \text{ \AA}$ . To realize high-quality X-ray with good parallelism and single wavelength for accurate XRD measurement, restrictive slits

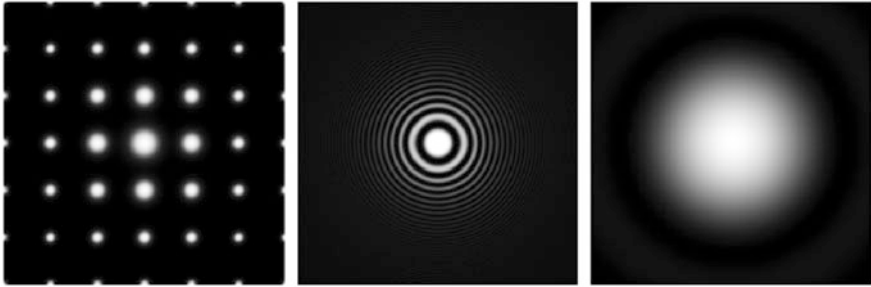


**Fig. 2.21** Three kinds of diffraction patterns in TEM (simulated results): single crystal (*left*), polycrystalline (*middle*), and amorphous (*right*)

and monochromators are placed in the emitter and detector of X-ray. In the measurement of polycrystalline samples, the size of slits are set as follows: emitting slit  $1^\circ$ , receiving slit  $1^\circ$ , and divergence slit 0.3 mm. As for the measurement of single crystals or epitaxial thin films, the value of each slit should be reduced by half and attenuation sheet should be inserted into the detector to protect the instrument due to the high diffraction intensity. What is more, other kinds of X-ray diffractometer have also been used by the collaborators in Hefei and Shanghai light source to accomplish part of this thesis work, which is not elaborated here.

In the characterization techniques for the micro-/nano-structures, there is another powerful instrument named *transmission electron microscope (TEM)*, which has ultra-high resolution and the ability of atomic level imaging. The basic principle of TEM is similar to the optical microscope, except the fact that electron beam is used as the light source and electric/magnetic fields are used as lens in the TEM imaging. Since the wavelength of the electrons is very small, image with atomic-scale resolution can be obtained by the TEM technique. However, as the penetrating ability of the electron beam is weak, samples to be characterized by TEM have to be prepared into ultra-thin slices (generally less than 100 nm), which is a difficult task. In addition to directly imaging the samples at the atomic level, TEM has another basic function of carrying out the electron diffraction. Similar to X-ray diffraction, the behavior of electron diffraction also obeys the Bragg's law  $2d \cdot \sin(\theta) = n\lambda$ , only the  $\lambda$  here is the wavelength of electrons. From the diffraction pattern of TEM, the crystal morphology and structure of the sample can be easily determined, which can be divided into three kinds of categories with different diffraction patterns, including single crystal, polycrystalline, and amorphous structure, as shown in Fig. 2.21. The diffraction pattern of the single crystal sample consists of ordered lattices, i.e., the reciprocal lattice of the single crystal. The diffraction pattern of the polycrystalline sample consists of many concentric rings, in which the finer the ring is, the larger the grain size will be. The diffraction pattern of the amorphous sample exhibits a diffuse halo-like form, due to the absence of ordered crystal lattice inside the materials.

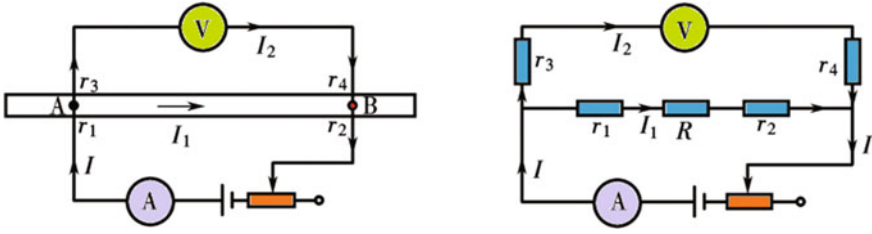


**Fig. 2.22** Two-wire method for the resistance measurement: schematic circuit (*left*) and equivalent circuit (*right*)

### 2.2.5 Electrical Transport Measurement Technique and Photolithography

The most frequent task in the electrical experiments is the measurement of resistance. There are a lot of factors that affect the accuracy of resistance measurement. For example, the precision of instrument is one of the key factors, and on the other hand, the design of measurement circuit is also important which is related to the contact resistance. Generally, the two-wire method is often adopted in resistance measurements, as shown in Fig. 2.22.

In the circuit,  $R$  is the true resistance of the sample,  $r_1$  and  $r_2$  are the contact resistance induced by the access of current,  $r_3$  and  $r_4$  are the contact resistance induced by the access of voltmeter. The internal resistance of an ideal voltmeter in circuit can be considered as infinity; therefore, the currents in the two-wire circuit satisfy the following relations:  $I_2 \ll I_1$  and  $I_1 - I$ . As for the voltage measurement, the visual value is equal to  $U_{r_1} + U_R + U_{r_2}$ , and therefore, the calculated resistance of the sample is  $r_1 + R + r_2$ . If the resistance of the sample is very large, i.e.,  $R \gg r_1$  and  $R \gg r_2$ , the result of the two-wire measurement is approximate to the true value  $R$ . However, in the case that  $R$  is small or high requirement of measurement precision, e.g., the measurement of magnetoresistance in CoFeB structures, the two-wire method is no longer viable. The contact and lead resistance in circuit cannot be avoided, but can be eliminated by a so-called four-wire method as shown in Fig. 2.23, which is important to measure the resistivity of metal or semiconductor materials.

In the case that all the conditions in the two-wire and four-wire circuits, such as the sample resistance  $R$ , the contact resistance  $r_1, r_2, r_3, r_4$ , and the equivalent condition  $I_1 - I$  for an ideal voltmeter, are similar to each other, one can see that the visual voltage is  $U_R$  and the calculated resistance is  $R$ , which is equal to the true value of the sample, as revealed from the equivalent circuit in Fig. 2.23b.

In this thesis, the involved measurements of magnetoresistance and investigation of the electric field control of magnetization in the CoFeB/PMN-PT structure are carried out in the MPMS, which provides a stable and controllable magnetic field and temperature environment. Different kinds of electrometers are integrated with MPMS and employed in the four-wire method, in which Keithley 2400 is

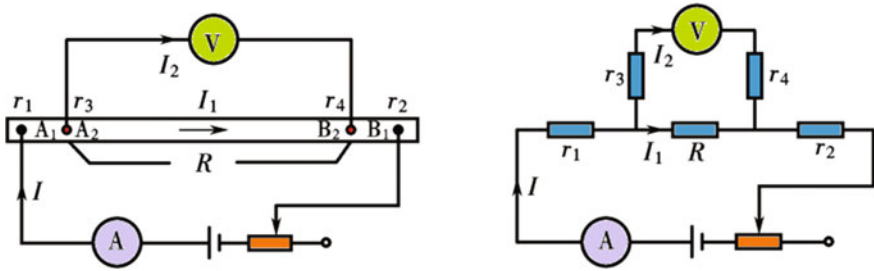


**Fig. 2.23** Four-wire method for the resistance measurement: schematic circuit (*left*) and equivalent circuit (*right*)

used as the constant current source, Keithley 2182 is used as the voltmeter, and Keithley 6517A is used for applying high voltage. Moreover, lithography technique and mask design are also needed for the preparation of spintronic devices. Since this part of work is done by collaborators, the lithography technique is not described here.

## References

1. D. Dijkkamp, T. Venkatesan, X.D. Wu et al., Preparation of Y-Ba-Cu-O oxide superconductor thin films using pulsed laser evaporation from high  $T_c$  bulk material. *Appl. Phys. Lett.* **51**, 619–621 (1987)
2. D.B. Chrisey, G.K. Hubler, *Pulsed Laser Deposition of Thin Films* (Wiley-Interscience, New York, 1994)
3. L.W. Martin, Y.H. Chu, R. Ramesh, Advances in the growth and characterization of magnetic, ferroelectric, and multiferroic oxide thin films. *Mater. Sci. Eng. R-Reports* **68**, 133 (2010)
4. M. Kanai, T. Kawai, S. Kawai, Atomic layer and unit cell layer growth of (Ca, Sr)CuO<sub>2</sub> thin film by laser molecular beam epitaxy. *Appl. Phys. Lett.* **58**, 771–773 (1991)
5. P.J. Kelly, R.D. Arnell, Magnetron sputtering: a review of recent developments and applications. *Vacuum* **56**, 159–172 (2000)
6. W.J. Xu, Recent developments and applications in magnetron sputtering. *Mod. Instrum.* **5**, 1–10 (2005). (in Chinese)
7. J. Clarke, SQUID: for superconducting quantum interference devices. *Sci. Am.* **271**, 46 (1994)
8. M. Mcelfresh, *Fundamentals of Magnetism and Magnetic Measurements* (Purdue University, Quantum Design, USA, 1994)
9. J.J. Yang, Tunability of the electric and magnetic properties in multiferroic heterostructures. Doctoral Thesis, Tsinghua University, 2010. (in Chinese)
10. W. Ning, Investigation of perovskite manganites by electron spin resonance. Doctoral Thesis, Institute of Physics CAS, 2008. (in Chinese)
11. J. Lee, J. Jeong, D. Kim et al., Three-configurational surface magneto-optical Kerr effect measurement system for an ultrahigh vacuum in situ study of ultrathin magnetic films. *Rev. Sci. Instrum.* **71**(10), 3801–3805 (2000)

12. G. Ornelas-Arciniega, J. Reyes-Gomez, A.G. Castellanos-Guzman, A new modification to the Sawyer-Tower ferroelectric hysteresis loop tracer. *J. Korean Phys. Soc.* **32S**, S380–S381 (1998)
13. S.M. Feng, Y.S. Chai, J.L. Zhu et al., Determination of the intrinsic ferroelectric polarization in orthorhombic  $\text{HoMnO}_3$ . *New J. Phys.* **12**, 073006 (2010)
14. M. Fukunaga, Y. Noda, New technique for measuring ferroelectric and antiferroelectric hysteresis loops. *J. Phys. Soc. Jpn.* **77**, 064706 (2008)
15. T. Wu, A. Bur, P. Zhao et al., Giant electric-field-induced reversible and permanent magnetization reorientation on magnetoelectric  $\text{Ni}/(011)[\text{Pb}(\text{Mg}_{1/3}\text{Nb}_{2/3})\text{O}_3](1-x)-[\text{PbTiO}_3]x$  heterostructure. *Appl. Phys. Lett.* **98**, 012504 (2011)
16. J. Ma, Y.H. Lin, C.W. Nan, Anomalous electric field-induced switching of local magnetization vector in a simple  $\text{FeBSiC-on-Pb}(\text{Zr, Ti})\text{O}_3$  multiferroic bilayer. *J. Phys. D-Appl. Phys.* **43**, 012001 (2010)
17. C. Thiele, K. Dorr, O. Bilani et al., Influence of strain on the magnetization and magnetoelectric effect in  $\text{La}_{0.7}\text{A}_{0.3}\text{MnO}_3/\text{PMN-PT}(001)$  ( $A = \text{Sr, Ca}$ ). *Phys. Rev. B* **75**, 054408 (2007)
18. Z.Y. Feng, D. Lin, H.S. Luo et al., Effect of uniaxial stress on the electromechanical response of  $\langle 001 \rangle$ -oriented  $\text{Pb}(\text{Mg}_{1/3}\text{Nb}_{2/3})\text{O}_3\text{-PbTiO}_3$  crystals. *J. Appl. Phys.* **97**, 024103 (2005)
19. L. Han, H.M. Chen, X.F. Wang, The application of the scanning probe microscopy in the GaAs semiconductor. *Funct. Mater.* **2**, 32–35 (1999). (in Chinese)
20. V.L. Mironov, *Fundamentals of Scanning Probe Microscopy* (Institute of Physics of Microstructures, The Russian Academy of Science, Nizhniy Novgorod, 2004)
21. H. Zhong, Quantitative investigation of magnetic nanostructures by magnetic force microscopy. Doctoral Thesis, Tsinghua University, 2009. (in Chinese)
22. N. Balke, I. Bdikin, S.V. Kalinin et al., Electromechanical imaging and spectroscopy of ferroelectric and piezoelectric materials: state of the art and prospects for the future. *J. Am. Ceram. Soc.* **92**(8), 1629–1647 (2009)
23. J.Y. Dai, J.X. Wang, Study of the ferroelectric domain structure and evolution in  $\text{PMN-30 \% PT}$  single crystal by means of piezoresponse force microscopy (in English). *Prog. Phys.* **2**, 197–214 (2009)
24. F. Zavaliche, S.Y. Yang, T. Zhao et al., Multiferroic  $\text{BiFeO}_3$  films: domain structure and polarization dynamics. *Phase Transitions* **79**, 991–1017 (2006)
25. S. Anders, H.A. Padmore, R.M. Duarte et al., Photoemission electron microscope for the study of magnetic materials. *Rev. Sci. Instrum.* **70**, 3973–3981 (1999)
26. M. Birkholz, P.F. Fewster, C. Genzel, *Thin Film Analysis by X-Ray Scattering* (WILEY-VCH Verlag GmbH, Weinheim, 2006)
27. P.F. Fewster, Reciprocal space mapping. *Crit. Rev. Solid State Mater. Sci.* **22**, 69–110 (1997)
28. H.J. Liu, P. Yang, K. Yao et al., Twinning rotation and ferroelectric behavior of epitaxial  $\text{BiFeO}_3$  (001) thin film. *Appl. Phys. Lett.* **96**, 012901 (2010)
29. G.Y. Gao, S.W. Jin, W.B. Wu, Lattice-mismatch-strain induced inhomogeneities in epitaxial  $\text{La}_{0.7}\text{Ca}_{0.3}\text{MnO}_3$  films. *Appl. Phys. Lett.* **90**, 012509 (2007)

# Chapter 3

## Electric-Field Control of Magnetism in CoFeB/PMN-PT(001) Structure

### 3.1 Introduction

As mentioned in Chap. 1, the investigation of multiferroic materials and magneto-electric (ME) coupling is an important and difficult issue, which has not only profound significances in physics, but also great prospects in application. On the one hand, the coexistence and coupling between different ferroic orders in multiferroic materials have brought some interesting phenomena as well as new challenges related to strongly correlated electron systems, which inspire new research hotspots in the area of condensed matter physics and materials science [1]. On the other hand, multiferroic material is a new type multifunctional material with ME coupling effects, including electrical control of magnetization and magnetic field manipulation of polarization, which have broad applications in spintronics, magnetic sensors, and many other areas.

However, single phase multiferroic materials which exhibit simultaneous magnetic and ferroelectric orders are rather rare at room temperature and the ME coupling coefficients are always too small to be useful. Thereby, artificial two-phase multiferroic system consisting of ferroelectric (FE) and ferromagnetic (FM) materials has provided an alternative way to achieve multiferroicity with large magnetic coupling effects at room temperature and has been extensively studied in recent years [2]. To realize electric-writing and magnetic-reading energy efficient memories for the next generation, the investigation related to electric-field control of magnetism has drawn much of the scientific research, in which the strain-mediated ME coupling effect has been widely reported in FM/FE heterostructures, such as  $\text{La}_{0.67}\text{Sr}_{0.33}\text{MnO}_3/\text{PMN-PT}$  [3],  $\text{Fe}/\text{BaTiO}_3$  [4, 5],  $\text{FeCoV}/\text{PZN-PT}$  [6],  $\text{CoFe}_2\text{O}_4/\text{PMN-PT}$  [7],  $\text{FeGaB}/\text{PZN-PT}$  [8],  $\text{Fe}_3\text{O}_4/\text{PZT}$ ,  $\text{Fe}_3\text{O}_4/\text{PMN-PT}$  [9],  $\text{ZFO}/\text{PMN-PT}$  [10],  $\text{FeBSiC}/\text{PZT}$  [11],  $\text{Ni}/\text{BaTiO}_3$  [12],  $\text{Ni}/\text{PZT}$ ,  $\text{Fe-Ge}/\text{PZT}$ ,  $\text{Fe-Ge}/\text{BSPT}$  [13],  $\text{Ni}/\text{PMN-PT}/\text{Ni}$  [14], and so on.

For the electric-field control of magnetism, both switchable and nonvolatile are important for the information storage. Although electrical modulation of magnetization has been widely achieved at room temperature in the strain-mediated multiferroic system as mentioned above, the bipolar-electric-field-controlled

magnetization generally exhibits a reversible *butterfly-like* behavior, which is a kind of volatile ME coupling and disadvantageous for applications, for the piezostrain will be vanished when the driving electric field is removed in this system. As a result, a switchable and nonvolatile electrical control of magnetization at room temperature is highly desired in the FM/FE compound multiferroic system. In another aspect, the mechanism for the ME coupling effect in the strain-mediated multiferroic system has been simply understood as the macroscopic piezostrain of the FE substrate transferred onto the FM layer, which changes the magnetic anisotropy. Besides, the microscopic ME coupling between the ferroelectric and ferromagnetic domains at the interface of the FM/FE heterostructure is also another important mechanism for the electric-field control of magnetization, which has been generally ignored but offers an opportunity to achieve nonvolatile converse ME effects [15]. Thereby, the investigation of electrical control of magnetism based on the microelastic coupling between ferroelectric and ferromagnetic domains is an interesting and a significant issue with prospective applications.

In recent years, the ferroelectric relaxor-based single crystals, such as lead magnesium niobate—lead titanate  $\text{Pb}(\text{Mg}_{1/3}\text{Nb}_{2/3})\text{O}_3\text{-xPbTiO}_3$  (PMN-*x*PT) and lead zinc niobate—lead titanate  $\text{Pb}(\text{Zn}_{1/3}\text{Nb}_{2/3})\text{O}_3\text{-xPbTiO}_3$  (PZN-*x*PT) have drawn much interest of the scientific research in materials science and physics due to the excellent ferroelectric and piezoelectric properties, which can be used for high-performance electromechanical actuators [16, 17]. Employed as the ferroelectric substrates, PMN-PT, and PZN-PT have been widely used in the compound multiferroic heterostructures, to realize electrical control of magnetization via their giant piezostrain. What's more, with component near morphotropic phase boundary (MPB) [18], the (001)-oriented PMN-PT single crystal exhibits various ferroelectric phases and complicated domain structures, as shown in Fig. 3.1. As a result, we choose PMN-PT as the ferroelectric substrate to investigate the electric-field control of magnetism, in order to achieve a kind of nonvolatile ME effect in virtue of the ferroelectric domain switching effect.

On the other hand,  $\text{Co}_{40}\text{Fe}_{40}\text{B}_{20}$  (CoFeB) belongs to the class of amorphous ferromagnetic Co-Fe-B alloys, which exhibits perfect soft ferromagnetism [19] without magnetocrystalline anisotropy and possesses the highest spin polarization among Co-Fe-B compounds [20] with a large tunneling magnetoresistance (TMR) in magnetic tunnel junctions. Considering the absence of magnetocrystalline anisotropy and the low coercive field, it is interesting to explore the electric-field control of magnetism of CoFeB thin film in the FM/FE heterostructure which is helpful for realizing strain-mediated magnetoelectric random access memory.

Based on the above considerations, we choose the artificial CoFeB/PMN-PT(001) FM/FE heterostructure to investigate the electrical control of magnetization as well as the ME coupling effect in the compound multiferroics [21].

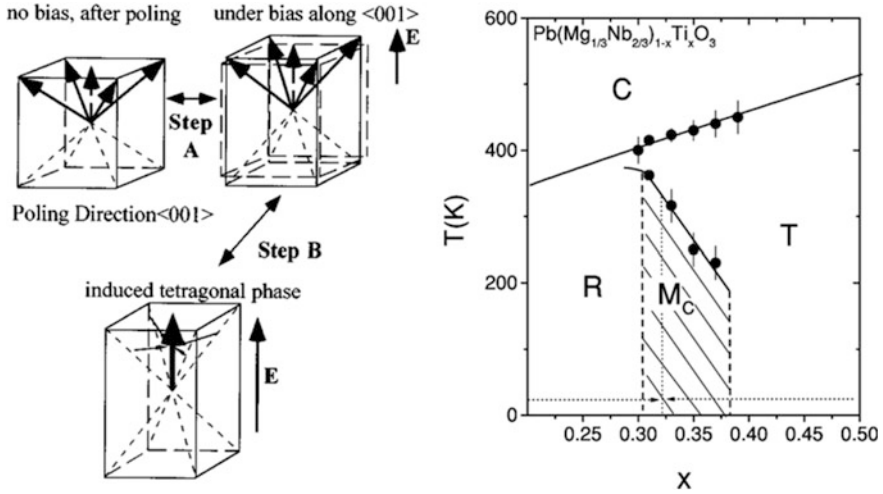


**Fig. 3.1** Domain structure (left, Reprinted with permission from Ref. [16]. Copyright 1997, American Institute of Physics) and phase diagram (right, Reprinted with permission from Ref. [18]. Copyright 2002 by American Physical Society) of PMN-PT

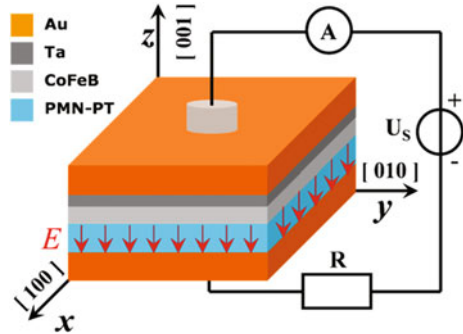
## 3.2 Sample Preparation and Characterization

### 3.2.1 Sample Preparation

Since the growth technology of PMN-PT has been well developed, commercial (001)-oriented PMN-30 %PT single crystal was one-side polished and cut into a slab with a size of  $3 \times 2.5 \times 0.5 \text{ mm}^3$ , which was used as the FE substrate to grow the ferromagnetic film. Amorphous  $\text{Co}_{40}\text{Fe}_{40}\text{B}_{20}$  film with a thickness of 20 nm was deposited on top of the PMN-PT substrate and followed by a 10 nm tantalum (Ta) via an ultra-high vacuum (ULVAC) magnetron sputtering system with a base pressure of  $1 \times 10^{-6} \text{ Pa}$ . The high vacuum environment and capping layer of Ta are essential for preventing the active elements such as cobalt (Co) and iron (Fe) in the CoFeB thin film from being oxidized during deposition and after taking out of the chamber. Compared with the pulsed laser deposition (PLD), the growth temperature of the magnetron sputtering method is low. As a result, the problem related to volatilization of lead (Pb) in PMN-PT substrate at high temperature can be avoided during deposition, which ensures the reliability of the sample components.

Since the investigation of electrical control of magnetization needs to be carried on with in situ electric field, gold (Au) layers with a thickness of 300 nm were sputtered on both the top and bottom sides of the CoFeB/PMN-PT FM/FE multiferroic heterostructure as electrodes. When applying the electric field, copper (Cu) wires with a diameter of 100  $\mu\text{m}$  was connected to the electrodes on the sample surfaces with silver (Ag) paste. The whole structure of the sample and configuration of the electric circuit are shown in Fig. 3.2, in which the sample side with

**Fig. 3.2** The CoFeB/PMN-PT multiferroic heterostructure and configuration of applying electric field (Reprinted with permission from Ref. [21]. Copyright 2012 by American Physical Society)



Au/Ta/CoFeB was defined as the positive electrode and the high voltage ( $U_s$ ) is provided by a Keithley 6517 A source meter. Moreover, a Keithley 2400 ammeter (A) together with a 16 M $\Omega$  protecting resistor (R) were series-wound in the circuit, to monitor the current and protect the sample as well as measurement system under high voltage during all the measurements performed at room temperature.

### 3.2.2 Texture Characterization of the Sample

In order to determine the orientation and quality of the PMN-PT single crystal as well as the amorphous features of CoFeB thin film, a Rigaku-D/max-RB X-ray diffractometer was employed in the texture characterization and the relevant results are shown in Fig. 3.3.

From Fig. 3.3a, we can see that the PMN-PT single crystal substrate has an accurate (001) orientation and the lattice parameters along the c-axis of PMN-PT can be calculated as 4.02 Å according to the position of the diffraction peak, which is consistent with the previous report [18]. Meanwhile, the rocking curve of the PMN-PT substrate has also been measured and the result around (002) diffraction peak is shown in Fig. 3.3b. From the figure, we can see the full width at half maximum (FWHM) of the (002) rocking curve is approximate to 0.17°, which means that the PMN-PT single crystal has a good quality. Moreover, we do not see the polycrystalline peaks of Co and Fe in the figures above, which means that the texture of CoFeB grown by magnetron sputtering is fully amorphous.

Moreover, by collaboration with professor Zhang's group in Department of Materials Science, Tsinghua University, transmission electron microscope (TEM) was employed to directly visualize the microstructure of the CoFeB/PMN-PT sample, and the results are shown in Fig. 3.4. From the low-resolution TEM image in Fig. 3.4a, we can see a wide range of uniform, continuous and smooth CoFeB film distributed on the PMN-PT substrate with a clear boundary. From the high-resolution TEM image in Fig. 3.4b, we can clearly see a high quality ordered lattice structure in the PMN-PT region instead of CoFeB region, which further confirms the crystalline structure of PMN-PT and amorphous structure of CoFeB.

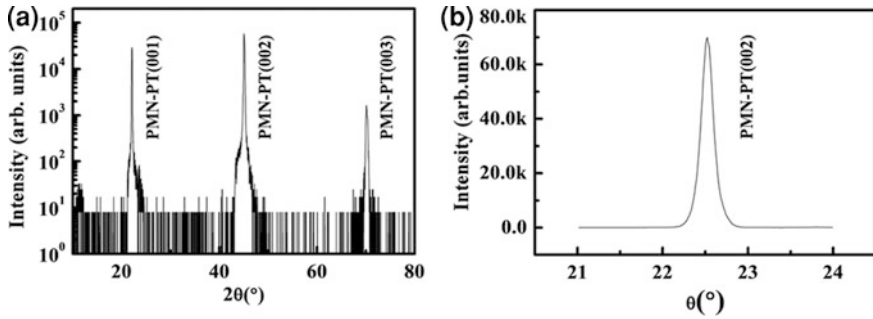


**Fig. 3.3** XRD characterization of the CoFeB/PMN-PT heterostructure: **a**  $\theta$ - $2\theta$  linkage scanning, **b** rocking curve scanning

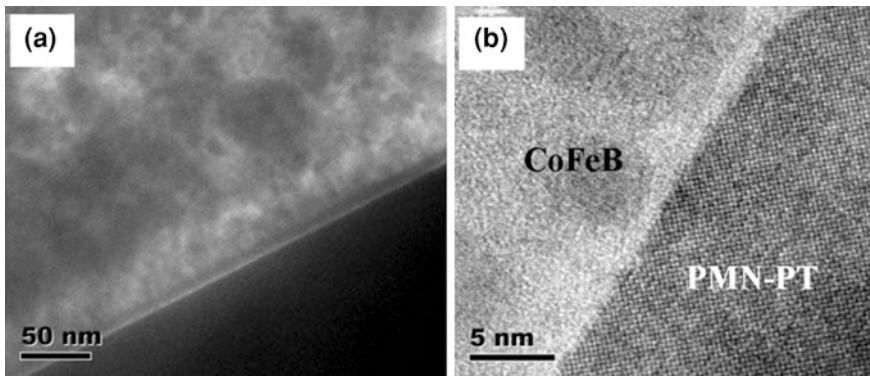


**Fig. 3.4** TEM cross-sectional images of the CoFeB/PMN-PT heterostructure: **a** low-resolution, **b** high-resolution

### 3.2.3 Characterization of Ferroelectric and Piezoelectric Properties

Premier II ferroelectric analyser produced by Radiant Company was employed to characterize ferroelectric properties of the sample, and the result is shown in Fig. 3.5a. From the ferroelectric hysteresis loop (P-E) of the sample, one can see the coercive field of PMN-PT substrate is about 2 kV/cm and the saturated polarization is about 25  $\mu\text{C}/\text{cm}^2$ . Meanwhile, the switching current during polarization reversal and leakage current at high voltage of the sample were automatically recorded by the ammeter in the circuit as shown in Fig. 3.2, and the current-voltage (I-V) curve is shown in Fig. 3.5b. As one can see from the figure, a giant current peak with maximum value about 0.5  $\mu\text{A}$  appears when the electric field is around the coercive field of PMN-PT, which can be easily understood as the switching current due to polarization reversal. When the electric field exceeds the coercive field of PMN-PT, the current will decrease rapidly with leakage current less than 20 nA under electric

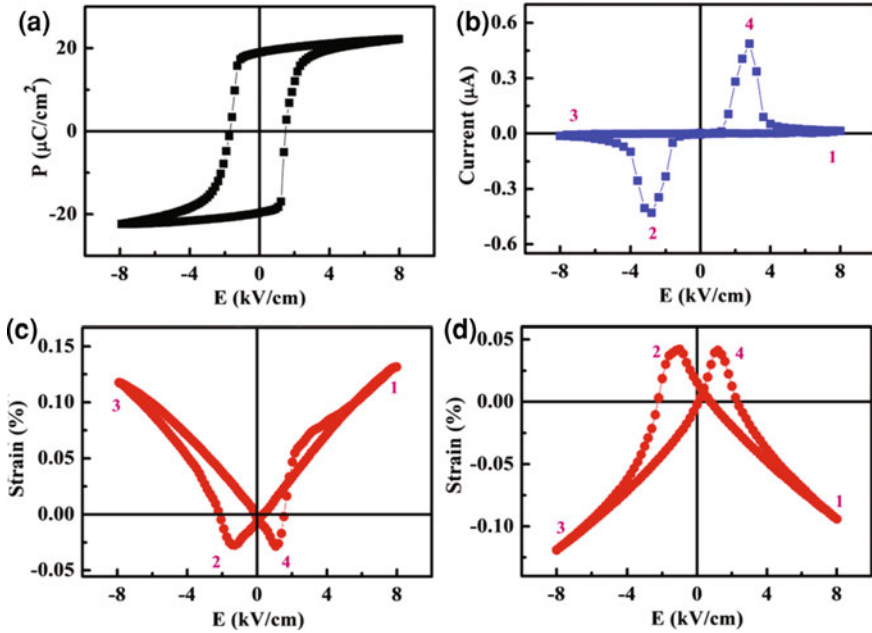


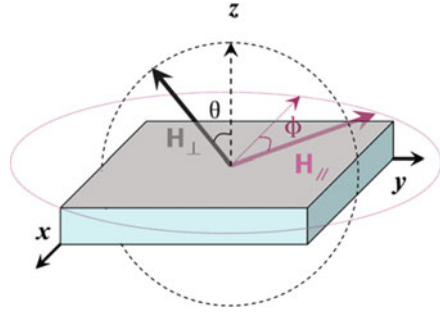
**Fig. 3.5** Ferroelectric and piezoelectric properties of PMN-PT: **a** P-E loop, **b** polarization current, **c** out-of-plane and **d** in-plane piezostain curves

field of 8 kV/cm, indicating that the PMN-PT sample we used here has good performances in ferroelectricity and insulation, which is important for our subsequent investigation of electric control of magnetization.

Besides, we also employed laser interferometer based on the Radiant-Premier II system and self-building strain measurement system based on strain gauge to characterize the strain properties of PMN-PT out of plane and in plane, respectively. The out-of-plane and in-plane piezostain results of PMN-PT are shown in Fig. 3.5c and d, both of which exhibit butterfly-like behaviors in strain electric field (S-E) curves. The out-of-plane strain value of PMN-PT reaches up to 0.15 % under electric field of 8 kV/cm and the in plane one is about 0.08 % at 8 kV/cm, which are consistent with the previous reports [3, 16]. In the above electrical measurements, the polished side of PMN-PT with CoFeB is defined as the positive electrode and the numbers marked in Fig. 3.5b–d are used to guide the sequence of applying electric fields and the measurement order.

By the basic structural and physical characterizations of the CoFeB/PMN-PT sample as prepared, we can see the properties of the compound FM/FE heterostructure are normal as expected and meet the basic requirements of multiferrocity, which lay a good foundation for the further investigation of the electric-field control of magnetism in the CoFeB/PMN-PT heterostructure.

**Fig. 3.6** Configuration of the ESR measurement (Reprinted with permission from Ref. [21]. Copyright 2012 by American Physical Society)



### 3.3 Electric-Field Control of Magnetism

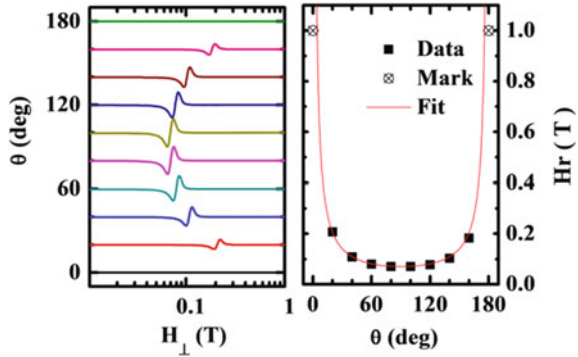
In order to study the magnetic response of the sample under external electric field, various magnetic characterization methods with in situ electric field are employed for different functional measurements, i.e., using the electron spin resonance (ESR) technique to measure the magnetic anisotropy of the sample, using the superconducting quantum interference device (SQUID) to measure the magnetization, and using the magnetic force microscopy (MFM) to measure the magnetic domain structure, all of which are described as follows.

#### 3.3.1 Electric-Field Control of Magnetic Anisotropy

Via collaboration with Sun's group in Institute of Physics, Chinese Academy of Science, a 9.51 GHz JEOL JES-FA200 electron spin resonance system was employed to characterize the magnetic anisotropy of the sample, as shown in Fig. 3.6.

We firstly use the ESR method to investigate the out-of-plane magnetic anisotropy of the sample, as shown in Fig. 3.6. Defining the angle between the direction of magnetic field and the normal line of the sample surface as  $\theta$ , ESR measurement was performed at different angles  $\theta$  under control of the instrument via sample rotation. In this situation, when  $\theta$  is equal to 0 or  $180^\circ$  (i.e., magnetic field is perpendicular to the sample surface), the out-of-plane ESR signal can be obtained, and in case of  $\theta = 90^\circ$  (i.e., magnetic field is parallel to the sample surface), the in-plane ESR signal can be obtained. The results of out-of-plane ESR signal and deduced resonance magnetic field ( $H_r$ ) which change along with the angles  $\theta$  are shown in Fig. 3.7. From the figure, we can see that the minimum resonance magnetic field is about 750 Oe at  $\theta = 90^\circ$ . As the angle gradually deviates from  $90^\circ$ , the resonance magnetic field increases, from 750 Oe to more than 1 T (10000 Oe) at  $\theta = 0$  or  $180^\circ$ . The reason for this phenomenon can be

**Fig. 3.7** The out-of-plane ESR signal and resonance magnetic field ( $H_r$ ) of the sample gathered at different angles (Reprinted with permission from Ref. [21]. Copyright 2012 by American Physical Society)



understand as the large out-of-plane demagnetization field exists in the CoFeB thin film, which forces the magnetic moments lying only in plane. As a result, the plane of the sample surface is the easy plane of magnetization, and the normal direction of the sample surface is the hard direction of magnetization. In this regard, we mainly focus on the in-plane magnetic anisotropy of the CoFeB film, which can be more easily tuned by the external electric fields.

Afterward, the in-plane magnetic anisotropy of the sample was investigated by the ESR method, as shown in Fig. 3.6. Defining the angle between the direction of magnetic field and the [00-1] direction of the sample as  $\varphi$ , ESR measurement was performed at different angle  $\varphi$  under control of the instrument via circularly rotating sample in plane, and the results are shown in Fig. 3.8.

Without electric field, the resonance magnetic field ( $H_r$ ) of the as-grown CoFeB film displays almost a circular shape in the polar graph shown as (■) in Fig. 3.8b with a fitted average  $H_r = 765.8$  Oe and uniaxial magnetic anisotropy field  $H_u = 13.7$  Oe. The anisotropic ratio ( $H_u/H_r$ ) is about 1.7 %, which can be considered as magnetic isotropy in plane and is consistent with the magnetic property of the amorphous CoFeB film. When the sample is poled by a positive electric field of +8 kV/cm, we find the resonance magnetic field of the CoFeB film varies with the angle  $\varphi$  as shown in the left panel of Fig. 3.8a and the deduced resonance magnetic field ( $H_r$ ) exhibits a *dumbbell-like* curve in the polar graph shown as (●) in Fig. 3.8b, which indicates that the sample changes to a uniaxial magnetic anisotropy state with the easy axis of magnetization along the [110] direction and hard axis along the [-110] direction. The fitted average resonance magnetic field ( $H_r$ ) and uniaxial magnetic anisotropy field ( $H_u$ ) in the positive poled case are equal to 738.9 and -71.2 Oe, respectively, with anisotropic ratio  $H_u/H_r = -9.6$  %. In the negative poled case under electric field of -8 kV/cm, the uniaxial magnetic anisotropy becomes stronger with fitted values of  $H_r = 730.7$  Oe,  $H_u = -93.1$  Oe,  $H_u/H_r = -12.7$  % and the easy axis of magnetization remains almost unchanged, which is shown as (▲) in Fig. 3.8b.

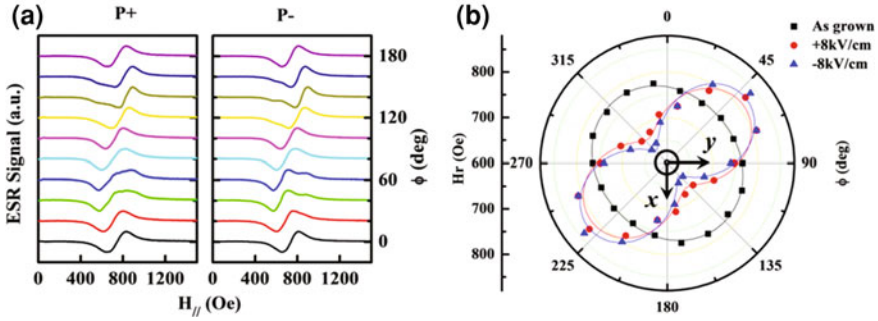


**Fig. 3.8** The **a** in-plane ESR signal and **b** polar plotting of the resonance magnetic field ( $H_r$ ) of the sample under different electric fields (Reprinted with permission from Ref. [21]. Copyright 2012 by American Physical Society)

### 3.3.2 Electric-Field Control of Magnetization

In order to directly investigate the electric-field control of magnetization in the CoFeB/PMN-PT structure, an integrated multiferroic measurement system based on SQUID was employed to measure the magnetization of the sample with in situ electric fields. According to the ESR measurement, the sample exhibits a uniaxial magnetic anisotropy state with the easy axis of magnetization along the  $[110]$  direction and hard axis along the  $[-110]$  direction. As a result, the investigations of electrical control of magnetization are mainly performed along the two special directions and the results along the  $[110]$  direction (easy axis) are shown in Fig. 3.9.

The magnetization-magnetic field (M-H) hysteresis loops were measured along the  $[110]$  direction under electric fields of 0,  $\pm 1$ , and  $\pm 8$  kV/cm, respectively, and the maximum change in magnetization occurs between  $+8$  and  $-8$  kV/cm as shown in Fig. 3.9a. It can be seen that the positive electric field tends to decrease the magnetization, while the negative electric field tends to increase it. This phenomenon is consistent with the ESR result as shown in Fig. 3.8b, in which the negative electric field results in a smaller resonance magnetic field than positive electric field along the  $[110]$  direction, implying that the negative electric field makes magnetizing process easy along the  $[110]$  direction.

Figure 3.9a also reveals that the converse ME effect is more remarkable at low magnetic fields. As a result, the direct magnetic response to electric field has been investigated via measuring magnetization of the sample along the  $[110]$  direction by cycling the electric field in the range of  $\pm 8$  kV/cm under a low magnetic field of 5 Oe. Meanwhile, the polarization current has also been recorded automatically by the ammeter in the circuit. The magnetization-electric field (M-E) curve is shown in Fig. 3.9b, which turns out to be a special *loop-like* behavior. From the M-E loop, one can see that the magnetization only changes slightly around  $600 \text{ emu/cm}^3$  for electric field sweeping from  $+8$  kV/cm to zero. As the electric field changes to negative and increases in magnitude gradually, a sharp increase in

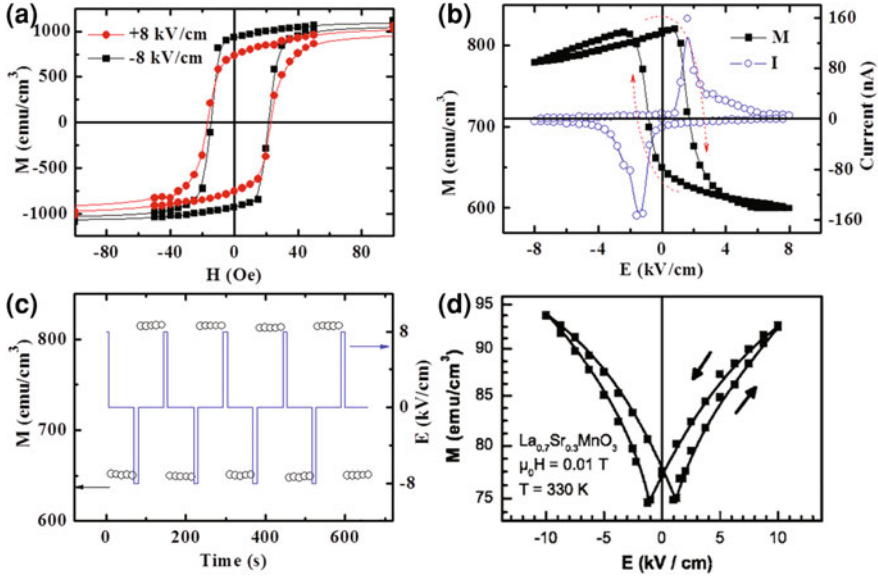


**Fig. 3.9** The results of electric-field control of magnetization along the  $[110]$  direction: **a** M-H loops under different electric fields, **b** *loop-like* (nonvolatile) M-E curve, **c** magnetization states tuned by pulsed electric fields, **d** *butterfly-like* (volatile) M-E curve (Reprinted with permission from Ref. [21]. Copyright 2012 by American Physical Society and figure (d) is adopted from the literature with permission from Ref. [3]. Copyright 2007 by American Physical Society)

magnetization occurs at about  $-2$  kV/cm as guided by the dashed arrow, which corresponds to the polarization switching process in PMN-PT as revealed by the polarization current peak in Fig. 3.9b. After that, the magnetization decreases a little around  $800$  emu/cm<sup>3</sup> during electric field changing from  $-2$  to  $-8$  kV/cm. For the case of electric field sweeping from  $-8$  to  $+8$  kV/cm, the magnetization first increases slowly and then switches back to the initial low magnetization state during the positive polarization switching process.

The M-E curve in our CoFeB/PMN-PT heterostructure is therefore clearly distinct from the previous results as commonly observed in the piezostain-mediated FM/FE structures, such as  $\text{La}_{0.67}\text{Sr}_{0.33}\text{MnO}_3$  [3] and  $\text{CoFe}_2\text{O}_4$  [7] grown on the same (001)-oriented PMN-PT substrate, or thick ferromagnetic alloy FeCoV layers bonded to (011)-oriented PZN-PT [6], all of which exhibit *butterfly-like* M-E curves as shown in Fig. 3.9d and the change of magnetization is volatile due to the piezostain vanish after removing the electric field. However, for the *loop-like* M-E curve as found in our experiment, the magnetization of CoFeB can be switched by bipolar electric fields and the electrical-modulated magnetization state can be maintained after removing the electric field, which is a kind of nonvolatile ME effect. Thereby, stable and remarkable high/low magnetization states can be switched from one to the other by pulsed electric fields with opposite polarities, as shown in Fig. 3.9c. In this regard, the large, switchable and nonvolatile converse

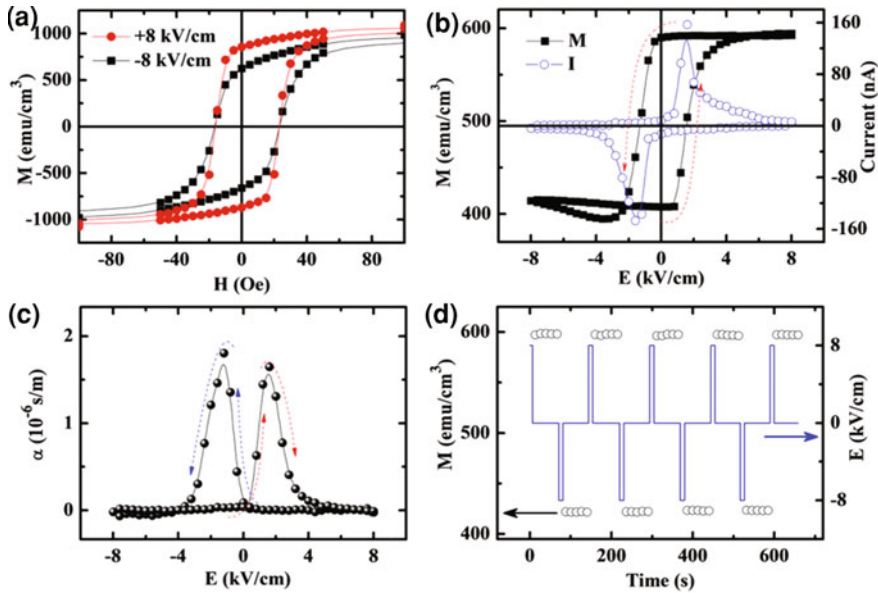


**Fig. 3.10** Results of electric-field control of magnetization along the  $[-110]$  direction: **a** M-H loops under different electric fields, **b** loop-like (nonvolatile) M-E curve, **c** deduced ME coupling coefficient, **d** magnetization states tuned by pulsed electric fields (Reprinted with permission from Ref. [21]. Copyright 2012 by American Physical Society)

ME effect reported here is particularly important in terms of room temperature applications involving electric-field control of magnetism and nonvolatile multiferroic memories.

Subsequently, similar measurements were carried out along the  $[-110]$  direction (i.e., the hard axis of magnetization) and all the results are shown in Fig. 3.10. Interestingly, comparing to the performances of electrical control of magnetization along the  $[110]$  direction (Fig. 3.9), we can see that all the M-H, M-E, and M-Time curves as shown in Fig. 3.1a-c along the  $[-110]$  direction exhibit reverse behaviors, in which positive electric field makes a large magnetization (about 600 emu/cm<sup>3</sup>) and negative electric field makes a small magnetization (about 400 emu/cm<sup>3</sup>). This phenomenon is consistent with the ESR result as shown in Fig. 3.8b, in which the positive electric field results in a smaller resonance magnetic field than negative electric field along the  $[-110]$  direction, implying that the positive electric field makes magnetizing process easy along the  $[-110]$  direction. Via careful comparison of the results along the  $[110]$  and  $[-110]$  directions, we can see the changed values of magnetization in M-H, M-E, and M-Time curves are almost the same (about 200 emu/cm<sup>3</sup>) and corresponding with each other, e.g., when a positive electric field switches the magnetization of the sample from 800 to 600 emu/cm<sup>3</sup> along the  $[110]$  direction, it also switches the magnetization from 400 to 600 emu/cm<sup>3</sup> along the  $[-110]$  direction, with the same amount of changed magnetization (200 emu/cm<sup>3</sup>). In this regard, the complementary behavior along

the two directions in magnetization as tuned by electric fields is inferred to be related with the magnetization rotation in plane, in which positive electric field will rotate the magnetization from the [110] direction to  $[-110]$  direction while negative electric field will do the contrary.

It is worth to mention that, according to the definition of magnetoelectric coupling coefficient:  $\alpha = \mu_0 dM/dE$  [15], the ME coupling coefficient  $\alpha$  can be derived by differentiating M-E curve in Fig. 3.10b and the maximum value reaches up to  $2 \times 10^{-6}$  s/m during the polarization switching process as shown in Fig. 3.10d, which is nearly one or two orders of magnitude larger than the previous reports [3, 7, 15]. By carefully comparing the M-E and I-E curves in Figs. 3.9b and 3.10b, we can see that the sharp changes of magnetization correspond to the current peaks induced by polarization reversal, which imply the mechanism for the nonvolatile converse ME effect is related to the polarization reversal effect in the PMN-PT substrate.

### 3.3.3 Electric-Field Control of Magnetic Domain

In order to further explore the behavior of nonvolatile electric-field control of magnetization at the microscopic scale, the evolution of magnetic domain structure in the sample under electrical stimulation has been investigated by magnetic force microscopy (MFM) with in situ electric field, which has been performed in a scanning probe microscope (SPM) system via collaboration with Prof. Ramesh's group in UC Berkeley and the results of electric-field control of magnetic domain as well as the corresponding macroscopic M-E and M-time curves are shown in Fig. 3.11.

The technique of observing the magnetic domain structure under in situ electric field is an advanced and important method in the area of multiferroic investigation, which can provide clear and direct experimental evidences and has been rarely reported [22, 23]. The key point in the MFM measurement with in situ electric field is that by proper designing the experiment, one can get rid of the influence of high electric field on the measurement system and eliminate other electrical interferences while detecting the signal of magnetic domain. Due to technical and secure limitations, the maximum electric field that can be applied onto the SPM system is about 4 kV/cm. As a result, the macroscopic investigation of electrical control of magnetization has firstly been performed with electric fields in the range of  $\pm 4$  kV/cm, and the results are shown in Fig. 3.11a and b. Since the change of magnetization mainly happens in the polarization reversal process and the electric field of 4 kV/cm is larger than the coercive field of PMN-PT, the *loop-like* M-E curve and nonvolatile ME effect can also be observed within the small range of electric fields, similar to the results under  $\pm 8$  kV/cm (see Fig. 3.10). Afterward, magnetic domain measurement of the sample with in situ electric fields was carried out, and MFM images corresponding to different magnetization states labeled "d" to "h" as shown in Fig. 3.11b were taken from the same region of the sample and the results are shown in Fig. 3.11d-h, respectively. To ensure the magnetic

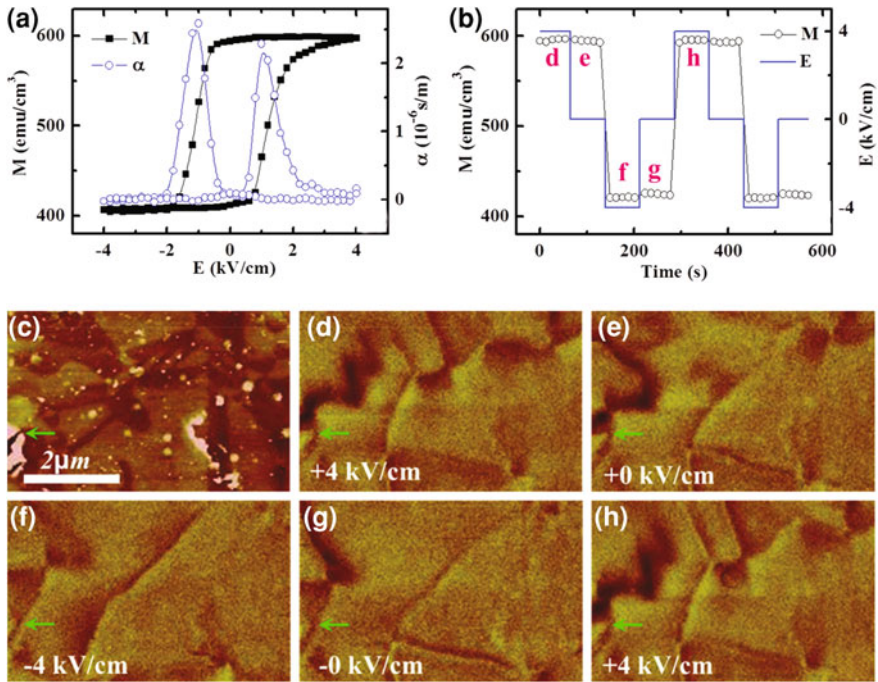


**Fig. 3.11** Macroscopic and microscopic investigation of electric-field control of magnetization: **a** M-E and  $\alpha$ -E curves, **b** M-Time curve, **c** Surface topography (AFM image), **d-h** Magnetic domain images (MFM phase)

domain images have been obtained from the same region, a high spot marked by a green arrow on AFM topography as shown in Fig. 3.11c was employed as a significant feature to align all the regions during the MFM measurement. From the figures, it can be seen that after removing the electric field of +4 kV/cm, both the magnetization and MFM image are comparable to those with application of +4 kV/cm, i.e., comparing state “e” with state “d” in Fig. 3.11b and comparing Fig. 3.11e with Fig. 3.11d, which indicates a nonvolatile behavior or memory effect both in magnetization and magnetic domain structure. Then, the sample is switched by a negative electric field of -4 kV/cm to a low magnetization state denoted by letter “f” as shown in Fig. 3.11b and the magnetic domain structure also shows a corresponding change as shown in Fig. 3.11f. Again, both the magnetization and the magnetic domain structure exhibit a nonvolatile behavior after removal of the negative electric field, i.e., comparing state “g” with state “f” in Fig. 3.11b and comparing Fig. 3.11g with Fig. 3.11f. Finally, the application of +4 kV/cm electric field switches the sample back to the high magnetization state denoted by letter “h” in Fig. 3.11b and the magnetic domain structure also shows a corresponding change as shown in Fig. 3.11h. The image is comparable to that in Fig. 3.11d, indicating the reversibility of electric-field control of both magnetization and magnetic domain structure.

Notably, we can see not all of the magnetic domains in the observed area will change along with the external electric fields, and some magnetic domains even do not change at all. This phenomenon indicates that the nonvolatile electrical control of magnetism originates from a certain local ME coupling in the microscopic scale, e.g., ferroelastic coupling between the magnetic domains and ferroelectric domains at the interface of the CoFeB/PMN-PT heterostructure, which should be a kind of new mechanism to be explored and different from the previous reports involving macroscopic piezostain-mediated ME coupling [3, 7].

## 3.4 Mechanism Investigation

### 3.4.1 *Eliminating Interfacial Charge Modulation and Current Effect*

Since the electric control of magnetization in the CoFeB/PMN-PT sample exhibits *loop-like* behavior similar to the ferroelectric hysteresis loop of PMN-PT, the most possible mechanism to be considered in this structure is the interfacial charge-mediated ME coupling effect as observed in the previous reports [24–27].

For the interfacial charge-mediated ME coupling effect, the FM materials employed in the FM/FE heterostructures are mainly thin films close to the insulator [24] or semiconductor [25] with low carrier concentration, in which it is easy for an external electric field to accumulate or deplete the spin-dependent carriers and thereby achieve remarkable electrical control of magnetization. However, for the metal film with good conductivity (such as Fe), it is hard to realize large charge-mediated ME coupling effect, because of the higher carrier concentration. Even at very high-electric field, only a few atomic layers of the iron film can be manipulated by electric field both in theory and experiment [26, 27]. According to reports, the resistivity of CoFeB we used here is about  $10^{-6} \Omega \cdot \text{m}$ , in which the effective screening length of electrons induced by electric field of 8 kV/cm is less than 1 Å. Since the thickness of the CoFeB film in our sample is 20 nm, the nonvolatile ME effect here can not be explained by the above scenario related to the electric field-induced charge accumulation/dissipation at the interface or a surface effect due to the polarization switching in the ferroelectric layer, because the contributions from these two scenarios are too small to account for the observed large change in magnetization which should originate from the variation of the whole film.

On the other hand, since the sharp changes of magnetization correspond to the current peaks as shown Figs. 3.9b and 3.10b, it is necessary to make sure that these changes are not related to the magnetic field produced by the polarization current. According to the equation  $I = dQ/dt = S \cdot cdP/dt$ , where the polarization charge  $Q$ , electrode area  $S$  and polarization  $P$  are constants for a certain ferroelectric sample, the polarization current  $I$  can be manipulated by changing the time of polarization reversal. Based on the circuit as shown in Fig. 3.2, in which the polarization current

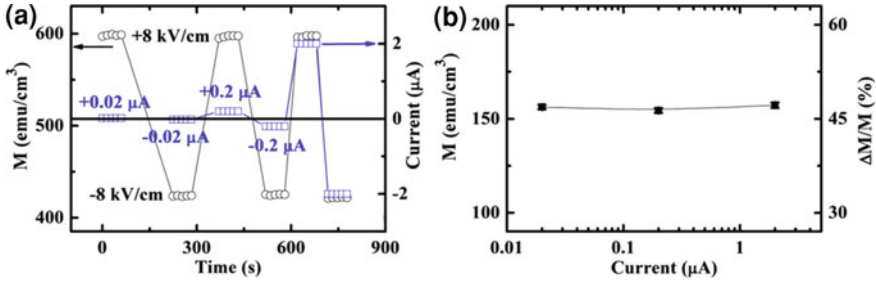


**Fig. 3.12** Eliminating the polarization current effect: **a** time evolution of magnetization and switching current, **b** variation of changed magnetization with switching current

can be observed simultaneously in the process of electric-field control of magnetization, an experiment was designed as manually changing the time of polarization reversal to get different maximum polarization currents, and the results are shown in Fig. 3.12. During the process of electric-field control of magnetization, the values of polarization currents with electric field switching between  $\pm 8$  kV/cm can be controlled as 0.02, 0.2 and 2  $\mu\text{A}$ , as shown in Fig. 3.12a. If the magnetization change of CoFeB film is controlled by the polarization current-induced magnetic fields, larger magnetization change will be achieved under larger polarization current. However, according to the experimental result as shown in Fig. 3.12b, despite the value of polarization current has changed three orders of magnitude, the magnetization change of CoFeB keeps almost the same ( $\Delta M \sim 150$  emu/cm<sup>3</sup>). As a result, the current effect can be ruled out and the mechanism in our system should owe to other factors related to polarization reversal in PMN-PT.

### 3.4.2 Characterization and Analysis of Ferroelectric Domain of PMN-PT

According to the previous experimental results and discussions in our system (see Sect. 3.3.3), the nonvolatile electric-field control of magnetization should originate from a certain kind of microscopic coupling effect related to polarization reversal (i.e., ferroelectric domain switching) in PMN-PT. As a result, piezoresponse force microscopy (PFM) was employed to investigate the ferroelectric domain structure of PMN-PT, especially during the polarization reversal process.

The composition of PMN-PT that we used here is in the region of the morphotropic phase boundary (MPB) [16], which possess not only a ultrahigh piezoelectric response but also complicated phase structures and ferroelectric domains [17]. One of the major structures of PMN-PT is the rhombohedral (R) phase with spontaneous ferroelectric polarizations along  $\langle 111 \rangle$  directions (the body diagonals of the pseudo-cubic unit cell) at room temperature as in rhombohedral BiFeO<sub>3</sub>, and there are eight equivalent polarization directions, which can

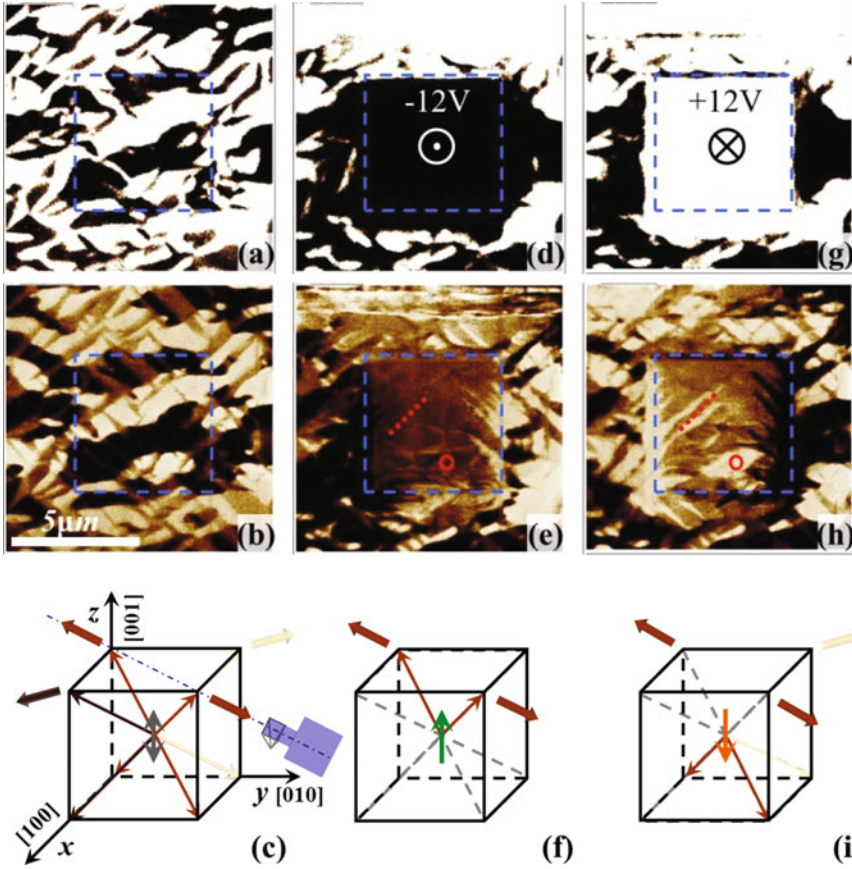
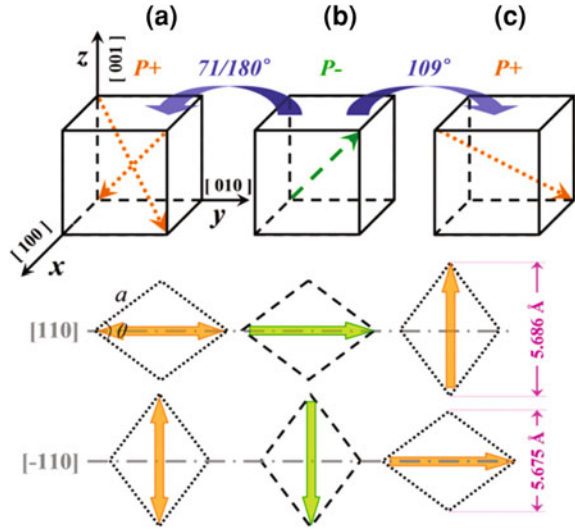


**Fig. 3.13** PFM phase images of different polarization states taken with the cantilever along the PMN-PT's pseudocubic  $[110]$  direction. (a) (d) (g) out-of-plane PFM images (b) (e) (h) in-plane PFM images (c) (f) (i) configurations of polarization vector under different voltages (Reprinted with permission from Ref. [21]. Copyright 2012 by American Physical Society)

be switched by  $71$ ,  $109$  and  $180^\circ$ , respectively [28]. As a result, similar analysis method [29] was used to investigate the ferroelectric domain state and polarization switching in the PMN-PT substrate. A Veeco Multimode<sup>TM</sup> 8 SPM system was employed to investigate the ferroelectric domain structure at ambient conditions with the cantilever along the  $[110]$  direction and a driving AC voltage of  $2.0 V_{PP}$  at  $45$  kHz applied onto the sample via conductive DDESP-10 tip. The domain structures as well as the corresponding configurations of polarization vectors of PMN-PT with unpoled, positive poled, and negative poled states as revealed by PFM are shown in Fig. 3.13.

From the PFM results, we can see that the out-of-plane phase images in Fig. 3.13a, d, and g have two kinds of colors in contrast, i.e., black and white, which represent the out-of-plane polarization components pointing up and down, respectively. As for the

**Fig. 3.14** The polarizations and lattice distortions induced by different kinds of ferroelectric domains switching. (b) to (a): 71 or 180° switching, (b) to (c): 109° switching (Reprinted with permission from Ref. [21]. Copyright 2012 by American Physical Society)



in-plane phase images in Fig. 3.13b, e, and h, there are three kinds of colors in contrast, i.e., black, white, and brown, which represent the in-plane polarization components pointing left, right, and along the cantilever (i.e., the  $[110]$  and  $[-1-10]$  directions in our case), respectively. Figure 3.13a and b are the PFM images of the unpoled PMN-PT for the out-of-plane and in-plane cases, respectively. Based on the piezoresponse analyzing principle [29], the polarization directions can be deduced as shown in Fig. 3.13c, which agrees with the nature of the rhombohedral structure. After poling a  $5\ \mu\text{m}$  by  $5\ \mu\text{m}$  square in the center of a  $10\ \mu\text{m}$  by  $10\ \mu\text{m}$  visual field with a  $-12\ \text{V}$  dc voltage biased on the tip, the color of the out-of-plane image becomes black in the poled area and the color of the in-plane one changes to brown as shown in Fig. 3.13d and e, respectively, which means that all the out-of-plane polarization components are switched upward in the poled area and the in-plane ones only have two possible orientations along the  $[110]$  direction as shown in Fig. 3.13f. In the case of  $+12\ \text{V}$  bias voltage poling, the out-of-plane image becomes white as shown in Fig. 3.13g, representing the out-of-plane polarization components switched downward as shown in Fig. 3.13i, while for the in-plane image shown in Fig. 3.13h some white regions appear inside the brown area. We can deduce the in-plane polarization directions as shown in Fig. 3.13i. Therefore, the white regions as denoted by red-dashed line and circle in Fig. 3.13e and h correspond to  $109^\circ$  switching (ferroelastic switching [30]), while the other brown regions are related to  $71$  or  $180^\circ$  switching.

Based on the above experimental results as observed in the PFM investigation, a brief model has been proposed to explain the special ME coupling effect and electric-field control of magnetization, as shown in Fig. 3.14.

In the unit cell of PMN-PT single crystal with rhombohedral phase, its spontaneous polarizations point along the  $\langle 111 \rangle$  directions (i.e., the diagonals of the cubic unit cell) and the lattice perimeter is slightly elongated along the polarization

direction, which makes the unit cell of PMN-PT to be a “pseudo-cubic” structure. Under the rhombohedral distortion in the pseudo-cubic unit cell, the projections of the  $\langle 111 \rangle$  polarization vectors on the (001) plane lie along the pseudo-cubic  $\langle 110 \rangle$  directions, transforming the square (001) plane of the cubic unit cell to a rhombic shape. According to the lattice parameters of the rhombohedral distortion reported in the literature [18], the long and short diagonals of the rhomb parallel and perpendicular to the in-plane projection of polarization was calculated to be 5.686 and 5.675 Å, respectively, as shown in Fig. 3.14.

Based on this model, the aforementioned results can be understood as follows. Without poling, the virgin states of polarizations as well as ferroelectric domains are randomly oriented along the eight possible  $\langle 111 \rangle$  directions, resulting in the random orientation of the in-plane rhombohedral distortions. As a result, the as-grown CoFeB thin film on the unpoled PMN-PT substrate exhibits an in-plane magnetic isotropy as shown in Fig. 3.8b, due to its amorphous nature and the randomness of in-plane rhombohedral distortions. After negative poling, most of the ferroelectric domains align in the [110] direction as shown in Fig. 3.13f to reduce the ferroelastic energy [21], leading to a longer distortion along the [110] direction as shown in Fig. 3.14b, which induces the uniaxial magnetic anisotropy in CoFeB films with the easy direction of magnetization along [110] and hard direction along  $[-110]$  as shown in Fig. 3.8(b). For the positive poling, some ferroelectric domains switch by  $109^\circ$  while others switch by  $71^\circ$  or  $180^\circ$  as shown in Fig. 3.13i and also Fig. 3.14. When the  $71^\circ$  or  $180^\circ$  ferroelectric domain switchings occur in the PMN-PT sample, the in-plane rhombohedral distortions do not change their directions, as shown in Fig. 3.14a and b. Thereby, the elongated direction of the local strain still lies along the [110] direction and the local uniaxial magnetic anisotropy of CoFeB film remains unchanged. In contrast to the  $71^\circ$  or  $180^\circ$  switchings, the  $109^\circ$  switching changes the elongated distortions from the [110] direction for negative poling to the  $[-110]$  direction for positive poling as shown in Fig. 3.14b and c, leading to the local easy axis of magnetization in CoFeB film turning to the  $[-110]$  direction. However, the number of ferroelectric domains with  $109^\circ$  switching is not large enough to change the direction of magnetic easy axis of the whole sample, and the effect of  $109^\circ$  switchings only result in a weaker uniaxial anisotropy at positive electric field comparing to the negative electric field, as shown in Fig. 3.8b. It should be emphasized that the  $109^\circ$  domain switching is essentially a kind of ferroelastic switching [30], which also produces strain effect. However, different from the macroscopic strain generated by converse piezoelectric effect, the ferroelastic strain generated by  $109^\circ$  switching will retain its value after removing the electric field due to the maintenance of ferroelectric domain as well as polarization orientation, which is responsible for the nonvolatile electrical control of magnetization as observed in our investigation. When the external electric field exceeds the ferroelectric coercive field of the PMN-PT substrate, the ferroelastic strain will change its value accompanying with the  $109^\circ$  ferroelectric switching, leading to complementary strain along the [110] and  $[-110]$  directions and *loop-like* M-E curves with the complementary behavior for the [110] and  $[-110]$  directions as shown in Figs. 3.9b and 3.10b.

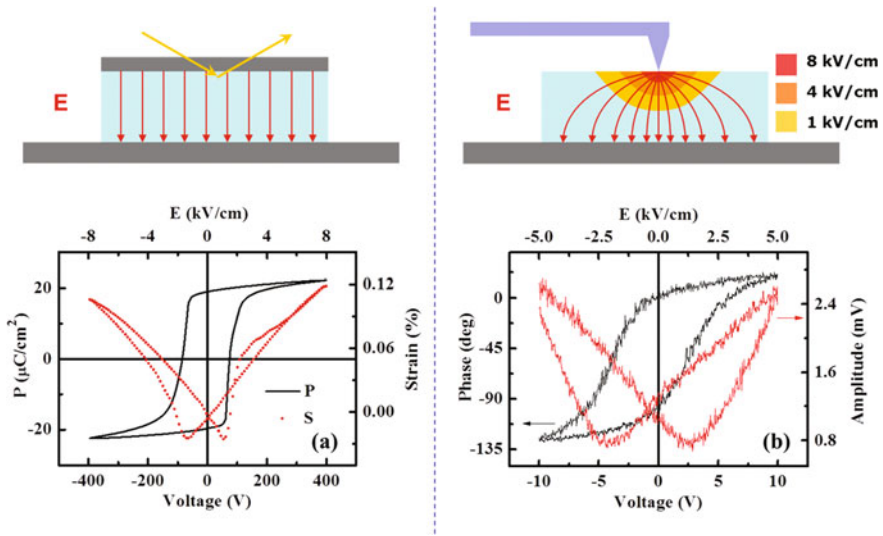


**Fig. 3.15** The difference between **a** electrode poling and **b** tip poling

Notably, the PFM is a kind of probe-based local detection method, and the results that have been measured can not fully reflect the electrical response of the whole sample with a large-area electrode. One important difference is that the electric field applied on the tip has a steep gradient with ultra-high electric field near the tip, while the electric field applied by a large-area electrode is very uniform, as shown in Fig. 3.15. In the P-E loop and S-E curve measurements with a large-area electrode, electric voltages above 100 V are needed for the 0.5 mm thick sample in order to exceed the coercive field of PMN-PT (about 2 kV/cm) as shown in Fig. 3.15a. However, for the equivalent measurements of the sample with the same thickness via the PFM tip, electric voltages below 5 V are sufficient for achieving 2 kV/cm equivalent electric field, switching the polarization of PMN-PT and producing similar ferroelectric and piezoelectric responses, as shown in Fig. 3.15b. Comparing the two figures in Fig. 3.15, we can see that the intensity of equivalent electric field decreases rapidly away from the tip. Thereby, the tip-induced electric field can only switch the ferroelectric domains within a thin layer of the sample surface near the tip rather than throughout the whole sample. Besides, PFM is mainly a kind of qualitative investigation method with the powerful ability of directly observing the ferroelectric domains. Other quantitative analysis methods with conditions comparable to the ME coupling experiments ought to be developed for our sample, in order to further understand the phenomenon of nonvolatile electric-field control of magnetization.

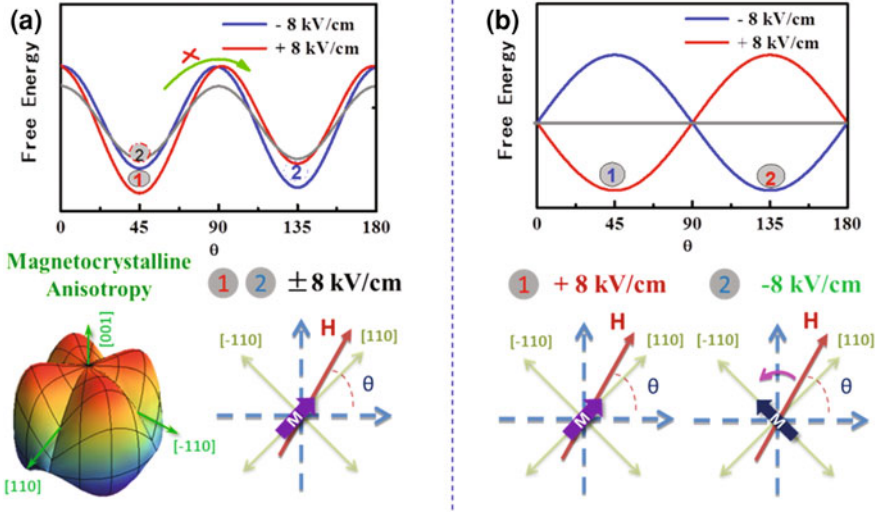


**Fig. 3.16** Different magnetic response to  $109^\circ$  domain switching: **a** epitaxial film with strong magnetic anisotropy, **b** amorphous film without magnetic anisotropy

### 3.4.3 Magnetic Response of $\text{CoFeB}$ to $109^\circ$ Ferroelectric Domain Switching

According to the analysis in the last section, the  $109^\circ$  ferroelectric domain switching in PMN-PT which induces complementary rhombohedral distortions along the  $[110]$  and  $[-110]$  directions in plane, is the main reason for the nonvolatile electrical control of magnetization. However, it is worth to mention that in our previous work [7], PMN-PT substrates with the same composition and orientation as we used in this thesis have been employed in the  $\text{CoFe}_2\text{O}_4/\text{PMN-PT}$  heterostructures while the result of electrical control of magnetization exhibits commonly observed *butterfly-like* behavior instead of *loop-like* nonvolatile ME coupling as observed here. The main difference between the two multiferroic structures is that the FM layer which exhibits *butterfly-like* M-E curve is epitaxial  $\text{CoFe}_2\text{O}_4$  thin film with strong magnetocrystalline anisotropy and the FM layer which exhibits *loop-like* M-E curve is amorphous  $\text{CoFeB}$  film without magnetocrystalline anisotropy. The difference in magnetic anisotropy of the two kinds of materials results in different response to the  $109^\circ$  ferroelectric domain switching, as shown in Fig. 3.16.

From Fig. 3.8b, one can see the difference in magnetic anisotropy fields induced by positive and negative electric fields has an equivalent value of about 20 Oe. Comparing to the coercive field of  $\text{CoFe}_2\text{O}_4$ , 20 Oe magnetic field is too small to overcome the magnetocrystalline anisotropy field when magnetization vectors are rotating between different directions. Therefore, the response of magnetization to the ferroelastic strain related to the  $109^\circ$  domain switching has

been suppressed, resulting in the *butterfly-like* M-E curve with a much smaller change in magnetization, as shown in Fig. 3.16a. However, due to the absence of magnetocrystalline anisotropy in amorphous CoFeB film, the magnetic field with equivalent value of 20 Oe induced by  $109^\circ$  domain switching is large enough for the magnetic vectors of amorphous CoFeB to achieve a  $90^\circ$  rotation in plane and results in the *loop-like* M-E curve with a much larger change in magnetization, as shown in Fig. 3.16b. Similar switchable and nonvolatile electric-field control of magnetization, as reported here, should be expected for FM/FE structures consisting of nonepitaxial FM layers with weak or no magnetocrystalline anisotropy and FEs with  $109^\circ$  ferroelastic switching.

### 3.4.4 Quantitative Analysis Based on XRD-RSM

In the previous sections, we have qualitatively investigated the mechanism for the nonvolatile electrical control of magnetization by PFM method with explicit experimental evidence. To further quantitatively investigate the ME coupling effect with information about the change of crystal structure and lattice parameters accompanying the ferroelectric domain switching in PMN-PT, other quantitative analysis methods ought to be employed with in situ electric fields. The X-ray diffraction (XRD) analysis techniques (including reciprocal space mapping, RSM [31]) under in situ electric field are newly developed measurement methods recently, which are powerful tools for the quantitative investigation of piezostain in crystal lattice [32] and ferroelectric domain structure [30]. By collaboration with Prof. Gao's group in University of Science and Technology of China, the synchrotron radiation high-resolution XRD-RSM method with in situ electric field was employed for the quantitative investigation of the rhombohedral distortion and ferroelastic strain in lattice related to the ferroelectric domain switching in the samples.

The configuration as well as the sample structure for the XRD-RSM measurement under in situ electric fields is shown in Fig. 3.2, in which the electric field is applied by external electric circuit and high intensity X-Ray is supplied by synchrotron radiation light source. Since the CoFeB film on top of the sample has an amorphous structure, no diffraction peaks of CoFeB will be observed in the XRD pattern. Although the Au layer has a polycrystalline structure, its diffraction intensity is much smaller than that of PMN-PT single crystal substrate. Besides, only specific diffraction peaks of PMN-PT such as (002), (103), and (113) were selected by the  $\omega$ - $2\theta$  linkage scanning in RSM, which effectually eliminate the interference of Au layer in the diffraction. On the other hand, the area of X-Ray spot is slightly larger than the sample size in plane. As a result, crystal information of the entire sample surface can be gathered by XRD, which will be helpful for the following quantitative analysis based on the XRD data and comparison with the ME results. For ferroelectric materials with rhombohedral structures, the (113) reflection is often chosen in RSM measurements to determine the four kinds of distortions and the eight equivalent polarizations [30]. With the in-plane reciprocal

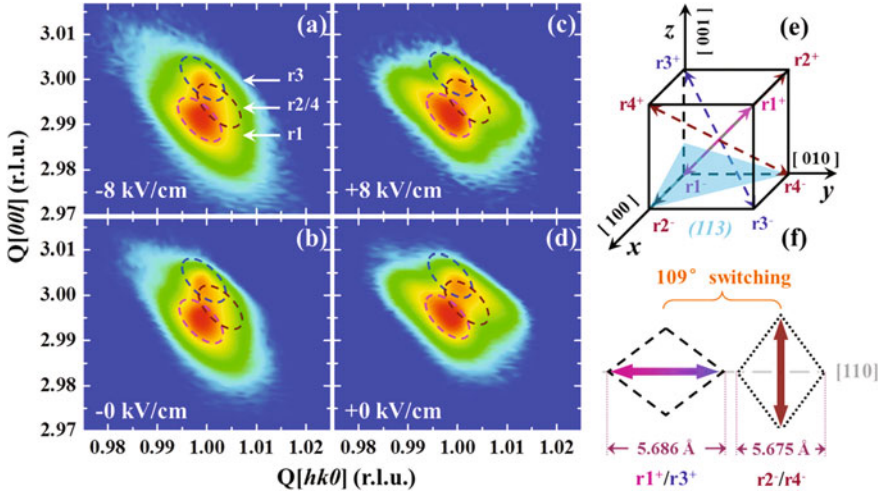


**Fig. 3.17** The **a–d** RSM images around the (113) reflection of PMN-PT at different electric fields and **e–f** the corresponding rhombohedral distortions (Reprinted with permission from Ref. [21]. Copyright 2012 by American Physical Society)

vector component  $Q_x$  defined along the  $[110]$  direction, XRD-RSMs around the (113) reflections have been measured under different electric fields and four of the key results as well as the crystal structures are presented in Fig. 3.17.

The reflections around the (113) peak under electric fields of  $-8$  kV/cm,  $-0$  kV/cm (i.e., after removing the negative electric field),  $+8$  kV/cm,  $+0$  kV/cm (i.e., after removing the positive electric field) are shown in Fig. 3.17a–d, respectively. Interestingly, the overall features of the reflections are almost unchanged after removing the electric fields, e.g., comparing Fig. 3.17a with Fig. 3.17b and comparing Fig. 3.17c with Fig. 3.17d, while they show a remarkable difference for the positively and negatively poled cases, e.g., comparing Fig. 3.17a with Fig. 3.17c and comparing Fig. 3.17b with Fig. 3.17d. This behavior is consistent with the nonvolatile electric-field control of magnetization as shown in Figs 3.9 as well as 3.10, and also agrees with the investigation of magnetic domain variation under electric fields as shown in Fig. 3.11. These correlations and consistencies in magnetization, magnetic domain and ferroelectric domain further reveal the ferroelectric domain switching-related mechanism of the nonvolatile ME coupling effect. Besides, the XRD method with the ability of accurate and quantitative analysis of the crystal lattice enables us to quantify the mechanism for the nonvolatile electric control of magnetization.

Based on the basic principle of XRD-RSM [31] and the reported rhombohedral crystal structure of PMN-PT [16], the pseudo-cubic unit cell of PMN-PT with the four kinds of distortions (i.e.,  $r1$ ,  $r2$ ,  $r3$ , and  $r4$ ) as well as the eight equivalent polarization directions (i.e.,  $r1^\pm$ ,  $r2^\pm$ ,  $r3^\pm$  and  $r4^\pm$ ) are shown in Fig. 3.17e, in which the (113) crystal face is also indicated by a translucent blue plane. For the

**Table 3.1** The calculated positions of diffraction spots in RSM around the (113) reflection for each kind of rhombohedral distortion and the corresponding polarization of PMN-PT

Angle	Indices of crystal			Distortion	Polarization	$Q_{[001]}$	$Q_{[110]}$
	$h$	$k$	$l$				
89.8(9)°	1	1	3	r1	$r1^+$ , $r1^-$	2.996(2)	0.999(0)
				r2 /r4	$r2^+$ , $r2^-$ / $r4^+$ , $r4^-$	3.000(0)	1.001(0)
				r3	$r3^+$ , $r3^-$	3.003(8)	0.999(0)

Numbers in brackets are not accurate because of the error (Reprinted with permission from Ref. [21]. Copyright 2012 by American Physical Society)

rhombohedral phase, the projections of the  $\langle 111 \rangle$  polarization vectors on the (001) plane lie along the pseudo-cubic  $\langle 110 \rangle$  axes, transforming the square (001) plane of the cubic unit cell to a rhombic shape. According to the lattice parameters of the rhombohedral distortion as reported [18], the diagonals of the rhomb parallel and perpendicular to the in-plane projection of polarization was calculated to be 5.686 and 5.675 Å for 109° switching as shown in Fig. 3.17f. Besides, the theoretical positions of diffraction spots corresponding to all the possible rhombohedral distortions as well as polarizations in the (113) reflection have been calculated and the detailed coordinates of diffraction spots corresponding to different rhombohedral distortions are listed in Table 3.1 as following.

According to the theoretical coordinate in Table 3.1 and consideration of the kinetic elongated effect of (113) diffraction spot in the  $\omega$ -2 $\theta$  linkage scan [33], the diffraction spots corresponding to different types of rhombohedral distortions are marked by twisted ellipses in the RSMs as shown in Fig. 3.17a–d. Besides, the positions of the deduced spots at electric field of  $\pm 8$  kV/cm are accordingly shifted along the  $Q_{[001]}$  axis, due to the piezostain effect along the [001] direction. To compare the theoretical results with the experimental data, two-dimensional Gauss fittings of the RSM results were performed. Figure 3.18 shows the result of fitted (113) diffraction under negative polarization, in which the raw RSM data is denoted by continuous colored 3D surface with black mesh and the fitted data is denoted by gray envelope grid.

Using the two-dimensional Gauss fitting method as mentioned above, the RSM data in Fig. 3.17a–d were quantitatively fitted with the deduced spots in Table 3.1 to figure out the percentages of the four kinds of distinct distortions for the positively and negatively poled cases, respectively, and the results are listed in Table 3.2, in which the correlation coefficients for each cases are also included. In Table 3.2, we can see that the polarization vectors are mainly  $r1^+$  and  $r3^+$  under negative electric fields, and the quantity of polarizations  $r2^+/r4^+$  is small (about 4 %). Under positive electric field, although the polarizations of  $r1^-$  and  $r3^-$  are still dominant, the polarizations of  $r4^-/r2^-$  have also occupied a considerable number (about 30 %). These results agree with the PFM characterization as shown in Fig. 3.13 and also coincide with the macroscopic magnetic characterization in the previous sections.

From the corresponding of polarizations and rhombohedral distortions, we can deduce the switching category from the changes between different rhombohedral

**Fig. 3.18** Raw data and 2D Gauss fitting of the RSM around the (113) reflection

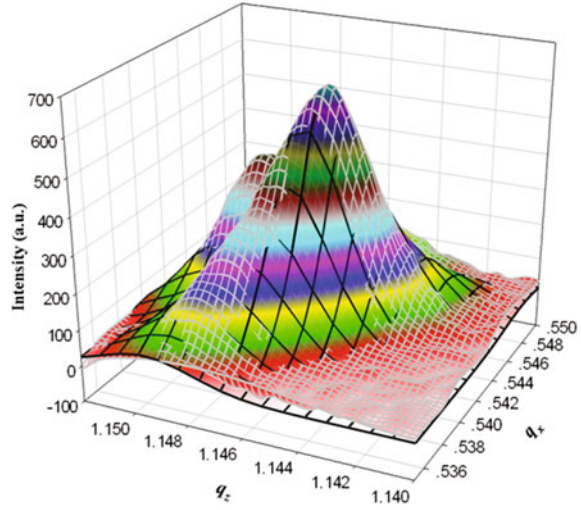


**Table 3.2** Percentages of the four rhombohedral distortions under different electric fields

Distortion category		-8 kV/cm	-0 kV/cm	+8 kV/cm	+0 kV/cm
Percentage	r1	79 ± 1 %	78 ± 1 %	56 ± 1 %	60 ± 1 %
	r2/r4	4 ± 1 %	4 ± 1 %	32 ± 1 %	30 ± 1 %
	r3	17 ± 1 %	18 ± 1 %	12 ± 1 %	10 ± 1 %
Correlation coefficient		0.95	0.96	0.94	0.93

(Reprinted with permission from Ref. [21]. Copyright 2012 by American Physical Society)

distortions as follows. Distortions changing from  $r1^+/r3^+$  to  $r2^-/r4^-$  or  $r2^+/r4^+$  to  $r1^-/r3^-$  (vice versa) correspond to the  $109^\circ$  switching, distortions changing from  $r1^+$  to  $r3^-$  or  $r3^+$  to  $r1^-$  (or the same case with  $r2$  to  $r4$ , vice versa) correspond to the  $71^\circ$  switching, and distortions without any changes (e.g.,  $r1^+$  to  $r1^-$  and so on) correspond to the  $180^\circ$  switching. Since the change between  $r1/r3$  and  $r2/r4$  corresponds to the  $109^\circ$  switching, therefore, the ratio of  $109^\circ$  switching is about 26 % (because the percentage of  $r2/r4$  between the negatively and positively poled cases changes from about 4–30 %) and the  $71/180^\circ$  switchings share the balance of 74 %. On the other hand, the change of magnetization is about  $200 \text{ emu/cm}^3$  as shown in the M-E curves in Figs. 3.9b and 3.10b, and the remnant magnetization is about  $800 \text{ emu/cm}^3$  as shown in Figs. 3.9a and 3.10a. Therefore, the relative change of magnetization ( $200/800 = 25 \%$ ) and the percentage of  $109^\circ$  switching (26 %) are quantitatively comparable, suggesting that the change of magnetization is closely related to  $109^\circ$  switching.

Since the XRD method has the ability of accurate and quantitative analysis of the lattice perimeters of materials, the lattice parameters of the PMN-PT single crystal substrate along the [110] direction can be deduced from the RSM results for the in-plane reciprocal vector components of reflections around the (113) peak are parallel

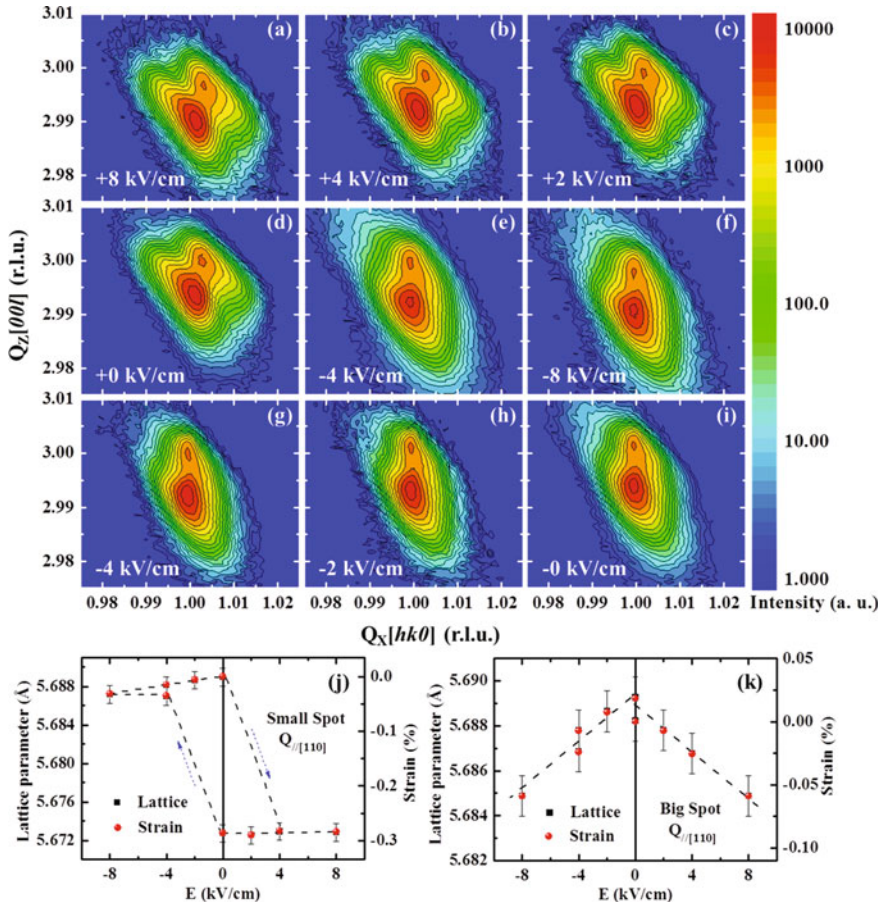


**Fig. 3.19** All the (113) reflections under different electric fields (from **a** +8 kV/cm to **i** -0 kV/cm) and the quantify analysis of lattice strain for the **j** small spot ( $109^\circ$  switching contribution) and **k** big spot ( $71/180^\circ$  switchings contribution) (Reprinted with permission from Ref. [21]. Copyright 2012 by American Physical Society)

to the [110] direction. All the (113) reflections under a series of electric fields: from +8 to -8 kV/cm and back to 0 kV/cm together with variations of the deduced lattice parameters along the [110] direction with external electric fields are shown in Fig. 3.19, in which two spots are present in the RSM images and the position of the small one changes remarkably with electric fields. The lattice parameters along the [110] direction deduced from the obviously changed small spot are about 5.688 and 5.673 Å for the negatively and positively poled cases, respectively, which are consistent with the calculated results (i.e., 5.686 and 5.675 Å) based on  $109^\circ$  domain switching (PFM observation)-induced distortion as shown in Fig. 3.17f. Variation of the small spot with electric field was obtained with detailed quantitative analysis of all the RSMs around the (113) reflection as shown in Fig. 3.19a-i,

and the electric field tuned lattice parameter and corresponding strain along the [110] direction exhibits a giant *loop-like* behavior (ferroelastic strain) as shown in Fig. 3.19j, consistent with the M-E curves as shown in Fig. 3.9b. Quantitative analysis of the position of the other big one in the (113) reflection is shown in Fig. 3.19k, which reveals the electric field-tuned lattice parameter and corresponding strain along the [110] direction related to 71/180° domain switching. The strain deduced from the big spot is much smaller than that deduced from the small spot and is volatile.

Finally, it should be mentioned that the *loop-like* M-E curve is not a standard “loop” but appears like a “butterfly” curve that is biased to one side, and the reason can be understood as follows. As we discussed in the previous section, the 109° switching changes the elongated distortions from the [110] direction to the [−110] direction, resulting in complementary ferroelastic strains along the two directions with a *loop-like* behavior, which accounts for the important nonvolatile ME effect. However, that is not the whole story. Since the PMN-PT has large strain effect, it surely has some contribution to the volatile ME (*butterfly-like*) effect. As one can see from Fig. 3.19j and k, both of the 109° switching-induced *loop-like* behavior and the 71/180° switching-induced *butterfly-like* behavior can be observed, and the maximum strains are about 0.2 and 0.07 %, respectively. We have simulated the normal *butterfly-like* curve as shown in Fig. 3.20a and the novel *loop-like* 109° curve as shown in Fig. 3.20b. After linear superposition of the two simulated S-E curves with a ratio of 1/3, we can get the final S-E curve as shown Fig. 3.20c, which is similar to the experimental M-E curve as shown in Fig. 3.20d. Therefore, it is reasonable that the M-E curve is neither a standard hysteresis shape nor a standard butterfly shape. Thus we cannot simply consider the M-E curve comes from the normal *butterfly* curve that is biased. Or in other words, the reason for the “bias” of *butterfly* curve is the 109° switching-induced *loop-like* nonvolatile ME effect.

### 3.4.5 Further Inference and Validation Based on the Mechanism

According to the previous discussion, the 109° ferroelectric domain switching in rhombohedral phase is important for the nonvolatile electric control of magnetization. Thereby, the phase structure of ferroelectric substrates will influence the behavior of electric control of magnetization. As one can see from the phase diagram of PMN-PT in Fig. 3.1b, the ferroelectric phase and crystal structure of PMN-PT will change with the components and temperature, e.g., PMN-28 %PT will exhibit typical rhombohedral phase and PMN-35 %PT and will exhibit typical tetragonal phase at room temperature. Thereby, these two kinds of PMN-PT substrates are employed in the CoFeB/PMN-PT heterostructure to further investigate the electrical control of magnetization, and the results are shown in Fig. 3.21.

The virgin ferroelectric domain structures of the two PMN-PT substrates have been characterized by PFM. The domain pattern of the rhombohedral phase in

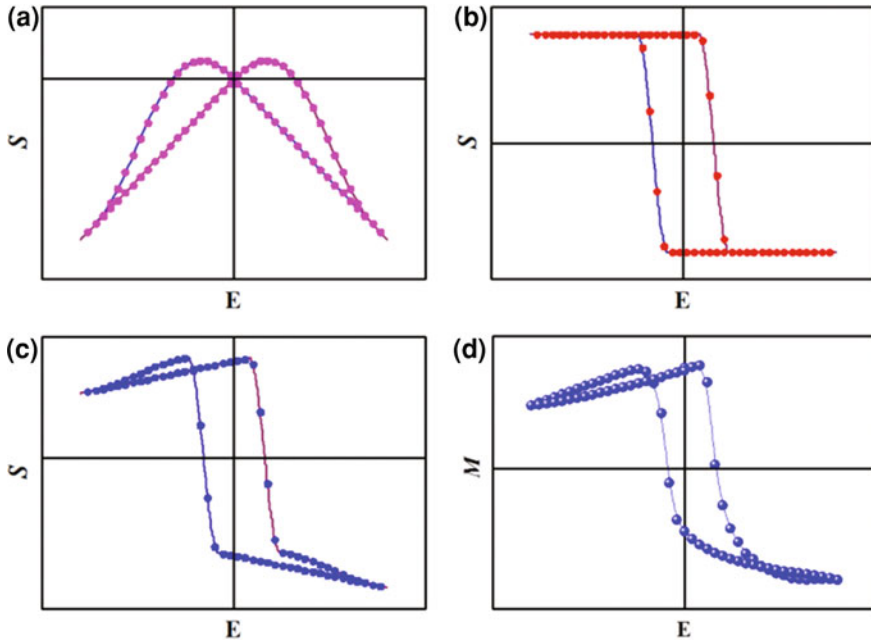


**Fig. 3.20** Simulated S-E curves along the [110] direction: **a** Normal *butterfly-like* S-E curve. **b** 109° switching-induced *loop-like* S-E curve. **c** Superposition of the S-E curves in (a) and (b) with a ratio of 1/3. **d** Experimental M-E curve along the [110] direction (the same data as Fig. 3.9b in the thesis)

PMN-28 %PT exhibits a relatively complicated zigzag structure as shown in Fig. 3.21a, and the domain pattern of the tetragonal phase in PMN-35 %PT exhibits a relatively simple strip-like structure as shown in Fig. 3.21b. The out-of-plane lattice parameters of the two PMN-PT substrates have also been characterized by XRD with  $\theta$ - $2\theta$  scan mode and the results are shown in Fig. 3.21c. Since the rhombohedral distortion induced by the spontaneous polarization of PMN-28 %PT is along the  $\langle 111 \rangle$  directions of the pseudo cubic structure, the lattice parameters of the four kinds of rhombohedral distortions along the [001] direction are the same. As a result, the (002) diffraction peak of the PMN-28 %PT sample exhibits unimodal distribution, shown as the blue line in Fig. 3.21c. In contrast, the lattice parameter of the tetragonal distortion with polarization along the [001] direction (also the [00-1] direction) is different from the case of tetragonal distortion with polarization along the [100] direction (also the  $[-100]$ , [010] and [0-10] directions), for which the (002) diffraction peak splits into bimodal distribution shown as the red line in Fig. 3.21c. After preparing ferromagnetic CoFeB film on top of the two kinds of PMN-PT substrates and taking the M-E measurements, we found that the sample with PMN-28 %PT exhibited nonvolatile *loop-like* behavior in M-E curve while the sample with PMN-35 %PT exhibited volatile *butterfly-like* behavior in M-E curve as shown in Fig. 3.21d. This

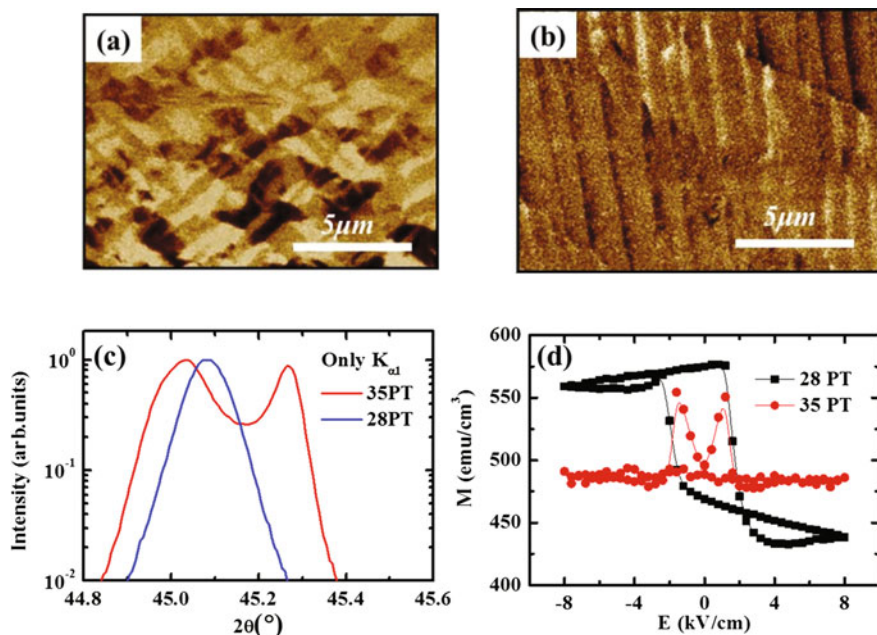


**Fig. 3.21** The a–b ferroelectric domains, c XRD patterns and d ME curves of different samples grown on a PMN-28PT and b PMN-35PT, respectively



**Fig. 3.22** The mechanism summary of the nonvolatile electrical control of magnetization

result is consistent with our expectation and can be understood as follows. In the rhombohedral phase of PMN-PT, there are 109° domain switchings which lead to the *loop-like* M-E curve. However, in the tetragonal phase of PMN-PT, the 109° domain switchings do not exist which result in the *butterfly-like* M-E curve.

In conclusion, the mechanism for the large, tunable and nonvolatile electric-field control of magnetization in CoFeB/PMN-PT at room temperature can be understood as the direct coupling between FE domain and FM film with the combined action of 109° ferroelastic domain switching in PMN-PT and the absence of magnetocrystalline anisotropy in CoFeB film, as shown in Fig. 3.22. This work is significant for exploring novel mechanisms in electric-field control of magnetism and relevant applications.

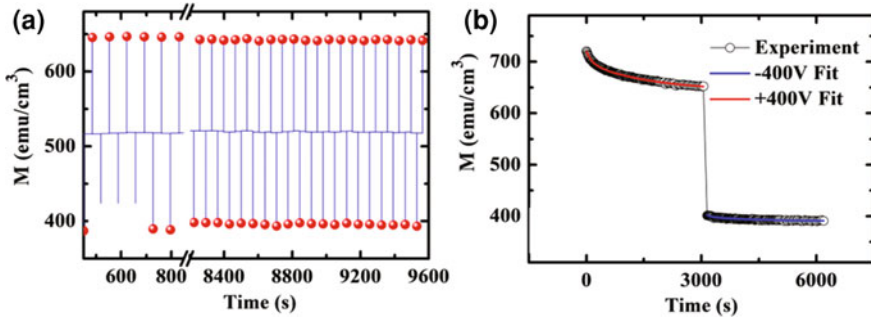


**Fig. 3.23** Investigation of the **a** fatigue and **b** retention properties of the ME effect (Reprinted with permission from Ref. [21]. Copyright 2012 by American Physical Society)

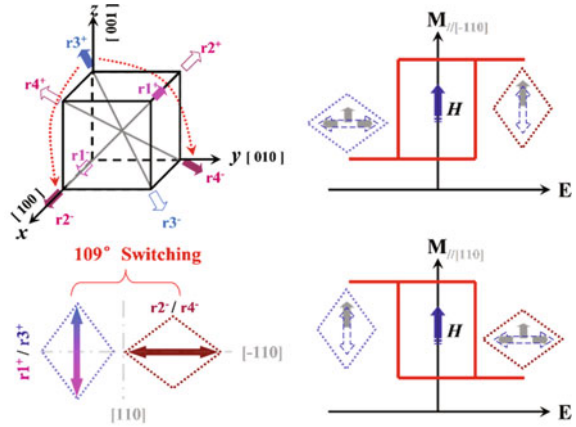
### 3.5 Characterization of Properties Related to Application Requirements

Since the main aim for the electric-field control of magnetization is providing room temperature applications related to the new generation information storage technology with high-integration density and low-power consumption, it is important to characterize the properties related to application requirements at room temperature. As a result, experiments related to fatigue and retention properties of the ME coupling effect was performed and electric-field control of magnetization reversal was also realized with the assistance of magnetic field as following.

#### 3.5.1 Characterization of Fatigue and Retention Properties of the Sample

Considering the requirements of application, the fatigue and retention properties of the ME effect have also been investigated. The magnetization of the sample was switched by electric fields for thousands of times, and as far as we have tested, the ME effect was repeatable as shown in Fig. 3.23a. We also continuously measured the magnetization for hours after positive and negative electric field pulses and the magnetization was almost unchanged, excepting a minor relaxation as shown in Fig. 3.23b. Fitting the magnetization relaxation curve, we can deduce the time that the magnetic state can be maintained is more than 10 years. These results further demonstrated that the electric-field-controlled magnetization is tunable and non-volatile, which is practical for applications.

**Fig. 3.24** Schematic of  $109^\circ$  domain switching-induced  $90^\circ$  rotation of magnetization



### 3.5.2 Magnetic Field-Assisted Electric-Field Control of Magnetization Reversal

It should be noticed that the nonvolatile electrical control of magnetization in our observations is not electric-field control of magnetization reversal but only electric field manipulating the amplitude of magnetization. In principle, the distortions induced by local  $109^\circ$  ferroelastic domain switching are bidirectional and only  $90^\circ$  rotation of magnetization can be achieved, as shown in Fig. 3.24.

For the electrical writing and magnetic reading device, reversible and deterministic reversal of magnetization is important for applications. Although the  $90^\circ$  rotation of magnetization can result in magnetoresistance change in spintronic devices, the  $180^\circ$  reversal of magnetization is still important for increasing the storage density and readout sensitivity. However, the electric-field controlled reversible and deterministic reversal of magnetization in FM/FE heterostructures at room temperature is still limited. Thereby, a method of magnetization reversal controlled by electric fields and assisted with a magnetic field was demonstrated. One period of the manipulation is shown in Fig. 3.25.

The upper panel in Fig. 3.25 shows the variation of magnetization (open circle) with electric field (blue line) at different time. The scheme of the lower-panel describes the external magnetic field ( $H$ ) by arrow with a broken tail, projection of distortion ( $D$ ) of the rhombohedral phase by dashed rhomb, magnetization ( $M$ ) state by solid arrow and easy direction of magnetization by open arrow at different stages corresponding to the upper panel. One period of the electric-field control of magnetization reversal with the assistance of magnetic fields can be achieved in 5 steps described as following. First, the CoFeB film was magnetized by a large negative magnetic field and then the magnetization was measured at  $-10$  Oe, during which a positive electric field of  $+8$  kV/cm was applied to make the easy direction of magnetization for CoFeB along the magnetic field. In this situation, the magnetization is stable as both the magnetization and external magnetic field

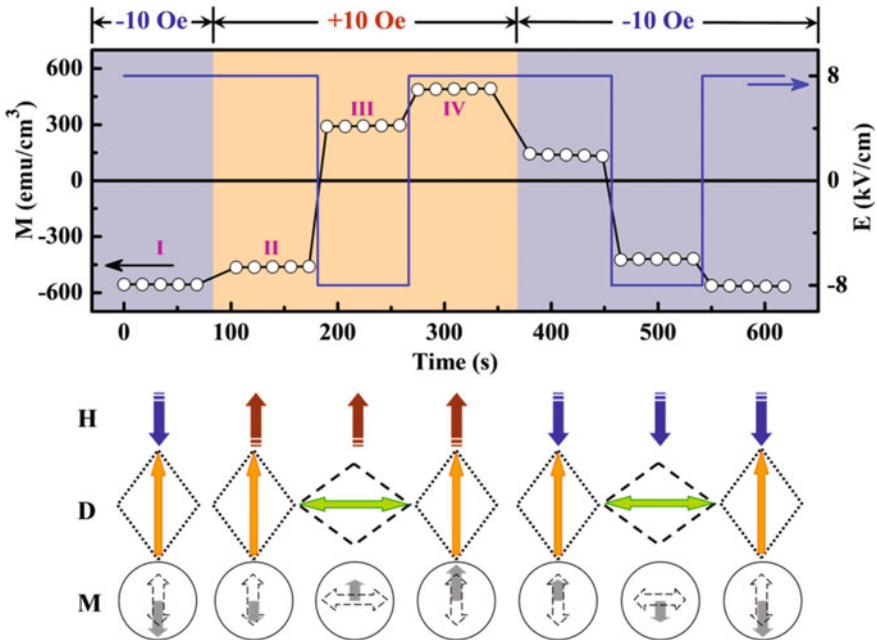


**Fig. 3.25** Process of magnetization reversal controlled by electric fields with the assistance of magnetic fields along the  $[-110]$  direction

are along the same direction, shown as stage (I) in Fig. 3.25. Then, the magnetic field was switched to +10 Oe with the electric field unchanged. Since the coercive field of CoFeB is a little bit larger than 10 Oe as shown in the M-H curve in Fig. 3.9a, 10 Oe magnetic field is not strong enough to change the magnetization to the positive direction, however, it shows a minor decrease as shown in the stage (II) in Fig. 3.25. This configuration is unstable with magnetization antiparallel to the external magnetic field, and can be easily switched to the positive direction by a change of the local easy direction of magnetization due to the distortion variation in the following stage (III), where the electric field is switched from positive to negative. In this case, the magnetization turns to the positive direction along the magnetic field, but lies in a hard direction of magnetization. Afterward, the electric field was changed to positive again, which rotated the local easy direction of magnetization back to the magnetic field direction, leading to an increase in magnetization to form a positive stable state shown as the stage (IV) in Fig. 3.25. A similar process was taken by switching the magnetic field to -10 Oe, followed by changing electric field, and similar behavior was observed compared to the previous case. The magnetization reversal process controlled by electric fields and assisted with a magnetic field is repeatable, holding promising applications in future.

### 3.6 Chapter Summary

In summary, a multiferroic  $\text{Co}_{40}\text{Fe}_{40}\text{B}_{20}/\text{Pb}(\text{Mg}_{1/3}\text{Nb}_{2/3})_{0.7}\text{Ti}_{0.3}\text{O}_3$  two-phase structure was prepared by depositing ferromagnetic  $\text{Co}_{40}\text{Fe}_{40}\text{B}_{20}$  film on top of (001)-oriented  $\text{Pb}(\text{Mg}_{1/3}\text{Nb}_{2/3})_{0.7}\text{Ti}_{0.3}\text{O}_3$  ferroelectric substrate in a ultra-high vacuum magnetron sputtering system. Via different magnetic measurements with in situ electric field in this structure, a large, tunable and nonvolatile converse ME effect was observed at room temperature, in which the magnetization of CoFeB film exhibits a *loop-like* response to electric field instead of the *butterfly-like* behavior commonly observed in the piezostain-mediated FM-FE structures. By further investigations on the ferroelectric domains, crystal structures and magnetic domains with in situ electric fields, it was demonstrated that the nonvolatile ME effect originates from the direct coupling between FE substrate and FM film with the combined action of  $109^\circ$  ferroelastic domain switching in PMN-PT and the absence of magnetocrystalline anisotropy in CoFeB, which is a novel mechanism for the electric control of magnetization in strain-mediated ME coupling system and nonvolatile electrical control of magnetization can be expected in FM/FE structures consisting of nonepitaxial FM layers with weak or no magnetocrystalline anisotropy and FEs with  $109^\circ$  ferroelastic switching. This work provides a new way to realize large, switchable and non-volatile magnetoelectric coupling and is significant for applications.

### References

1. K.F. Wang, J.M. Liu, Y. Wang, Single-phase multiferroics—the coupling between magnetic and polarization orders. *Chin. Sci. Bull.* **53**, 1098–1135 (2008). (in Chinese)
2. C.W. Nan, M.I. Bichurin, S.X. Dong et al., Multiferroic magnetoelectric composites: historical perspective, status, and future directions. *J. Appl. Phys.* **103**, 031101 (2008)
3. C. Thiele, K. Dorr, O. Bilani et al., Influence of strain on the magnetization and magnetoelectric effect in  $\text{La}_{0.7}\text{A}_{0.3}\text{MnO}_3/\text{PMN-PT}(001)$  (A=Sr,Ca). *Phys. Rev. B* **75**, 054408 (2007)
4. S. Sahoo, S. Polisetty, C.G. Duan et al., Ferroelectric control of magnetism in  $\text{BaTiO}_3/\text{Fe}$  heterostructures via interface strain coupling. *Phys. Rev. B* **76**, 092108 (2007)
5. S. Brivio, D. Petti, R. Bertacco et al., Electric-field control of magnetic anisotropies and magnetic coercivity in  $\text{Fe}/\text{BaTiO}_3(001)$  heterostructures. *Appl. Phys. Lett.* **98**, 92505 (2011)
6. Y.J. Chen, J.S. Gao, T. Fitchorov et al., Large converse magnetoelectric coupling in  $\text{FeCoV}/\text{lead zinc niobate-lead titanate}$  heterostructure. *Appl. Phys. Lett.* **94**, 082504 (2009)
7. J.J. Yang, Y.G. Zhao, H.F. Tian et al., Electric field manipulation of magnetization at room temperature in multiferroic  $\text{CoFe}_2\text{O}_4/\text{Pb}(\text{Mg}_{1/3}\text{Nb}_{2/3})_{0.7}\text{Ti}_{0.3}\text{O}_3$  heterostructures. *Appl. Phys. Lett.* **94**, 212504 (2009)
8. J. Lou, M. Liu, D. Reed et al., Giant electric field tuning of magnetism in novel multiferroic  $\text{FeGaB}/\text{lead zinc niobate-lead titanate}$  (PZN-PT) heterostructures. *Adv. Mater.* **21**, 4711 (2009)
9. M. Liu, O. Obi, J. Lou et al., Giant electric field tuning of magnetic properties in multiferroic ferrite/ferroelectric heterostructures. *Adv. Funct. Mater.* **19**, 1826–1831 (2009)

10. M. Liu, O. Obi, J. Lou et al., Strong magnetoelectric coupling in ferrite/ferroelectric multiferroic heterostructures derived by low temperature spin-spray deposition. *J. Phys. D-Appl. Phys.* **42**, 045007 (2009)
11. J. Ma, Y.H. Lin, C.W. Nan, Anomalous electric field-induced switching of local magnetization vector in a simple FeBSiC-on-Pb(Zr, Ti)O<sub>3</sub> multiferroic bilayer. *J. Phys. D-Appl. Phys.* **43**, 012001 (2010)
12. S. Geprags, A. Brandlmaier, M. Opel et al., Electric field controlled manipulation of the magnetization in Ni/BaTiO<sub>3</sub> hybrid structures. *Appl. Phys. Lett.* **96**, 142509 (2010)
13. J. Wang, J. Ma, Z. Li et al., Switchable voltage control of the magnetic coercive field via magnetoelectric effect. *J. Appl. Phys.* **110**, 043919 (2011)
14. H.C. Xuan, L.Y. Wang, Y.X. Zheng et al., Electric-field control of magnetism without magnetic bias field in the Ni/Pb(Mg<sub>1/3</sub>Nb<sub>2/3</sub>)O<sub>3</sub>-PbTiO<sub>3</sub>/Ni composite. *Appl. Phys. Lett.* **99**, 032509 (2011)
15. W. Eerenstein, M. Wiora, J.L. Prieto et al., Giant sharp and persistent converse magnetoelectric effects in multiferroic epitaxial heterostructures. *Nat. Mater.* **6**, 348–351 (2007)
16. S.E. Park, T.R. Shrout, Ultrahigh strain and piezoelectric behavior in relaxor based ferroelectric single crystals. *J. Appl. Phys.* **82**, 1804–1811 (1997)
17. H.X. Fu, R.E. Cohen, Polarization rotation mechanism for ultrahigh electromechanical response in single-crystal piezoelectrics. *Nature* **403**, 281–283 (2000)
18. B. Noheda, D.E. Cox, G. Shirane et al., Phase diagram of the ferroelectric relaxor (1-x)PbMg<sub>1/3</sub>Nb<sub>2/3</sub>O<sub>3</sub>-xPbTiO<sub>3</sub>. *Phys. Rev. B* **66**, 054104 (2002)
19. S.U. Jen, Y.D. Yao, Y.T. Chen et al., Magnetic and electrical properties of amorphous CoFeB films. *J. Appl. Phys.* **99**, 053701 (2006)
20. T. Kubota, T. Daibou, M. Oogane et al., Tunneling spin polarization and magnetic properties of Co-Fe-B alloys and their dependence on boron content. *Jpn. J. Appl. Phys.* **46**, L250–L252 (2007)
21. S. Zhang, Y.G. Zhao, P.S. Li et al., Electric-field control of nonvolatile magnetization in Co<sub>40</sub>Fe<sub>40</sub>B<sub>20</sub>/Pb(Mg<sub>1/3</sub>Nb<sub>2/3</sub>)<sub>0.7</sub>Ti<sub>0.3</sub>O<sub>3</sub> structure at room temperature. *Phys. Rev. Lett.* **108**, 137203 (2012)
22. T.K. Chung, G.P. Carman, K.P. Mohanchandra, Reversible magnetic domain-wall motion under an electric field in a magnetoelectric thin film. *Appl. Phys. Lett.* **92**, 112509 (2008)
23. T. Brintlinger, S.H. Lim, K.H. Baloch et al., In situ observation of reversible nanomagnetic switching induced by electric fields. *Nano Lett.* **10**(4), 1219–1223 (2010)
24. H. Molegraaf, J. Hoffman, C. Vaz et al., Magnetoelectric effects in complex oxides with competing ground states. *Adv. Mater.* **21**, 3470 (2009)
25. D. Chiba, M. Sawicki, Y. Nishitani et al., Magnetization vector manipulation by electric fields. *Nature* **455**, 515–518 (2008)
26. T. Maruyama, Y. Shiota, T. Nozaki et al., Large voltage-induced magnetic anisotropy change in a few atomic layers of iron. *Nat. Nanotechnol.* **4**, 158–161 (2009)
27. C.G. Duan, S.S. Jaswal, E.Y. Tsymlal, Predicted magnetoelectric effect in Fe/BaTiO<sub>3</sub> multilayers: ferroelectric control of magnetism. *Phys. Rev. Lett.* **97**, 047201 (2006)
28. T. Zhao, A. Scholl, F. Zavaliche et al., Electrical control of antiferromagnetic domains in multiferroic BiFeO<sub>3</sub> films at room temperature. *Nat. Mater.* **5**, 823–829 (2006)
29. F. Zavaliche, S.Y. Yang, T. Zhao et al., Multiferroic BiFeO<sub>3</sub> films: domain structure and polarization dynamics. *Phase Transitions* **79**, 991–1017 (2006)
30. S.H. Baek, H.W. Jang, C.M. Folkman et al., Ferroelastic switching for nanoscale non-volatile magnetoelectric devices. *Nat. Mater.* **9**, 309–314 (2010)
31. P.F. Fewster, Reciprocal space mapping. *Crit. Rev. Solid State Mater. Sci.* **22**, 69–110 (1997)
32. A.A. Levin, A.I. Pommrich, T. Weissbach et al., Reversible tuning of lattice strain in epitaxial SrTiO<sub>3</sub>/La<sub>0.7</sub>Sr<sub>0.3</sub>MnO<sub>3</sub> thin films by converse piezoelectric effect of 0.72Pb(Mg<sub>1/3</sub>Nb<sub>2/3</sub>)O<sub>3</sub>-0.28 PbTiO<sub>3</sub> substrate. *J. Appl. Phys.* **103**, 054102 (2008)
33. M. Birkholz, P.F. Fewster, C. Genzel, *Thin Film Analysis by X-Ray Scattering* (Wiley-VCH Verlag GmbH, Weinheim, 2006)

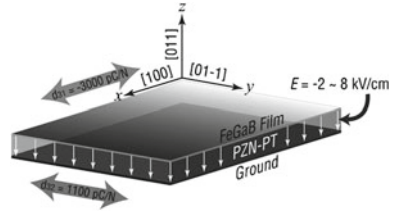
# Chapter 4

## Electric-Field Control of Magnetism and Magnetoresistance in CoFeB/PMN-PT(011) Structure

### 4.1 Introduction

As described in the first chapter of this book, one of the main aims in the investigation of multiferroic materials and magneto-electric (ME) coupling effect is to realize electrical writing and magnetic reading information storage devices for the next generation. Thereby, a lot of new type memory models based on multiferroic materials have been proposed and designed. The first multiferroic memory model was proposed by Tsymbal et al. [1], in which ferroelectric (FE) or multiferroic materials were employed as the barrier layer in magnetic tunnel junctions (MTJs) to realize multi-resistance states random access memories. Subsequently, Gajek et al. [2] and Garcia et al. [3] reported the experimental work related to the proposal and “four-state” memories that were realized at low temperature. However, ferroelectric or multiferroic materials are difficult to maintain their good ferroelectric or multiferroic properties in thin films, resulting in difficulty in the device preparation. Besides, both the aforementioned experimental work related “four-state” memories were achieved at low temperature (at 4 and 50 K respectively), which is disadvantageous for applications. The second model was proposed by Bibes et al. [4], in which MTJs was prepared on top of single-phase multiferroic materials. Through exchange bias coupling effect between the antiferromagnetic order in the multiferroic layer and ferromagnetic (FM) order in the bottom electrode of MTJ, an electrical writing and magnetic reading random access memory can be realized. The related experimental work was reported by Wu et al. [5] and Allibe et al. [6] respectively. Since single-phase multiferroic materials are rare at room temperature, the relevant investigations are limited and the aforementioned results are mainly reported in exchange bias system related to BiFeO<sub>3</sub>. The third model was proposed by Pertsev et al. [7] and Hu et al. [8], in which MTJs was prepared on top of piezoelectric or ferroelectric substrates. Through strain coupling effect between the FE substrates and the FM layers in MTJs, the electrical writing and magnetic reading random access memory can also be realized at room temperature. The relevant experimental work was first tried by Cavaco et al. [9], and Liu et al. [10] also reported the similar work recently. Due to the vast choices of ferroelectric/piezoelectric and ferromagnetic materials at room

**Fig. 4.1** In-plane strain anisotropy of (011)-oriented PZN-PT (Reproduced from Ref. [12] by permission of John Wiley & Sons Ltd)



temperature, electrical writing and magnetic reading random access memories based on strain modulation have broad prospects and applications.

In order to realize the new type electrical writing and magnetic reading random access memories, investigation of ME coupling effect in terms of electric-field control of magnetization is significant. Thereby in recent years, the electric-field control of magnetism which is known as the converse ME effect has been extensively studied as mentioned in the previous chapters. Despite the large number of experimental reports, large magnetic response to electric stimuli, which can be performed at room temperature with low magnetic field, is also limited and requires more attempts.

According to reports, FE single crystals such as lead magnesium niobate—lead titanate  $\text{Pb}(\text{Mg}_{1/3}\text{Nb}_{2/3})\text{O}_3\text{-xPbTiO}_3$  (PMN-xPT) and lead zinc niobate—lead titanate  $\text{Pb}(\text{Zn}_{1/3}\text{Nb}_{2/3})\text{O}_3\text{-xPbTiO}_3$  (PZN-xPT) exhibit ultra-high piezoelectric behaviors [11], which have a strong strain anisotropy in plane (i.e., tensile strain along the [01-1] direction and compressive strain along the [100] direction) with electric fields applied along the [011] crystalline direction in the (011)-cut case, as shown in Fig. 4.1. Utilizing this in-plane anisotropic piezostain, the (011)-oriented wafers of PMN-PT and PZN-PT can be employed in the strain-mediated multiferroic heterostructures to realize giant ME coupling effect and electric-field control of magnetization [12, 13].

On the other hand, FM materials employed in the spin-dependent transport devices with high spin polarization and large magnetoresistance effect are preferable for ME coupling. The amorphous  $\text{Co}_{40}\text{Fe}_{40}\text{B}_{20}$  (CoFeB), with perfect soft magnetic properties and absence of magnetocrystalline anisotropy [14], has been reported to possess the highest spin polarization among the amorphous ferromagnetic Co-Fe-B alloys and has been widely used in MTJs to achieve very large tunneling magnetoresistance (TMR) at room temperature. Therefore, the combination of CoFeB thin film and PMN-PT(011) single crystal is an ideal candidate for achieving large ME effects and for exploring the electric-field modulation of the magnetization and magnetic anisotropy in FM materials without magnetocrystalline anisotropy via the in-plane anisotropic piezostain [15]. Furthermore, spin valve structures based on CoFeB can be prepared on the (011)-oriented PMN-PT for further investigation of the electric-field control of giant magnetoresistance (GMR) effect, which is important for realizing strain-mediated magnetoelectric random access memory (SME-RAM) [8].

## 4.2 Sample Preparation and Characterization

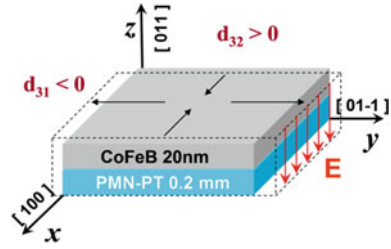
### 4.2.1 Sample Preparation

Similar to the sample preparation method described in the previous chapter, commercial (011)-oriented PMN-30 %PT single crystal was one-side polished and cut into a slab of size  $3 \times 2.5 \times 0.2 \text{ mm}^3$  to be used as the FE substrate for the growth of the ferromagnetic film. Since the piezoresponses ( $d_{xy}$ ) along the two in-plane axes are different in the (011)-oriented PMN-PT (i.e.,  $d_{31} > 0$  along the [100] direction and  $d_{32} > 0$  along the [01-1] direction), it is necessary to make the in-plane lengths of the sample different enough to distinguish the two different axes. After ward, amorphous  $\text{Co}_{40}\text{Fe}_{40}\text{B}_{20}$  film with a thickness of 20 nm was deposited on top of the PMN-PT substrate and followed by a 10 nm tantalum (Ta) via an ultra-high vacuum (ULVAC) magnetron sputtering system with a biased atmospheric pressure of  $1 \times 10^{-6}$  Pa. The high vacuum environment and capping layer of Ta are essential for preventing active elements such as cobalt (Co) and iron (Fe) in the CoFeB thin film from being oxidized during deposition and after taking out of the chamber. Compared with pulsed laser deposition (PLD), the growth temperature of the magnetron sputtering method is low. As a result, the problem related to volatilization of lead (Pb) in PMN-PT substrate at high temperature can be avoided during deposition, which ensures the reliability of the sample components. The brief configuration of the FM/FE structure is shown in Fig. 4.2.

To investigate the electric-field control of magnetism in the sample, Au layer with thickness of 300 nm was sputtered on both sides of the FM/FE structure as electrode, and the polished side of PMN-PT with CoFeB film was defined as the positive electrode. A high-voltage source-meter was employed to supply electric fields and an ammeter together with a 16 M $\Omega$  protecting resistor which was series-wound in the circuit to monitor the current during all the measurements performed at room temperature. All the sample structure, measurement method, and configuration of applying electric fields are the same as those in the previous chapter (see Fig. 3.2). The major differences are the orientation of the PMN-PT wafer selected as (011)-cut to realize anisotropic strain in plane and the sample thickness has been reduced to 0.2 mm to achieve higher electric field with limited voltage as shown in Fig. 4.2.

In addition, this chapter also involves the preparation method related to spin valve structure based on CoFeB, which can be easily achieved via the ultra-high vacuum magnetron sputtering system. The detailed fabrication process as well as sample structure is described later in the chapter.

**Fig. 4.2** In-plane strain anisotropy of the CoFeB/PMN-PT(011) structure under external electric field (Reprinted with permission from Macmillan Publishers Ltd: Ref. [15], copyright 2014)



### 4.2.2 Characterization of Crystal Structure, Ferroelectricity, and Piezoelectricity

We also used the Rigaku-D/max-RB X-ray diffractometer to determine the orientation and crystal structure of the PMN-PT single crystal and the relevant results are shown in Fig. 4.3. According to reports [11], the spontaneous polarizations of PMN-PT with rhombohedral (R) phase are along the  $\langle 111 \rangle$  directions, i.e., the body diagonals of the pseudo-cubic unit cell in the (001)-cut case. While in the (011)-cut case, the spontaneous polarizations lie along the diagonals of the (011) and (01-1) plane, as shown in Fig. 4.3a. The X-ray diffraction pattern of the (011)-cut PMN-PT substrate is shown in Fig. 4.3b, from which the out-of-plane lattice parameter can be deduced as 2.843 Å. Moreover, transmission electron microscope (TEM) was also employed to visualize the crystal lattice of PMN-PT as well as the amorphous texture of CoFeB thin film. The results of the TEM investigation are similar to those in the previous chapter (see Fig. 3.4), which are not shown here.

We also employed Radiant Premier II ferroelectric analyzer to characterize ferroelectric properties of the sample, and the result is shown in Fig. 4.4a. From the ferroelectric hysteresis loop (P–E) of the sample, one can see that the coercive field of the (011)-oriented PMN-PT substrate is about 4 kV/cm, which is larger than the (001)-oriented case (coercive field about 2 kV/cm as shown in Fig. 3.5a of Chap. 3). Therefore, the sample thickness has been reduced to 0.2 mm to reach larger electric field with the same voltage. One can also find that the saturated polarization is about 28  $\mu\text{C}/\text{cm}^2$ , which is larger than the (001)-oriented case (saturated polarization about 25  $\mu\text{C}/\text{cm}^2$  as shown in Fig. 3.5a of Chap. 3) and can be easily understood as the  $\langle 111 \rangle$ -oriented spontaneous polarization vectors of PMN-PT which have larger component in the [011] direction than the [001] direction. Meanwhile, the switching current during polarization reversal and leakage current at high voltage of the sample have also been measured and the current-voltage (I–V) curve is shown in Fig. 4.4b. As one can see from the figure, a giant current peak with maximum value about 0.25  $\mu\text{A}$  appears with electric fields around the coercive field of PMN-PT, which can be easily understood as the switching current due to polarization reversal. When the electric field exceeds the coercive field of PMN-PT, the current will decrease rapidly with leakage current less than 10 nA under electric field of 20 kV/cm, indicating that the PMN-PT sample we used here has good performances in ferroelectricity and insulation.

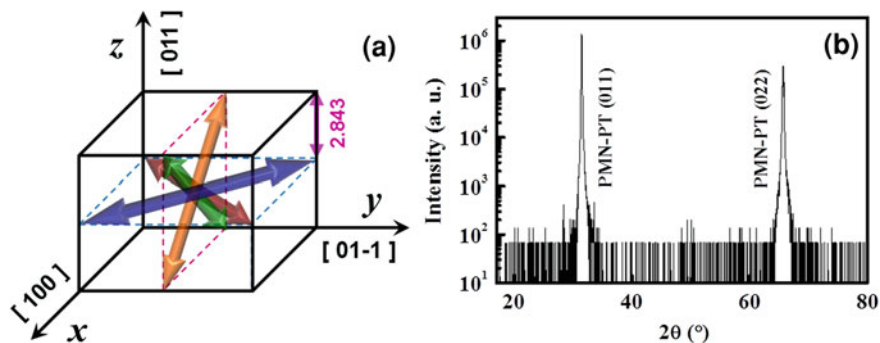


**Fig. 4.3** The **a** spontaneous polarizations and **b** X-ray diffraction patterns of PMN-PT with rhombohedral phase in the (011)-cut cases (Reprinted with permission from Macmillan Publishers Ltd: Ref. [15], copyright 2014)

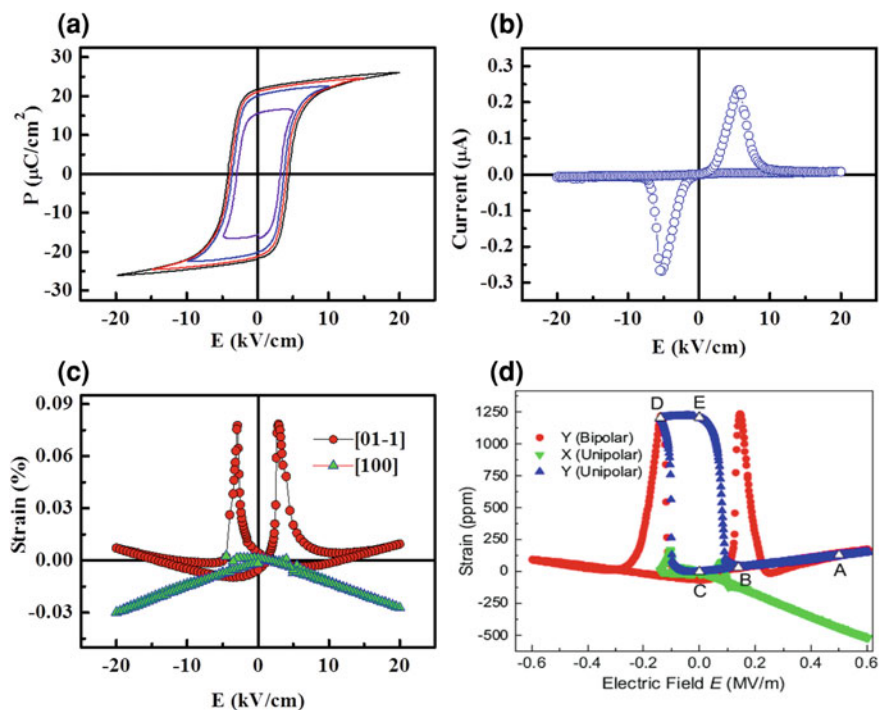


**Fig. 4.4** The **a** ferroelectric hysteresis loops, **b** leakage current and **c** strain curve of the sample. **(d)** Strain curve as reported for comparison (Reprinted with permission from Ref. [16]. Copyright 2011, American Institute of Physics)

Besides, we also employed the self-building strain measurement system based on strain gauge to characterize the in-plane strain properties of PMN-PT and the piezostain result along the [01-1] and [100] directions as shown in Fig. 4.4c, which is consistent with the previous report as shown in Fig. 4.4d [16]. By the basic characterization mentioned above, we can see that the CoFeB/PMN-PT(011) sample has been well prepared with good quality crystal structure, ferroelectricity and piezoelectricity, which are important for further investigation on electric control of magnetization as follows.

### 4.3 Electric-Field Control of Magnetism

#### 4.3.1 Electric-Field Control of Magnetization

As mentioned in the previous sections, the purpose of choosing this (011)-cut PMN-PT wafer is due to its strong in-plane anisotropic piezoresponse to external electric field. When poled along the [011] direction, the (011)-cut PMN-PT wafer will exhibit compressive strain along the [100] direction and outstretched strain along the [01-1] direction as shown in Fig. 4.2, due to the polarizations reorientation under electric field. According to reports [17, 18], the (011)-cut PMN-30 %PT we use here has optimized orientation and composition to achieve ultra-high in-plane piezoelectric coefficients with  $d_{31} \sim -3,100$  pC/N along the [100] direction and  $d_{32} \sim 1,400$  pC/N along the [01-1] direction, respectively. This giant anisotropic piezostain provides a great opportunity to generate a large in-plane magnetic anisotropic field and achieve  $90^\circ$  easy axis rotation as well as large magnetization response to electric field.

Electric-field control of magnetization was carried out in a Magnetic Property Measurement System (MPMS) with in situ electric fields (See the experimental method described in Chap. 3). First, the magnetic hysteresis (M–H) loops were measured along the [100] and [01-1] directions under electric fields 0, 10, and 20 kV/cm, respectively, and the results are shown in Fig. 4.5.

From the figures we can see that the magnetic response to external electric field are different in the two directions. The magnetization process of the sample along the [100] direction becomes harder and the remnant magnetization ( $M_r$ ) reduces when the electric field increases as shown in Fig. 4.5a. We can also find that the saturation magnetic field ( $H_S$ ) changes from about 20 Oe at 0 kV/cm to about 500 Oe at 20 kV/cm, which obviously inclines the “square” M–H curve to a “flat” one. However, the magnetic response to electric field is not so obvious along the [01-1] direction, and the situation is just the converse to that along the [100] direction, with an increment of the M–H squareness as well as remnant magnetization under large electric fields, as shown in Fig. 4.5b and its insert.

To understand the magnetic difference between the two directions, sketch models related to electric-field control of magnetic anisotropy have been put

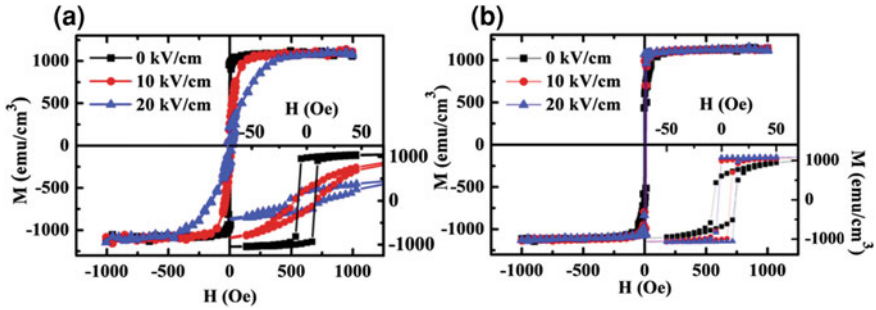
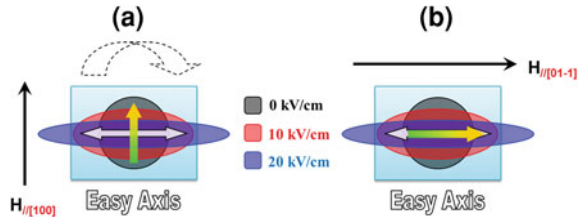


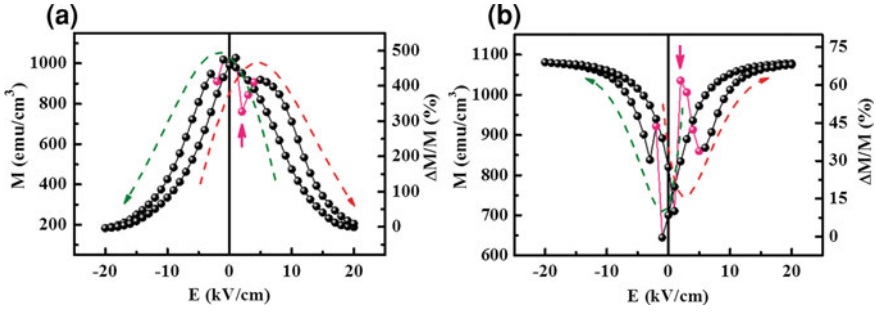
**Fig. 4.5** Electric-field control of magnetic hysteresis loop along the **a** [100] and **b** [01-1] directions of the sample (Reprinted with permission from Macmillan Publishers Ltd: Ref. [15], copyright 2014)

**Fig. 4.6** Understanding the magnetic response to different electric fields along the **a** [100] and **b** [01-1] directions



forward as shown in Fig. 4.6. Without electric field, the ferromagnetic CoFeB layer exhibits in-plane magnetic isotropy; for the amorphous CoFeB it has neither magnetocrystalline anisotropy nor induced magnetic anisotropy by external magnetic field during the fabrication. When external electric field is applied on the sample along the [011] direction, in-plane anisotropic strain is generated as shown in Fig. 4.2, which induces an uniaxial magnetic anisotropy of CoFeB layer with easy axis along the [01-1] direction and hard axis along the [100] direction. When performing the magnetization measurement along the [100] direction by MPMS, the magnetic field is also applied along the [100] direction. In this situation, the direction of external magnetic field ( $H$ ) is perpendicular to the induced magnetic easy axis as shown in Fig. 4.6a. As a result, the magnetic moments of CoFeB will rotate between the [100] and [01-1] directions with the change of external magnetic field, which leads to an obvious change in  $M$ - $H$  curve along the [100] direction. However, in the magnetization measurement along the [01-1] direction, since the direction of external magnetic field is parallel to the electric field induced magnetic easy axis as shown in Fig. 4.6b, the magnetic moments of CoFeB can only flip along the [01-1] direction with the change in external magnetic field, resulting in larger remnant magnetization and more “square”  $M$ - $H$  loop.

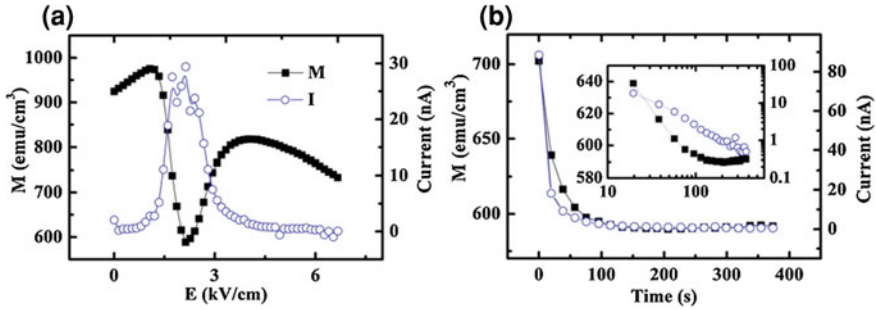
In order to directly investigate the electric-field control of magnetization, magnetic measurement under step changed electric field (i.e. from +20 to



**Fig. 4.7** Direct electrical control of magnetization ( $M$ - $E$  curves) of the sample along the **a** [100] and **b** [01-1] directions (Reprinted with permission from Macmillan Publishers Ltd: Ref. [15], copyright 2014)

$-20$  kV/cm with a step of 1 kV/cm) with a biased magnetic field ( $H = 5$  Oe) was performed, and the variations of magnetization with electric field along the two directions are shown in Fig. 4.7a and b, respectively. The magnetization response to electric field along the [100] direction exhibits a symmetrical *butterfly-like* behavior, similar to the previous report in other FM/FE heterostructure [19]. However, the relative change in magnetization ( $\Delta M/M$ ) is larger than the previous result. From the  $M$ - $E$  curve as shown in Fig. 4.7a, one can see that the magnetization changes from above 1,000 to lower than 200  $\text{emu}/\text{cm}^3$  with electric field changing from 0 to 20 kV/cm, and the relative magnetization change ( $\Delta M/M$ ) is up to 450 %. This giant electrical modulation of magnetization originates from the combination of the ultra-high value of anisotropic in-plane piezoelectric coefficients of (011)-cut PMN-PT [17, 18] and the perfect soft ferromagnetism without magnetocrystalline anisotropy of CoFeB film [14]. The  $M$ - $E$  curve along the [01-1] direction also has a *butterfly-like* shape but with an opposite behavior compared to the curve along the [100] direction, i.e., electric field increases the magnetization from about 700 to near 1100  $\text{emu}/\text{cm}^3$  with  $\Delta M/M \sim 66$  % as shown in Fig. 4.7b. These results can be understood by the electric field-induced magnetic anisotropy as discussed above and agree with the  $M$ - $H$  curve changes as shown in Fig. 4.5.

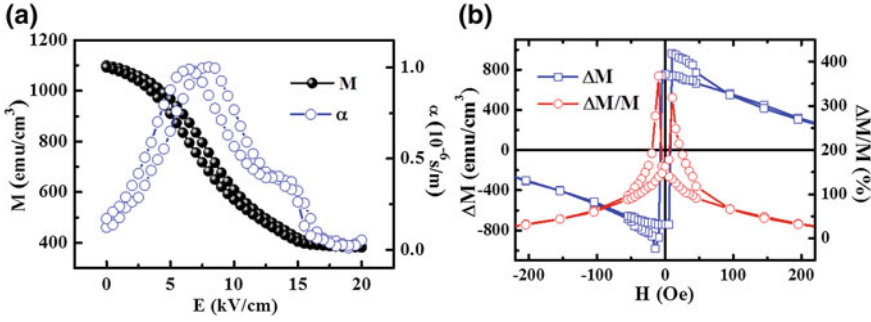
Moreover, by carefully observing the  $M$ - $E$  curves in Fig. 4.7, one can see that there are several data points jumping away from the regular *butterfly-like*  $M$ - $E$  curves, as masked by pink color and denoted by pink arrows in Fig. 4.7b and c. Since these anomalous points appear around the coercive field of PMN-PT (about 5 kV/cm), they are considered to originate from the domain reorientation effect during polarization reversal process, which results in the change in magnetization. To explore and confirm the mechanism for the appearance of anomalous data points,  $M$ - $E$  measurement at low electric fields ( $3 \sim 6$  kV/cm) near the coercive field of PMN-PT with a small increment of electric field (0.2 kV/cm) was carried out after poling the sample with a large negative electric field, and the relevant results are shown in Fig. 4.8.



**Fig. 4.8** Investigation of **a** the electrical control of magnetization and **b** relaxation behavior of ME coupling along the [100] direction near the coercive field of PMN-PT (Reprinted with permission from Macmillan Publishers Ltd: Ref. [15], copyright 2014)

It can be seen that the anomalous data points around the coercive field of PMN-PT in the previous results as shown in Fig. 4.7a turn to be a smooth valley in the M–E curve as shown in Fig. 4.8a. What is more, the polarization current during domain switching was also automatically recorded by an ammeter during the M–E measurement and the current–electric field (I–E) curve is also shown in Fig. 4.8a. As one can see from the figure, the change in magnetization and variation of polarization switching current have good correspondence, which indicates the association between the magnetization transition and the ferroelectric polarization reorientation. In fact, this behavior is consistent with the result of strain measurement as shown in Fig. 4.4c, and the sharp change is related to the existence of metastable state in which the spontaneous polarization vector of PMN-PT will lie in the (011) plane during polarization reversal process, as reported by Wu et al. [16] in the similar structure with a unipolar case. Notably, the magnetoelectric coupling around the coercive field of PMN-PT is huge and has been considered useful in terms of nonvolatile ME effect and SME-RAMs [8, 16]. However, relaxation behavior of ME coupling has been observed in the polarization reversal process by further measuring magnetization continuously at fixed electric field (e.g., 2 kV/cm) and the result is plotted with normal scale as shown in Fig. 4.8b and logarithm scale as shown in the inset of Fig. 4.8b. From the M–time and I–time curves, one can infer that the relaxation of magnetization is caused by the relaxation of polarization switching and about 100–350 s are needed to reach a stable magnetization state, which may hinder the applications in high-speed SME-RAMs in similar structures. The relaxation of polarization of the sample originates from the dynamic evolution of the metastable domain states during polarization reversal process in PMN-PT and needs to be further studied.

Since the anomalous points in the M–E curves as shown in Figs. 4.7a, b and 4.8a originate from the domain reorientation during polarization reversal process and result in relaxation behavior in electric-field control of magnetization, they can be eliminated in the M–E measurement with unipolar case. Since the M–E curves are almost symmetrical for the positive and negative electric fields as shown in



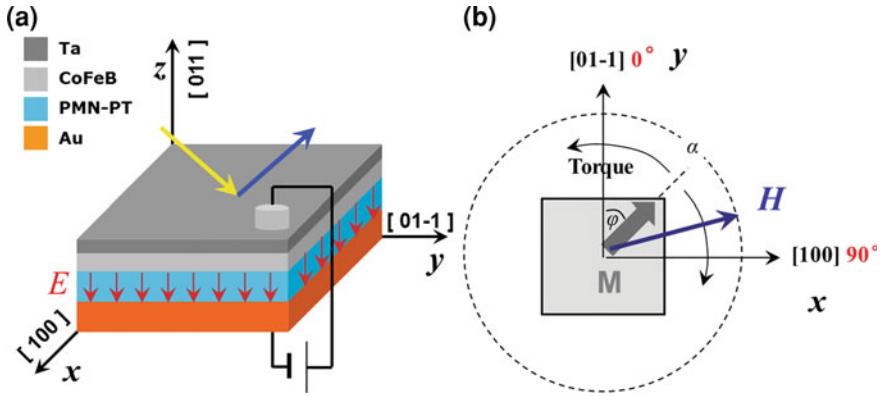
**Fig. 4.9** The **a**  $M$ - $E$  curve under unipolar electric field and **b** relative magnetization change with biased magnetic field

Fig. 4.7a and b, we mainly investigated the electric control of magnetization along the  $[100]$  direction under positive unipolar electric fields.

The sample was first poled by a positive electric field and then the  $M$ - $E$  measurement was started with increasing positive electric field. The result is presented in Fig. 4.9a, which shows a nonlinear  $M$ - $E$  curve with small hysteresis, and the anomalous points in the bipolar case as shown in Fig. 4.7a disappear as expected, as there is no polarization reversal process under unipolar electric fields. Thus, we can analyze the tendency of magnetization tuned by electric field without the disturbance of the anomalous points. According to the definition of magnetoelectric coupling coefficient ( $\alpha = \mu_0 dM/dE$ ), the variation of ME coupling coefficient can be deduced by differentiating the  $M$ - $E$  curve in Fig. 4.9a and the result is also shown in Fig. 4.9a, with a maximum value about  $1 \times 10^{-6}$  s/m at about 8  $\text{kV}/\text{cm}$ . This phenomenon is considered to be associated with the ferroelectric phase transition in PMN-PT under high electric field [20]. To further investigate the factors which determine the ME coupling effect, the absolute and relative magnetization changes (i.e.,  $\Delta M$  and  $\Delta M/M$ ) variation with the biased magnetic fields under electric field of 20  $\text{kV}/\text{cm}$  have been measured and results are shown in Fig. 4.9b. From the figure we can find that the changes in magnetization ( $\Delta M$  and  $\Delta M/M$ ) are larger under lower magnetic field, which can be understood as the magnetic moment ( $M$ ) can be easily rotated by the electric field-induced uniaxial magnetic anisotropic field ( $H_u$ ) with smaller external magnetic fields ( $H$ ).

### 4.3.2 Mechanism and Quantitative Investigation

To further understand the electric-field control of magnetism and magnetic anisotropy in the CoFeB/PMN-PT (011) structure, magnetic optic Kerr effect with a rotating field (Rot-MOKE) [21] was employed with in situ electric field via cooperation with Prof. Wu's group at Fudan University. The basic configuration of



**Fig. 4.10** The **a** configuration and **b** schematic of the MOKE measurement with in situ electric field

the experiment with the way of applying electric field is shown in Fig. 4.10a, along with the sample structure used for the Rot-MOKE measurement, i.e., Ta(5 nm)/CoFeB(20 nm)/PMN-PT(0.2 mm)/Au(300 nm). The reduced thickness of Ta layer is helpful to get better signal in the MOKE measurement.

The Rot-MOKE is based on the coherent rotation model, in which the sample is magnetized into a single domain state by a large magnetic field, and then the direction of external field is rotated as shown in Fig. 4.10b. The angle between the direction of magnetic moment ( $M$ ) and easy axis (i.e., the  $[01-1]$  direction) is denoted as  $\phi$ , and the angle between the direction of external magnetic field ( $H$ ) and the easy axis is denoted as  $\alpha$ . Therefore, the angle between the direction of external magnetic field ( $H$ ) and the direction of magnetic moment ( $M$ ) is  $\alpha - \phi$ . For the case of pure uniaxial anisotropy, the gross energy density of the system can be expressed by the following equation:

$$e = \frac{E}{V} = -M_S H \cos(\alpha - \phi) + K_u \sin^2 \phi \quad (4.1)$$

where  $E$  is the gross energy,  $V$  is the volume of the magnetic layer,  $M_S$  is the saturation magnetization, and  $K_u$  is the uniaxial anisotropy constant. The direction of magnetization is determined by minimizing the total energy per unit volume, which results in the following equation:

$$M_S H \sin(\alpha - \phi) = K_u \sin 2\phi \quad (4.2)$$

By defining the magnetic torque as

$$L[\alpha(\phi)] = V M_S H \sin(\alpha - \phi) \quad (4.3)$$

and defining the equivalent uniaxial anisotropy field  $H_u$  as

$$H_u = 2 \frac{K_u}{M_S} \quad (4.4)$$

the final form of magnetic torque can be simplified as the following expression:

$$I(\phi) = \frac{L[\alpha(\phi)]}{VM_S} = H \sin(\alpha - \phi) = \frac{1}{2} H_u \sin 2\phi \quad (4.5)$$

In the Rot-MOKE experiment, the longitudinal effect of MOKE was used, where the magnetization vector is parallel to both the sample surface and the plane of incidence. Thereby, the magnetization can be obtained by measuring the deflection angle of the polarization between the incident and reflected lights. The plane of incident light and reflected light was fixed in the (001) plane of the sample as shown in Fig. 4.10a. Thus, the component of magnetization along the [01-1] ( $M_y$ ) can be determined. After magnetizing the sample into one domain state by a large magnetic field, the direction of the external magnetic field was rotated step-by-step. At each step, the value ( $H$ ) and direction ( $\alpha$ ) of the external field were acquired, and the direction of magnetization ( $\varphi$ ) was deduced by  $\cos(\varphi) = M_y/M_S$ . Then, the magnetic torque moment  $I(\varphi)$  was calculated by  $H \cdot \sin(\alpha - \varphi)$ . After rotating the external magnetic field by half a circle, a torque curve was obtained, as shown in Fig. 4.11a. From the figure, one can see that the sample exhibits a weak uniaxial magnetic anisotropy with fitted magnetic anisotropic field about 50 Oe without electric field and it turns to be a strong uniaxial magnetic anisotropy with fitted magnetic anisotropic field about 120 Oe under voltage of the 300 V (i.e., electric field of 15 kV/cm). According to theory, the integration of magnetic torque over angle  $\varphi$  gives the ratio between uniaxial anisotropy energy and saturation magnetization. Thus, the angle dependence of uniaxial anisotropy energy with electric field 15 kV/cm on and off can be obtained as shown in Fig. 4.11b, in which one can distinctly see a  $90^\circ$  rotation of the easy axis of the sample tuned by electric fields, i.e., the easy axis lies along the [100] direction at 0 kV/cm and along the [01-1] direction at 15 kV/cm.

To obtain the threshold electric field when the easy axis begins to rotate and the variation in the induced uniaxial magnetic anisotropy field with electric field, magnetic torque measurement was carried out under different electric fields as shown in Fig. 4.12a, and the deduced easy axis as well as the fitted value of uniaxial magnetic anisotropy field are shown in Fig. 4.12b. It reveals that the value of uniaxial magnetic anisotropy changes almost linearly from  $-53$  Oe at zero electric field to about 130 Oe at electric field of 15 kV/cm. For electric fields below 5 kV/cm, the direction of the easy axis stays along the [100] direction. However, it switches about  $90^\circ$  and lies along the [01-1] direction for electric fields above 5 kV/cm. The situation of the negative branch is almost the same, with a sharper easy axis switching process.

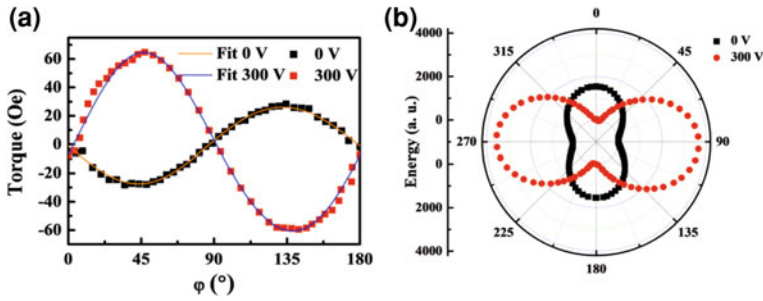


**Fig. 4.11** Electric-field control of magnetic anisotropy change of the sample: **a** magnetic torque and **b** polar plotting of uniaxial anisotropy energy curves, under different electric fields (Reprinted with permission from Macmillan Publishers Ltd: Ref. [15], copyright 2014)

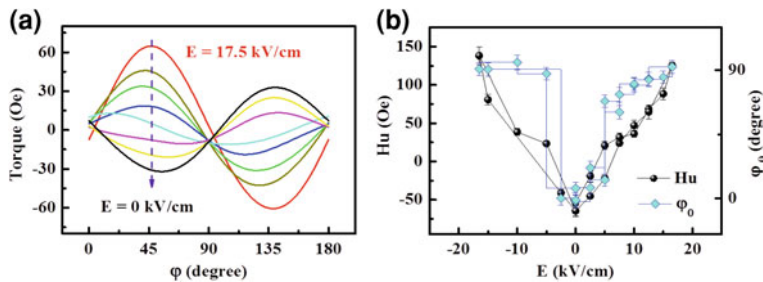


**Fig. 4.12** Electric-field control of magnetic anisotropy field of the sample: **a** magnetic torque curves under different electric fields and **b** the calculated amplitude of uniaxial magnetic anisotropy field as well as deduced direction of easy axis variation with electric field (Reprinted with permission from Macmillan Publishers Ltd: Ref. [15], copyright 2014)

### 4.3.3 Characterization and Design for Application

Considering the requirements of applications, the stability and repeatability of the converse ME effect have also been investigated. The sample was loaded by step-changed electric fields of 0, 10, and 20 kV/cm in sequence with magnetic field of 5 Oe, and stable, repeatable, and remarkable high/middle/low triple magnetization states were realized as shown in Fig. 4.13a and b for the [100] and [01-1] directions, respectively. As expected, the behavior along the [01-1] direction is reverse to that of the [100] direction and both agree with the M–E curves as shown in Fig. 4.7 in magnitude. This result should be useful for the promising applications-related SME-RAMs [8].

Using this giant electrical modulation of magnetization, especially the electric field controlled  $90^\circ$  rotation of the magnetic easy axis, a method of reversible and deterministic magnetization reversal (i.e.,  $180^\circ$  switching) controlled by pulsed electric fields with the assistance of weak magnetic fields was demonstrated, and the results are shown in Fig. 4.14.

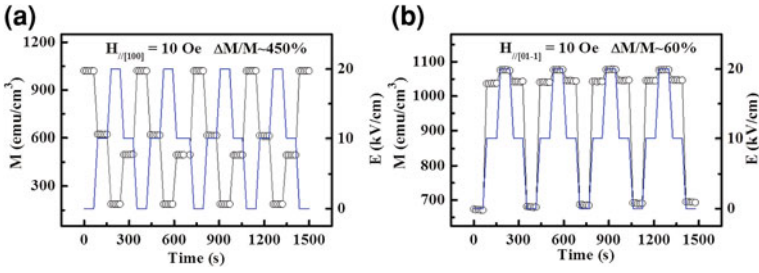


**Fig. 4.13** Electric-field control of different magnetization states along the **a** [100] and **b** [01-1] directions (Reprinted with permission from Macmillan Publishers Ltd: Ref. [15], copyright 2014)

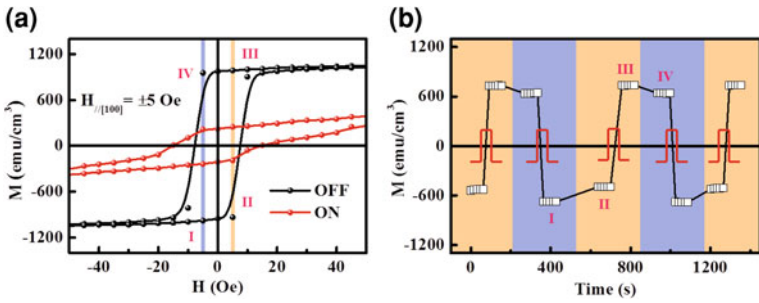
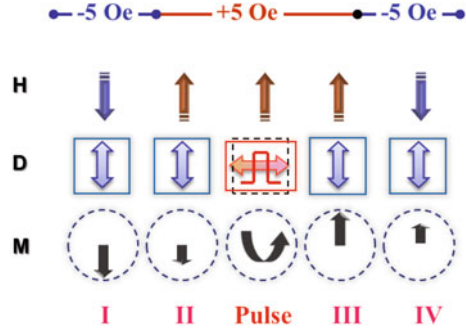


**Fig. 4.14** Electric-field control of magnetization reversal assisted by magnetic fields: **a** M-H curves with electric field on and off, **b** variation of magnetization with magnetic field and electric pulse at different time (Reprinted with permission from Macmillan Publishers Ltd: Ref. [15], copyright 2014)

One period of the manipulation with detailed process is described as follows. First, the CoFeB film was magnetized by a large negative magnetic field and then the magnetization was measured at  $-5$  Oe without electric field as denoted by stage I in Fig. 4.14a and b. According to the previous discussions, the induced easy axis of magnetization on PMN-PT is along the [100] direction when the electric field is off. In this situation, magnetization is stable since magnetization, easy axis, and external magnetic field are along the same direction (i.e., [100] direction) as shown in stage I of Fig. 4.15. Then, the magnetic field was switched to  $+5$  Oe as denoted by stage II in Fig. 4.14a and b. Since the coercive field of CoFeB is slightly larger than 5 Oe, the  $+5$  Oe magnetic field is not strong enough to switch the negative magnetization to the positive direction, however, it shows a minor change as shown in stage II of Fig. 4.14b. However, this configuration is metastable because magnetization is antiparallel to the external magnetic field as shown in stage II of Fig. 4.15. Afterward, a 20 kV/cm electric field was applied on the sample, resulting in a large in-plane anisotropic strain and rotation of the easy axis of magnetization to the [01-1] direction. This sudden change of easy axis broke the metastable state in stage II and the negatively aligned magnetization began to

**Fig. 4.15** Understanding the electrical control of magnetization reversal process (Reprinted with permission from Macmillan Publishers Ltd: Ref. [15], copyright 2014)



rotate toward the positive direction as shown in Fig. 4.15. Afterward, the electric field was turned off and the PMN-PT wafer changed back to the initial state, which rotated the easy axis of magnetization back to the [100] direction, leading to a positive stable state with magnetization, easy axis, and external magnetic field along the same direction, i.e., stage III of Figs. 4.14a, b and 4.15. A similar process was taken by switching the magnetic field to  $-5$  Oe, i.e., stage IV in Figs. 4.14a, b and 4.15, followed by a pulsed electric field, and similar behavior was observed as the previous case. This magnetization reversal process, controlled by pulsed electric fields and assisted with a weak magnetic field, is repeatable, holding promise for applications in novel multifunctional devices.

## 4.4 Electric-Field Control of Magnetoresistance

Since giant electric-field control of magnetization, magnetic anisotropy, and magnetization reversal can be achieved in the CoFeB/PMN-PT(011) heterostructure, these giant ME coupling effects can be utilized in spintronic devices to realize electric-field control of magnetoresistance, which has promising applications in terms of electrical writing and magnetic reading random access memory. Therefore, we prepared spin valves on top of (011)-oriented PMN-PT and carried on the investigation of electric-field control of magnetoresistance, via cooperation with Prof. Han's group in Institute of Physics, Chinese Academy of Sciences.

### 4.4.1 Electric-Field Control of Magnetization in CoFeB Film with Pinning Layer

The typical spin valve has a sandwich structure consisting of ferromagnetic layer/non-magnetic metal/ferromagnetic layer, in which one ferromagnetic layer is a free layer with freely rotated magnetic moments and the other is a reference layer with fixed magnetic moments (see details in Sect. 1.4.1 in Chap. 1). The direction

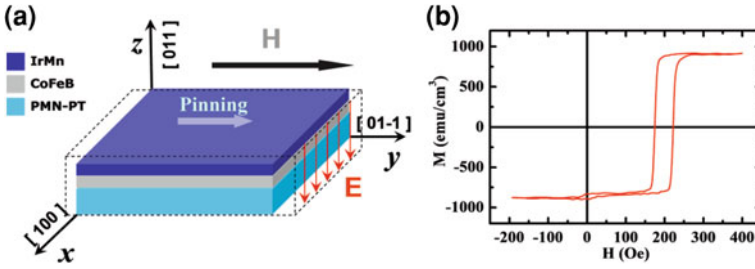


**Fig. 4.16** The **a** configuration and **b** M–H loop of the exchange bias structure

of magnetization in reference layer is pinned by an antiferromagnetic layer via exchange coupling effect between the ferromagnetic order and antiferromagnetic order at the interface. Before the investigation of electric-field control of magnetoresistance, electric-field control of magnetization and exchange bias effect in CoFeB film with pinning layer were first studied.

In the research, we employed the antiferromagnetic iridium-manganese alloy (IrMn) to be the pinning layer. Since the Neel temperature of the antiferromagnetic IrMn is above room temperature (i.e. growing temperature of CoFeB), thereby a biased magnetic field is needed to induce an uniaxial magnetic anisotropy during the growth of ferromagnetic layer CoFeB and antiferromagnetic pinning layer IrMn. The brief structure of the prepared IrMn/CoFeB/PMN-PT(011) sample is shown in Fig. 4.16a, and the property of the exchange bias effect is shown in Fig. 4.16b. From the figure, we can see that the IrMn layer generates a biased magnetic field about 200 Oe, which has a good pinning effect onto the CoFeB film and is important for the spin valve structure.

When external electric field is applied on the sample, the anisotropic strain in (011)-oriented PMN-PT will also be transferred onto the CoFeB and IrMn layers, which will result in magnetization change in the sample. Similar magnetic measurements such as M–H and M–E investigation have been carried on with in situ electric field (see details in the previous sections), and the results are shown in Fig. 4.17. From the figures, we can see that the magnetization of CoFeB can still be tuned by external electric fields, despite being pinned by the IrMn layer. The mechanism for the phenomenon is also the strain-mediated ME coupling effect, similar to the analysis in the previous discussion.

#### 4.4.2 Preparation of Spin Valve and Electric-Field Control of Magnetoresistance

Spin valve based on CoFeB with the structure of IrMn(10 nm)/CoFeB(5 nm)/Cu(2 nm)/CoFeB(5 nm) has been prepared on top of (011)-oriented PMN-PT substrate via the ultra-high vacuum magnetron sputtering system, and the investigation

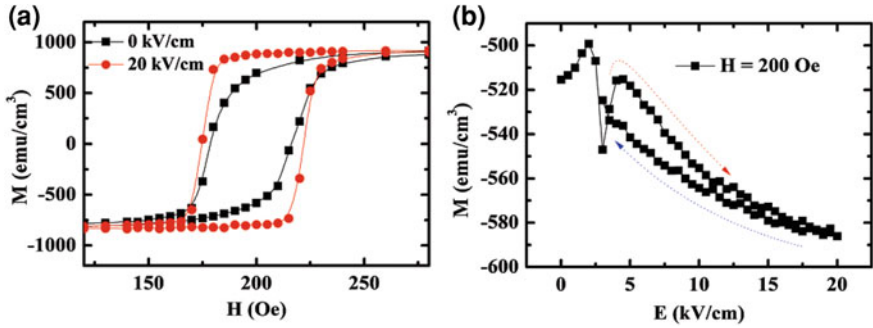
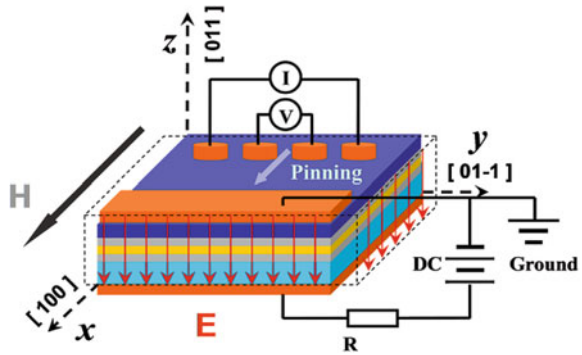


**Fig. 4.17** Electric-field control of exchange bias effect along the [01-1] direction: **a** M-H loops and **b** M-E curve

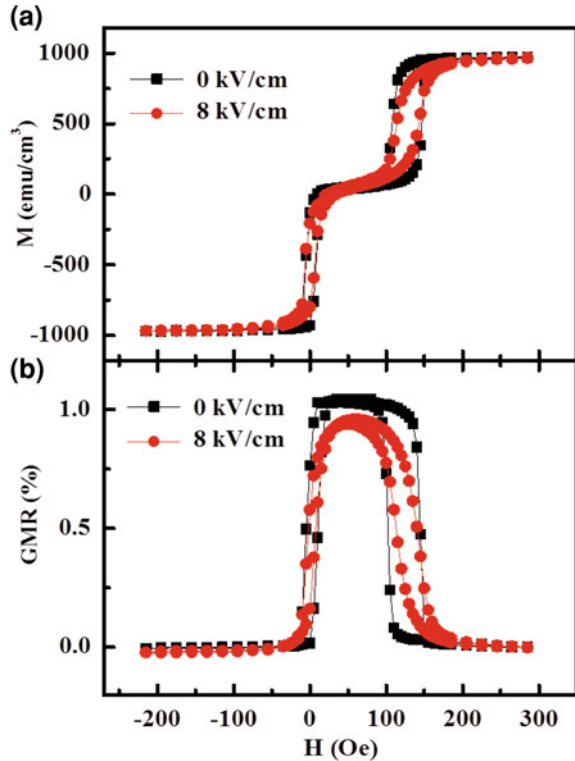
**Fig. 4.18** Configuration of electrical control of spin valve



of electric-field control of magnetization as well as magnetoresistance have been performed in the multiferroic measurement system based on MPMS. The sample structure, measurement configuration, and the way of applying electric fields as well as resistance measurement are shown in Fig. 4.18. Since the resistance of the IrMn/CoFeB/Cu/CoFeB multilayer structure is small, the four-wire circuit was employed in the electrical measurement to ensure the accuracy of resistance (see detailed method in Sect. 2.2.5 in Chap. 2) and the sample surface with spin valve structure is grounded to protect the device under high voltage.

In the spin valve structure, the magnetizations of CoFeB in both the free layer and the reference layer can be tuned by electric fields and the electric field depended M-H curves along the [100] direction are shown in Fig. 4.19a. Without electric field, the M-H curve of the structure exhibits typical “double loop” behavior due to the independent magnetization reversal in the free layer and the reference layer respectively. After applying 8 kV/cm electric field, the uniaxial magnetic anisotropy field induced by anisotropic piezostrain of (011)-oriented PMN-PT will make the magnetizing processes harder along the [100] direction in both the free layer and the reference layer and incline the “double loop” M-H curve as shown in Fig. 4.19a. Because the resistivity of Cu is smaller than that of

**Fig. 4.19** Electric-field control of **a** magnetization and **b** giant magnetoresistance in spin valve along the [100] direction



CoFeB layer, the electrical current in the spin valve will be transported inside the Cu layer and scattered by the magnetization in the CoFeB layer (i.e. current in plane, CIP mode as described detailed in Sect. 1.4.1 of Chap. 1). External magnetic field will change the direction of magnetization in the free layer and alter the relative orientation of magnetic moments in the two FM layers, resulting magnetoresistance (i.e. GMR) effect. Since the electric field will induce in-plane anisotropic strain and change the magnetization states in both sides of the CoFeB layer, which will affect the spin-dependent scattering and GMR effect as shown in Fig. 4.19b.

Although the GMR effect in the spin valve structure based on CoFeB is not large, this result has demonstrated the practicability of electric-field control of magnetoresistance in the spintronic devices via strain mediated ME coupling effect in compound multiferroic heterostructures, which is important for the energy-efficiency low-power electronics in terms of electrical writing and magnetic reading random access memory. By further improving the structure of spin valve (e.g. changing measurement configuration from the current in plane mode to current perpendicular-to plane mode) or preparing magnetic tunneling junctions on top of ferroelectric substrates with high in-plane anisotropic piezostain effect such

as (011)-oriented PMN-PT, even effective electric-field control of magnetoresistance with larger MR ratio can be achieved, which has promising applications.

## 4.5 Chapter Summary

Compound multiferroic heterostructure  $\text{Co}_{40}\text{Fe}_{40}\text{B}_{20}/\text{Pb}(\text{Mg}_{1/3}\text{Nb}_{2/3})_{0.7}\text{Ti}_{0.3}\text{O}_3$ (011) was prepared and giant electric-field control of magnetization ( $M$ ) as well as magnetic anisotropy were achieved at room temperature. Through direct investigation of magnetic response to electric field in the MPMS, a maximum relative magnetization change ( $\Delta M/M$ ) up to 450 % is observed. Further Rot-MOKE investigation demonstrated that magnetic easy axis of the sample can be rotated by  $90^\circ$  when the external electric field is larger than 5 kV/cm. The mechanism for this giant ME coupling can be understood as a combination of the ultra-high value of anisotropic in-plane piezoelectric coefficients of (011)-oriented PMN-PT and the perfect soft ferromagnetism without magnetocrystalline anisotropy of CoFeB film.

Based on the giant electric-field control of magnetization as well as magnetic anisotropy in this structure, exchange bias system and spin valve structure have been prepared on top of (011)-oriented PMN-PT. Investigations of electric-field control of magnetization in the IrMn/CoFeB exchange bias system and electric-field control of magnetoresistance in the IrMn/CoFeB/Cu/CoFeB spin valve structure have been performed and electric-field control of magnetization as well as giant magnetoresistance have been realized at room temperature. This work demonstrates the practicability of electric-field control of magnetoresistance in the spintronic devices and is helpful for the relevant investigation of electric-field control of tunneling magnetoresistance (TMR) in the MTJ based on CoFeB, which is important for the promising applications-related SME-RAMs.

## References

1. E.Y. Tsybal, H. Kohlstedt, Tunneling across a ferroelectric. *Science* **313**, 181–183 (2006)
2. M. Gajek, M. Bibes, S. Fusil et al., Tunnel junctions with multiferroic barriers. *Nat. Mater.* **6**, 296–302 (2007)
3. V. Garcia, M. Bibes, L. Bocher et al., Ferroelectric control of spin polarization. *Science* **327**, 1106–1110 (2010)
4. M. Bibes, A. Barthelemy, Multiferroics: towards a magnetoelectric memory. *Nat. Mater.* **7**, 425–426 (2008)
5. S.M. Wu, S.A. Cybart, P. Yu et al., Reversible electric control of exchange bias in a multiferroic field-effect device. *Nat. Mater.* **9**, 756–761 (2010)
6. J. Allibe, S. Fusil, K. Bouzehouane et al., Room temperature electrical manipulation of giant magnetoresistance in spin valves exchange-biased with  $\text{BiFeO}_3$ . *Nano Lett.* **12**, 1141–1145 (2012)
7. N.A. Pertsev, H. Kohlstedt, Magnetic tunnel junction on a ferroelectric substrate. *Appl. Phys. Lett.* **95**, 163503 (2009)

8. J.M. Hu, Z. Li, J. Wang et al., Electric-field control of strain-mediated magnetoelectric random access memory. *J. Appl. Phys.* **107**, 093912 (2010)
9. C. Cavaco, M. van Kampen, L. Lagae et al., A room-temperature electrical field-controlled magnetic memory cell. *J. Mater. Res.* **22**, 2111–2115 (2007)
10. M. Liu, S.D. Li, O. Obi et al., Electric field modulation of magnetoresistance in multiferroic heterostructures for ultralow power electronics. *Appl. Phys. Lett.* **98**, 222509 (2011)
11. S.E. Park, T.R. Shrout, Ultrahigh strain and piezoelectric behavior in relaxor based ferroelectric single crystals. *J. Appl. Phys.* **82**, 1804–1811 (1997)
12. J. Lou, M. Liu, D. Reed et al., Giant electric field tuning of magnetism in novel multiferroic fegab/lead zinc niobate-lead titanate (PZN-PT) heterostructures. *Adv. Mater.* **21**, 4711 (2009)
13. M. Liu, O. Obi, J. Lou et al., Giant electric field tuning of magnetic properties in multiferroic ferrite/ferroelectric heterostructures. *Adv. Funct. Mater.* **19**, 1826–1831 (2009)
14. S.U. Jen, Y.D. Yao, Y.T. Chen et al., Magnetic and electrical properties of amorphous CoFeB films. *J. Appl. Phys.* **99**, 053701 (2006)
15. S. Zhang, Y.G. Zhao, X. Xiao et al, Giant electrical modulation of magnetization in  $\text{Co}_{40}\text{Fe}_{40}\text{B}_{20}/\text{Pb}(\text{Mg}_{1/3}\text{Nb}_{2/3})_{0.7}\text{Ti}_{0.3}\text{O}_3(011)$  heterostructure. *Sci. Rep.* **4**, 3727 (2014)
16. T. Wu, A. Bur, P. Zhao et al., Giant electric-field-induced reversible and permanent magnetization reorientation on magnetoelectric  $\text{Ni}/(011)[\text{Pb}(\text{Mg}_{1/3}\text{Nb}_{2/3})\text{O}_3](1-x)-[\text{PbTiO}_3]x$  heterostructure. *Appl. Phys. Lett.* **98**, 012504 (2011)
17. J. Peng, H. Luo, D. Lin et al., Orientation dependence of transverse piezoelectric properties of  $0.70\text{Pb}(\text{Mg}_{1/3}\text{Nb}_{2/3})\text{O}_3-0.30\text{PbTiO}_3$  single crystals. *Appl. Phys. Lett.* **85**(25), 6221 (2004)
18. L. Luo, H. Wang, Y. Tang et al., Ultrahigh transverse strain and piezoelectric behavior in  $(1-x)\text{Pb}(\text{Mg}_{1/3}\text{Nb}_{2/3})\text{O}_3-x\text{PbTiO}_3$  crystals. *J. Appl. Phys.* **99**, 24104 (2006)
19. J.J. Yang, Y.G. Zhao, H.F. Tian et al., Electric field manipulation of magnetization at room temperature in multiferroic  $\text{CoFe}_2\text{O}_4/\text{Pb}(\text{Mg}_{1/3}\text{Nb}_{2/3})_{0.7}\text{Ti}_{0.3}\text{O}_3$  heterostructures. *Appl. Phys. Lett.* **94**, 212504 (2009)
20. H.X. Fu, R.E. Cohen, Polarization rotation mechanism for ultrahigh electromechanical response in single-crystal piezoelectrics. *Nature* **403**, 281–283 (2000)
21. R. Mattheis, G. Quednau, Determination of the anisotropy field strength in ultra-thin magnetic films using longitudinal MOKE and a rotating field: the ROTMOKE method. *J. Magn. Magn. Mater.* **205**, 143–150 (1999)

# Chapter 5

## Summary and Outlook

### 5.1 Research Summary

With the fast development of information storage, exploiting new concepts for dense, fast, and nonvolatile random access memory with reduced energy consumption is a significant and challenging task. To realize this goal, electric-field control of magnetism is crucial. A promising and energy-efficient way to control magnetism is using the converse magnetoelectric effect, which permits control of magnetism with electric fields rather than with electric currents or with magnetic fields. In this context, multiferroic materials which exhibit simultaneous magnetic and ferroelectric orders with coupling between them are among the top candidates for realizing electric-field control of magnetism. However, single-phase multiferroic materials are rare at room temperature and the converse magnetoelectric effects are typically also too small to be useful. The use of artificial two-phase systems consisting of ferromagnetic and ferroelectric materials, especially various room temperature ferromagnetic (FM) and ferroelectric (FE) materials, serves as an alternative approach to achieve electric-field control of magnetism and has been widely studied in recent years. In this thesis, we have investigated the electric-field control of magnetization as well as the spin-dependent transportation based on a  $\text{Co}_{40}\text{Fe}_{40}\text{B}_{20}(\text{CoFeB})/\text{Pb}(\text{Mg}_{1/3}\text{Nb}_{2/3})_{0.7}\text{Ti}_{0.3}\text{O}_3(\text{PMN-PT})$  FM/FE heterostructure. The main work can be divided into two parts as follows:

Multiferroic samples were fabricated by depositing amorphous CoFeB films on top of (001)-oriented PMN-PT substrates with an ultra-high vacuum magnetron sputtering system and the electric-field control of magnetization was performed by magnetic property measurement system with in situ electric fields. We have found that the magnetization of CoFeB film on the (001)-oriented PMN-PT exhibits a giant *loop-like* response to electric field at room temperature instead of the *butterfly-like* behavior as commonly observed in the strain-mediated FM-FE structures. Through systematic experimental investigation and theoretical analysis, it was demonstrated that the *loop-like* magnetization response to electric field originates from the combined action of  $109^\circ$  ferroelastic domain switching in PMN-PT and absence of magnetocrystalline anisotropy in CoFeB, which is a new

story for the strain-mediated FM-FE two-phase system. What is more, this large electric-field control of magnetization is tunable and nonvolatile, which is significant for applications.

In another aspect, we have found even larger electric-field control of magnetization of CoFeB on the (011)-oriented PMN-PT due to the in-plane strain anisotropy. Further experiments have demonstrated that the easy axis of CoFeB can be rotated  $90^\circ$  by external electric fields. Based on this large converse magnetoelectric effect, spin-valve structure was fabricated on top of (011)-oriented PMN-PT. It was shown that both the magnetization and giant magnetoresistance of the structure can be tuned by electric field at room temperature, which is important for applications, especially in terms of electrical writing and magnetic reading random access memories.

## 5.2 Outlook and Prospect

In recent years, the investigation of multiferroic materials and magnetoelectric (ME) coupling effect is a significant and challenging issue. The ME coupling is not only an interesting and profound phenomenon in condensed matter physics related to strong correlation system, but also has promising applications in multifunctional devices. So far, although a lot of work related to ME coupling and electrical control of magnetization has been done and achieved fruitful results, there are still a number of problems and challenges in this issue.

One of them is the challenge of searching new single-phase multiferroic materials with large ME coupling effect and coexistence of ferroelectric and ferromagnetic orders at room temperature. Except BiFeO<sub>3</sub>, nearly all the ME coupling effects in the single-phase multiferroic materials are presented at low temperature, although researchers have found room temperature single-phase multiferroics according to reports in the last several years, in which the polarization is induced by magnetic ordering. However, the value of “ferroelectric” polarization in this system is very small, which is disadvantageous for applications. Single-phase multiferroic materials with large magnetization, polarization, and ME coupling effect at room temperature are still waiting for man’s exploration.

On the other hand, realizing dense, fast, energy-efficient random access memories in terms of electrical writing and magnetic reading is the main aim in the investigation of multiferroic materials and ME coupling. Although a lot of work related to electric-field control of magnetization has been reported, the work related to electric-field control of magnetoresistance in spintronic devices is rare. Even in the current results on electric-field control of magnetoresistance, either electrical control of tunneling magnetoresistance (TMR) at low temperature or electrical control of giant magnetoresistance (GMR) at room temperature has been reported. The most important and useful work, i.e., electrical control of TMR at room temperature, is still ongoing and requires more research.